STUDIES OF MAGNETIC SOLIDS AT LOW TEMPERATURES.

A Thesis

Submitted for the degree of

Doctor of Philosophy

at the

University of Oxford

by

John D. Cashion.



New College,

Trinity Term 1969.

ABSTRACT

The series of compounds which crystallize in the orthorhombic Pbnm distortion of the perovskite structure has proved a lucrative source of experiments in solid state physics. In the general formula ABO_3, either or both the metallic ions may be magnetic and since the two site symmetries are also different this provides several different degrees of complication.

The main study in this thesis is of the two members $GdAlO_3$ and $DyAlO_3$ in which the B site is occupied by the diamagnetic aluminium ion. We therefore only have to consider the interactions of the rare earth ions with each other and with their surroundings.

Three types of experimental measurements have been carried out. Specific heat measurements in the range $0.5^{o}K$ to $20^{o}K$ were performed in a conventionally designed He^3 cryostat using a germanium resistance thermometer. Measurements of the magnetic moment and most of the magnetic susceptibility measurements were carried out by a ballistic method and the induced signal measured on an integrating digital voltmeter. Applied magnetic fields up to 90kOe were available for use in the moment experiments.

The temperature range 0.4°K to 4.2°K could be covered using pumped He^3 or He^4. Susceptibility measurements in the pumped liquid hydrogen range and some measurements in the liquid He^4 range were carried out using a mutual inductance technique.

The most prominent feature of the specific heat measurement on $GdAlO_3$ was a lambda anomaly peaked at 3.870°K which we take to be the ordering temperature. Around 1°K there is another smaller bump which is a Shottky anomaly due to the crystal field splitting. The total entropy under the magnetic part of the specific heat was measured to be R ln8 showing that the Gd^{3+} ion is in its $^8S_{7/2}$ ground state.

Measurement of the magnetic susceptibility of $GdAlO_3$ along the three orthorhombic axes showed results similar to that expected for a simple two sublattice antiferromagnet with the b-axis as the direction of magnetic alignment. Above the Néel temperature there was very little anisotropy.

As expected for an antiferromagnet with small anisotropy, the phenomenon of "spin flop" was observed in the magnetic moment measurement along the b-axis. The critical field was found to be 11.58kOe. Magnetic saturation was achieved along the a, b and c-axes at 45.6kOe,

39.5kOe and 44.4kOe respectively with an isotropic saturation moment within 1% of 7 Bohr magnetons per atom. From a simple molecular field theory analysis of these experiments we obtain the values 21.0kOe for the exchange field and 2.7kOe for the anisotropy field.

Closer analysis reveals that the anisotropy is mainly due to the crystal field interaction and the principal axis is canted at $\pm 38^{\circ}$ to the b-axis in the a-b plane for the two different magnetic sites. This means that the ordering mode is really divided into four sublattices with hidden canting in an $A_x G_y$ configuration following the notation of Bertaut*. At low temperatures the G_y component, which corresponds to antiparallel nearest neighbours, is dominant showing why many of the properties could be explained on the basis of a simple two sublattice antiferromagnet.

The sublattice magnetization was calculated in several different ways and helped show that the internal consistency of molecular field theory is much better than its accuracy in ab initio calculations.

Using results from the moment experiments along the b-axis the magnetic phase diagram on the H-T plane was plotted.

* E.F.Bertaut, Magnetism Vol.III, ed.Rado & Suhl, (Academic Press, 1963) p150.

The value of the nearest neighbour exchange constant was evaluated from results of several different experiments using the Heisenberg model and a best value of $J/k = -0.067^{\circ}K$ obtained. From the consistency of the results it was concluded that second nearest neighbour exchange is negligible.

Specific heat measurements on $DyAlO_3$ below $8^{\circ}K$ showed only a lambda anomaly peaked at the Neel point of $3.53^{\circ}K$. The entropy under the specific heat was measured to be almost R ln2 showing that the Dy^{3+} ion is in the lowest lying Kramers' doublet of the $^6H_{15/2}$ ground state.

Thus the Dy^{3+} is well described by an effective spin of $\frac{1}{2}$ and this gives rise to very anisotropic interactions with its surroundings. Optical measurements* have shown that one g-value is very much larger than the other two so we expect it to behave to a good approximation as an Ising system.

The susceptibility measurements below the Néel temperature confirm this belief, with the susceptibility decreasing with decreasing temperature along both the a- and b-axes. The ratio of the two measurements remains constant at a value corresponding to $\tan^2 33^{\circ}$ showing that

* H.Schuchert, S.Hufner & R.Faulhaber, Z.Physik, to be published.

the canting angle is $\pm 33^{\circ}$ to the b-axis. The susceptibility along the c-axis is very small and almost temperature independent.

The moment measurements in the a-b plane all showed the phenomenon of "spin flip" or reversal of the direction of a sublattice, expected in an anisotropic antiferromagnet. Measurements at an arbitrary angle showed two flips due to the magnetically inequivalent sublattices and the angular dependence could be explained well using dipole interactions alone.

Although the magnetic ordering is due mainly to dipole interactions it is shown that there is a significant antiferromagnetic exchange interaction with $J/k \sim -1^{\circ}K$ between nearest neighbours along the c-axis.

Susceptibility measurements were carried out on four series of rare earth compounds of the general formulae $RNbO_4$, R_3NbO_7, R_2TiO_5 and $R_2Ti_2O_7$ as well as several other members of the $RAlO_3$ family. Half of the compounds showed ordering transitions but further detailed work could not be carried out because of the difficulty in obtaining suitable specimens.

ACKNOWLEDGEMENTS.

The work described in this thesis has been entirely carried out in the Clarendon Laboratory and I am grateful to Professor B.Bleaney, F.R.S. for extending to me this privilege.

For his cheerful and never failing encouragement and help during all aspects of this work it is a pleasure to thank my supervisor Dr.A.H.Cooke.

All the experiments described were carried out with the assistance of Mr.M.R.Wells, and for his technical guidance and the many discussions, both lighthearted and scientific, I am extremely grateful.

For many useful discussions I would like to thank Dr.M.J.M.Leask, Dr.T.L.Thorp, Dr.J.F.B.Hawkes, Dr.G.A.Gehring, Dr.K.A.Gehring, Dr.D.T.Edmonds and Mr.G.P.Gill and to Mr.C.J.Ellis also for providing me with his unpublished results.

All the specimens used were prepared by Mrs.B.M.Wanklyn and to her I am very grateful.

For permission to use the facilities of the Computing Laboratory I would like to thank Professor L.Fox and Dr.J.S.Rollett.

I would especially like to thank my wife Joan for all the assistance she has given particularly in computing and in the preparation of this thesis.

Thanks are also due to many other people for their assistance, particularly Mr.J.Shaw, Mr.H.S.Locke, Mr.S.Giles, Mr.D.T.Smith, Mr.P.A.Hudson, Mr.C.W.Band, Mr.E.J.Jenkinson, Mr.T.Carr and the staff of the maintenance workshop and Mr.A.Hazel and the liquefaction staff.

Finally the financial support of a Sir Arthur Sims Travelling Scholarship is gratefully acknowledged.

CONTENTS.

ABSTRACT (i)

ACKNOWLEDGEMENTS (vi)

CHAPTER 1 PROEM

1-1	Introduction	1
1-2	Apparatus	5
1-3	Structure of the Compounds $RAlO_3$	15
1-4	Growth and Orientation of $RAlO_3$ Specimens	21
1-5	Magnetic Ordering Arrangements in $RAlO_3$ Crystals	26

CHAPTER 2 GADOLINIUM ALUMINATE - EXPERIMENTAL RESULTS

2-1	Introduction	32
2-2	Other Magnetic Measurements	34
2-3	Specific Heat Measurements	38
2-4	Susceptibility Measurements	53
2-5	Magnetic Moment Measurements	58
2-6	Summary	70

CHAPTER 3 GADOLINIUM ALUMINATE
SUBLATTICE MAGNETIZATION and the PHASE DIAGRAM

3-1	Introduction	72
3-2	Fisher's Relation	75
3-3	The Magnetic Phase Diagram	77
3-4	Sublattice Magnetization from the Susceptibility	82
3-5	Sublattice Magnetization from the Specific Heat	87

CHAPTER 3 (continued)

3-6	Sublattice Magnetization by Molecular Field Theory	87
3-7	Sublattice Magnetization from the Anisotropy Energy	91
3-8	Sublattice Magnetization from the Spin Flop Area	95
3-9	Summary	99

CHAPTER 4 GADOLINIUM ALUMINATE
The EXCHANGE and CRYSTAL FIELD INTERACTIONS

4-1	Introduction	102
4-2	Consideration of Possible Interactions	103
4-3	Crystal Field Parameters from Moment Measurements	111
4-4	CEF Parameters from Susceptibility Measurements	115
4-5	Estimates of the Exchange Parameter	118
4-6	Miscellaneous Explanations	125
4-7	The Canting Angle	130
4-8	Summary	132

CHAPTER 5 DYSPROSIUM ALUMINATE - EXPERIMENTAL RESULTS

5-1	Introduction	135
5-2	Other Magnetic Measurements	136
5-3	Specific Heat Measurements	139
5-4	Susceptibility Measurements	146
5-5	Moment Measurements	152
5-6	Summary	160

CHAPTER 6 DYSPROSIUM ALUMINATE - ANALYSIS of RESULTS

6-1	Introduction	162
6-2	Consideration of Interactions	162
6-3	Analysis of Moment Experiments	168
6-4	The Exchange Interactions	179
6-5	Summary	186

CHAPTER 7 OTHER MAGNETIC MEASUREMENTS

7-1	Introduction	187
7-2	Interpretation of Susceptibility Measurements	188
7-3	Rare Earth Orthoaluminates $RAlO_3$	191
7-4	Rare Earth Orthoniobates $RNbO_4$	196
7-5	Rare Earth Niobates R_3NbO_7	199
7-6	Rare Earth Titanates R_2TiO_5	202
7-7	Rare Earth Titanates $R_2Ti_2O_7$	203
7-8	Conclusions and Summary	205

APPENDIX 1 ORDERING MODES in the Pbnm STRUCTURE 207

GLOSSARY of SYMBOLS 214

REFERENCES 217

CHAPTER ONE

PROEM

1-1. Introduction.

The paths taken by experimental and theoretical physicists in their attempts to understand the same field of interest are usually diverse and quite often pursued without any thought of making their results easier to understand or more useful for the other.

The topic of magnetism is no exception to this unfortunate state of affairs and one may wonder at times whether there is not scope for more interaction and feedback between the two.

To some extent these feelings may be the expressions of dismay from an experimentalist who sees the mathematical techniques of the theoreticians becoming more and more sophisticated beyond his knowledge, but the complaint is not limited to this direction.

In this thesis we have tried as much as possible to compare our experimental results with different theories, and in so doing to not only explain our results but also to some extent evaluate the accuracy or

consistency of the theories.

We are fortunate that for the structure with which we are mainly concerned, the distorted perovskite form of the rare earth aluminates, the magnetic ions are sufficiently close to a simple cubic sublattice to enable us to make meaningful comparison with theoretical formulae derived for this structure. However many experimentalists are not so fortunate, and the number of theoretical results for the structures simple cubic, face centred cubic, body centred cubic and diamond follow a rapidly decreasing sequence, diminishing almost to zero for non-cubic lattices.

In some ways one cannot blame the theoretician for not evaluating his calculations for an enormous number of crystal structures. However very frequently a few sentences of helpful advice on sensible extrapolations to other structures or higher values of spin from the person who (hopefully) understands the theory would be of immeasurable help to the experimentalist who lacks a thorough knowledge of techniques like many-time Green's functions or diagram summations.

In the course of writing this thesis several topics became evident where theoretical knowledge could

be appreciably extended without undue labour. This is not including topics such as critical point phenomena, where the amount of calculation required to produce each better theory increases almost as fast as some of the power law divergences it predicts.

One opening for extension is in calculation of the energy and entropy distribution above and below the Néel point as measured in a specific heat experiment. This has been worked out by Domb and his coworkers[1] for zero anisotropy, but inclusion of anisotropy affects both the total energy and the distribution. While it is possible to work out very simply the total energy, calculation of the distribution requires a summation of the appropriate diagrams - possibly a type which has not been summed before.

However a table of such values for different lattices and values of S taking the simplest types of anisotropy - single ion DS_z^2 and long range dipole-dipole interactions - would be of considerable help to the experimentalist in his estimation of the size of interactions from specific heat data.

It was in 1907 that Pierre Weiss[2] first suggested that spontaneous magnetism was caused by

interactions between atoms, but the only interaction then known - the dipole-dipole interaction - was much too small to account for the observed transition temperatures of hundreds of degrees.

It was not until the advent of quantum theory that Heisenberg[3] and Dirac[4] discovered the exchange effect - an interaction with no classical anologue - and two years later Heisenberg[5] and Frenkel[6] independently demonstrated that this exchange effect could account for Weiss' molecular field.

Since then the Hamiltonian

$$\mathcal{H} = -2 \sum_{i<j} J_{ij} \underline{S}_i \cdot \underline{S}_j$$

has become universally known as the Heisenberg Hamiltonian.

After a brief description of some technical background in the remainder of this Chapter, Chapters 2-4 deal with the experimental results and interpretations on gadolinium aluminate, $GdAlO_3$ - a substance whose exchange coupling is found to be described extremely well by the isotropic Heisenberg Hamiltonian.

The properties of extremely anisotropic substances obviously will not be well described by the Heisenberg Hamiltonian and there is a simpler Hamiltonian

due to Ising[7] which includes only the z-components of the interacting spins:

$$\mathcal{H} = -2 \sum_{i<j} J_{ij} S_{zi} S_{zj}$$

It is said that Ising gave up his Hamiltonian in disgust because it failed to predict a phase transition for the linear chain with nearest neighbour interactions.

However since then it has had a revival because of its greater mathematical tractibility, which culminated in Onsager's exact solution[8] of the two dimensional model. The anisotropic g-values of dysprosium aluminate, $DyAlO_3$, described in Chapters 5 and 6 make it a good substance to be understood using the Ising Hamiltonian.

Finally in Chapter 7 a brief description is given of the experimental results of susceptibility measurements on several series of rare earth compounds which proved to be magnetically interesting but on which further work was stopped because of the difficulty of obtaining good stoichiometric single crystals.

1-2. Apparatus.

Three different pieces of apparatus have been used for the measurements in this thesis. Since all have been thoroughly described elsewhere, only a brief

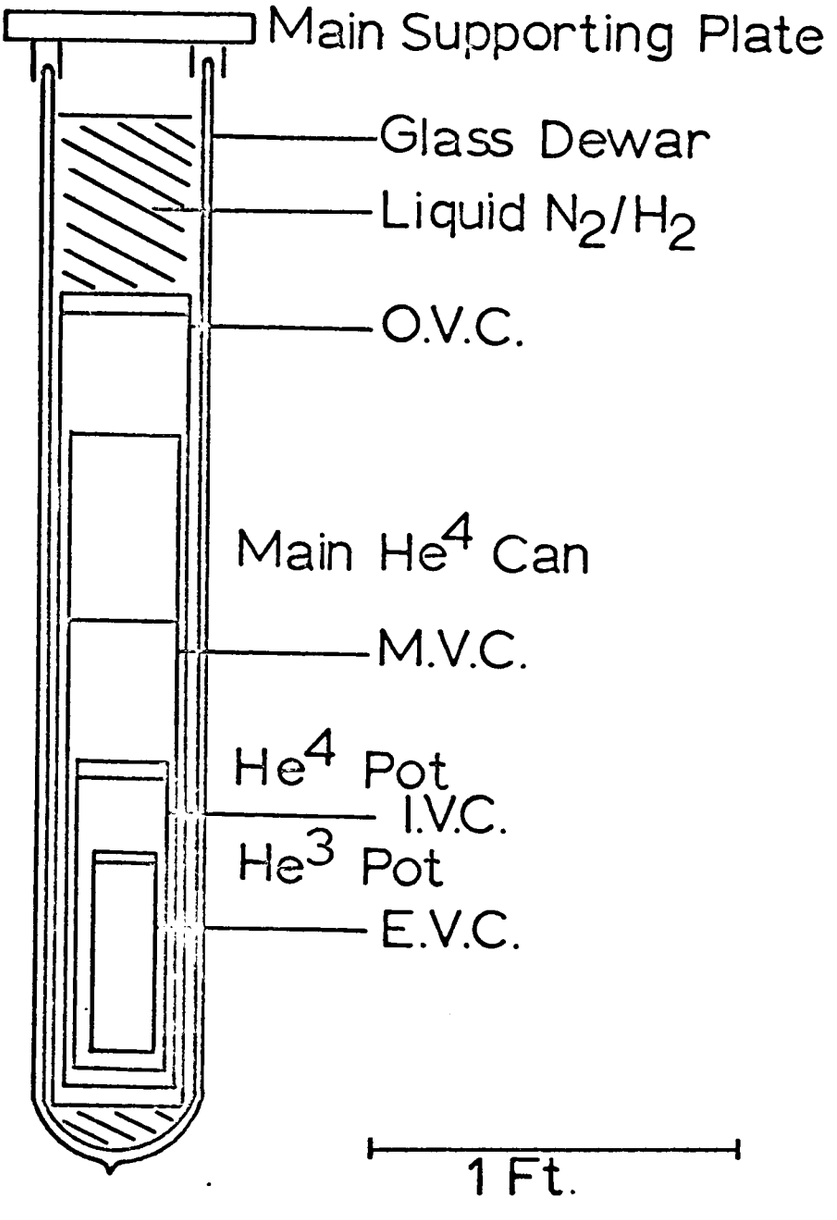
description will be given here to aid in the evaluation of the experiments.

The specific heat apparatus[9] was designed to measure specimens with a heat capacity as low as 10^{-3} J/°K in the range 0.4° - 20°K using liquid He^3, He^4, and hydrogen. The apparatus is shown schematically in Fig.1-1. The main He^4 can holds 600cc and, in the mode for low temperature running, remains at 4.2°K with a boil-off of 30cc/hr. A needle valve allows the pumped He^4 pot to be filled to its capacity of 20cc, and its boil-off is about 1½cc/hr at 1°K.

Sufficient He^3 to almost fill the He^3 pot (2cc liquid) can be condensed in and this is sufficient for 6-8 hours pumping. The calorimeter may be brought into thermal contact with this pot by a mechanical heat switch (Fig.1-2) whose stainless steel jaws clamp onto a gold plated copper wire.

The calorimeter is a thin walled copper cylinder containing the specimen and 8-10mm He^3 gas at room temperature. A heater made of a mat of constantan wire with resistance 1600Ω is wound around the calorimeter. The heater current is measured by a potentiometer and

Figure 1-1



He^3 Specific Heat Cryostat

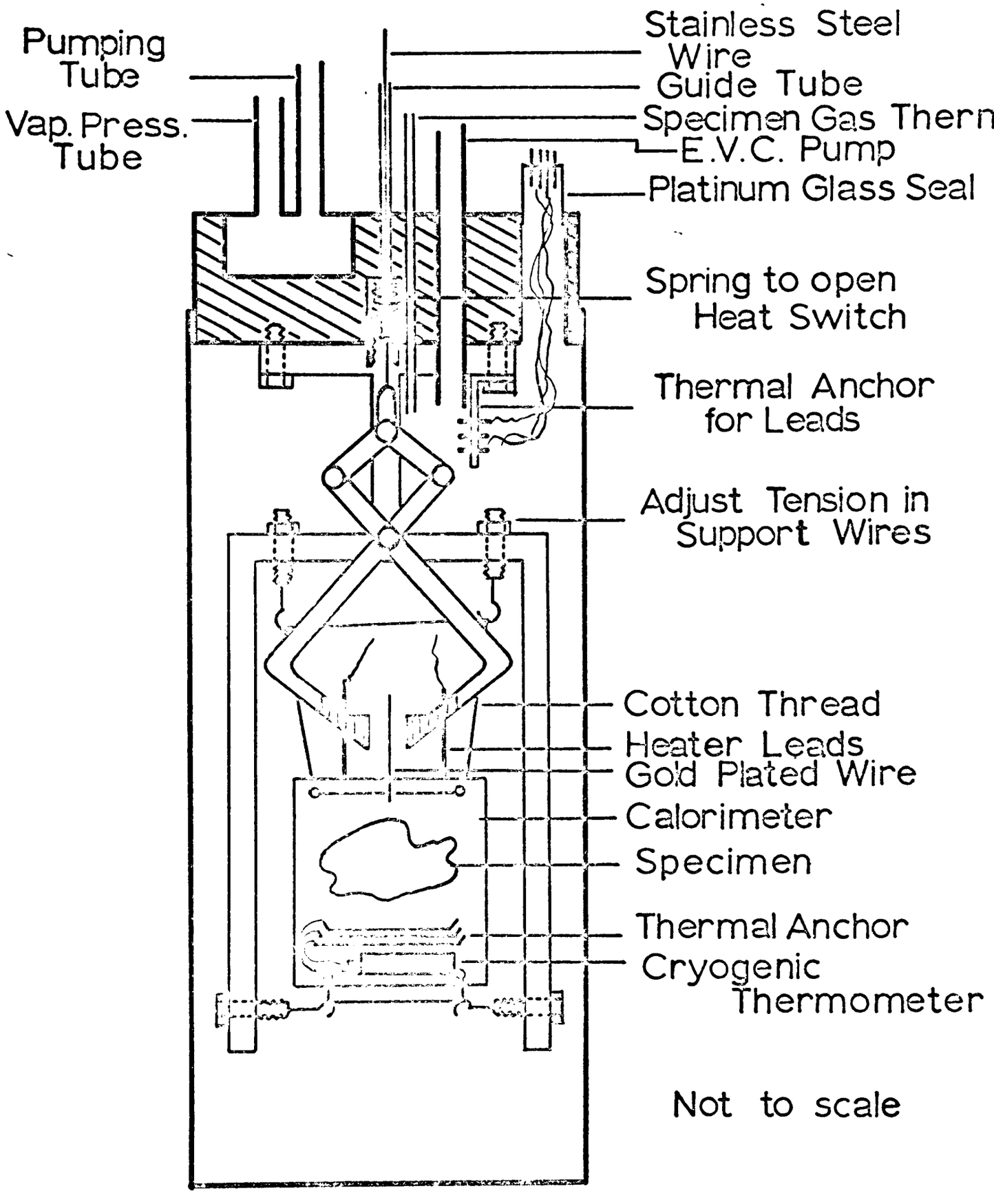


Figure 1-2

He^3 Specific Heat Cryostat

standard resistance and the heating times controlled by an electronic timer.

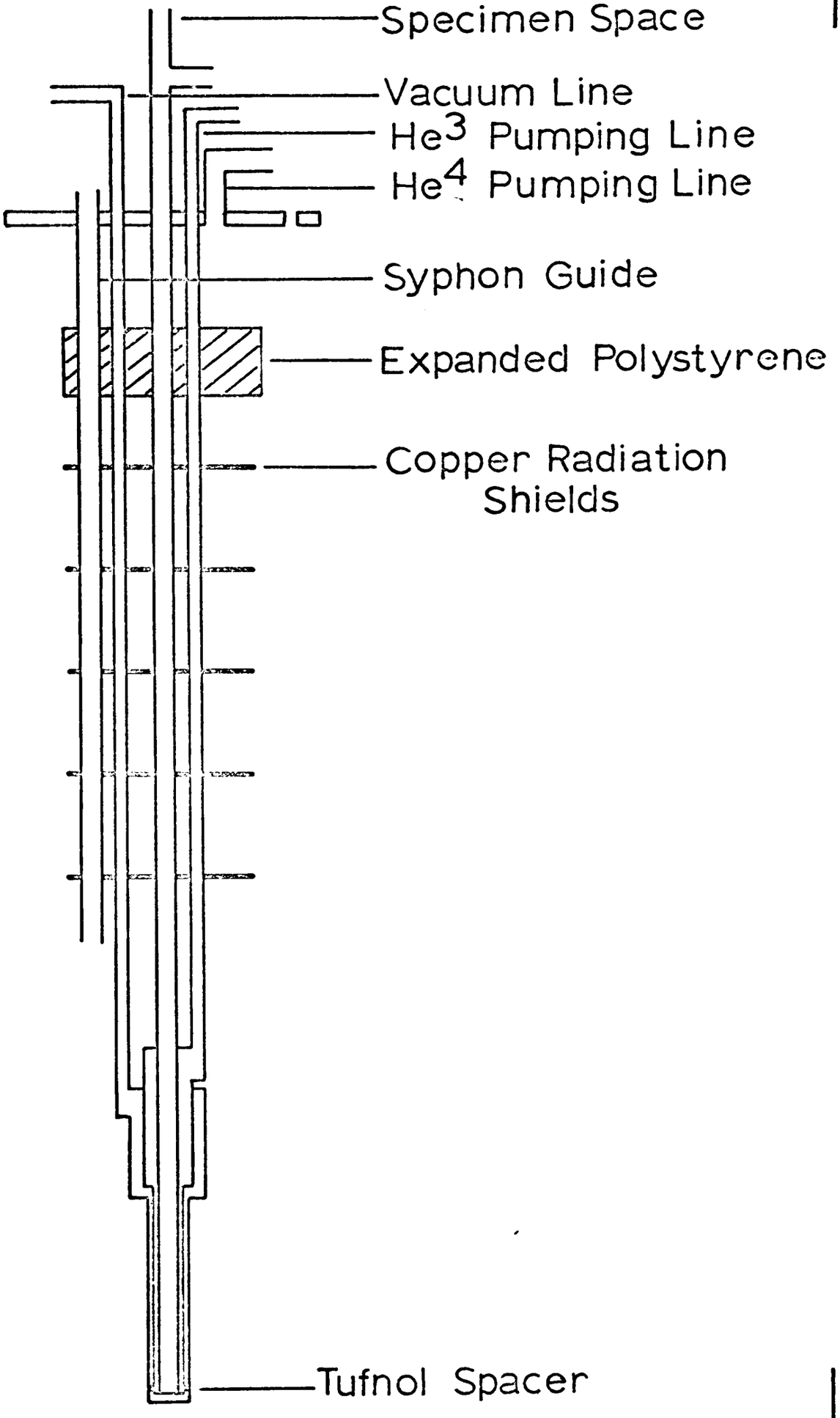
Two germanium resistance thermometers in a three lead configuration were used for temperature measurement in conjunction with an a.c. Wheatstone bridge operating at 400c/s. The high temperature thermometer covers the range 1.3°K (5000Ω) to 20°K (60Ω) and the low temperature thermometer from 0.4°K (1400Ω) to 1.3°K (230Ω) using a thermometer current of 2μA.

Measurements are taken isothermally i.e. at constant temperature of the surrounding heat shield and temperature drifts plotted as a function of time to obtain the true heating interval.

A ballistic method of measurement was used both for high field magnetic moment and most susceptibility measurements. A metal dewar(9 with a 2" tail, which could be inserted into either a 90kOe water cooled solenoid or a 1kOe air cooled solenoid for the two different measurements, formed the body of the apparatus.

The internal details are shown in Fig.1-3. The entire He^4 can of 2.3 litre capacity is pumped and this is separated at the lower end from the inner tubes by a vacuum casing. The specimen tube contains 2-3mm of

Figure 1-3



He^3 Magnetic Moment Cryostat

exchange gas and the space around it contains condensed gas, either He^3 or He^4 being used in both depending on the temperature range to be covered.

The specimen is contained in a P.T.F.E. box suspended from a german-silver tube. The container material was chosen because of its ability to withstand boiling in aqua regia - the method used for cleaning containers between experiments. The specimen is moved pneumatically through a fixed 3cm travel which carries it between the centres of the two oppositely wound pick-up coils.

The only modification of the system from that described by Thorp is that the induced signal is now recorded on a Hewlett-Packard 2401C integrating digital voltmeter via a 3sec RC time constant and a Hewlett-Packard 2411A x10 amplifier.

The system is calibrated against the saturation moment of manganous ammonium sulphate. The sensitivity is sufficient that 100mgm of manganous ammonium sulphate gives a signal of 5mV-sec at saturation with a noise level of 1 - 20μV-sec depending on magnet power.

The absolute accuracy between experiments is $\pm 1\%$ although in regions of low signal, e.g. below the

spin flop in $GdAlO_3$, the correction for the magnetic effect of the specimen assembly may be 10% of the total signal.

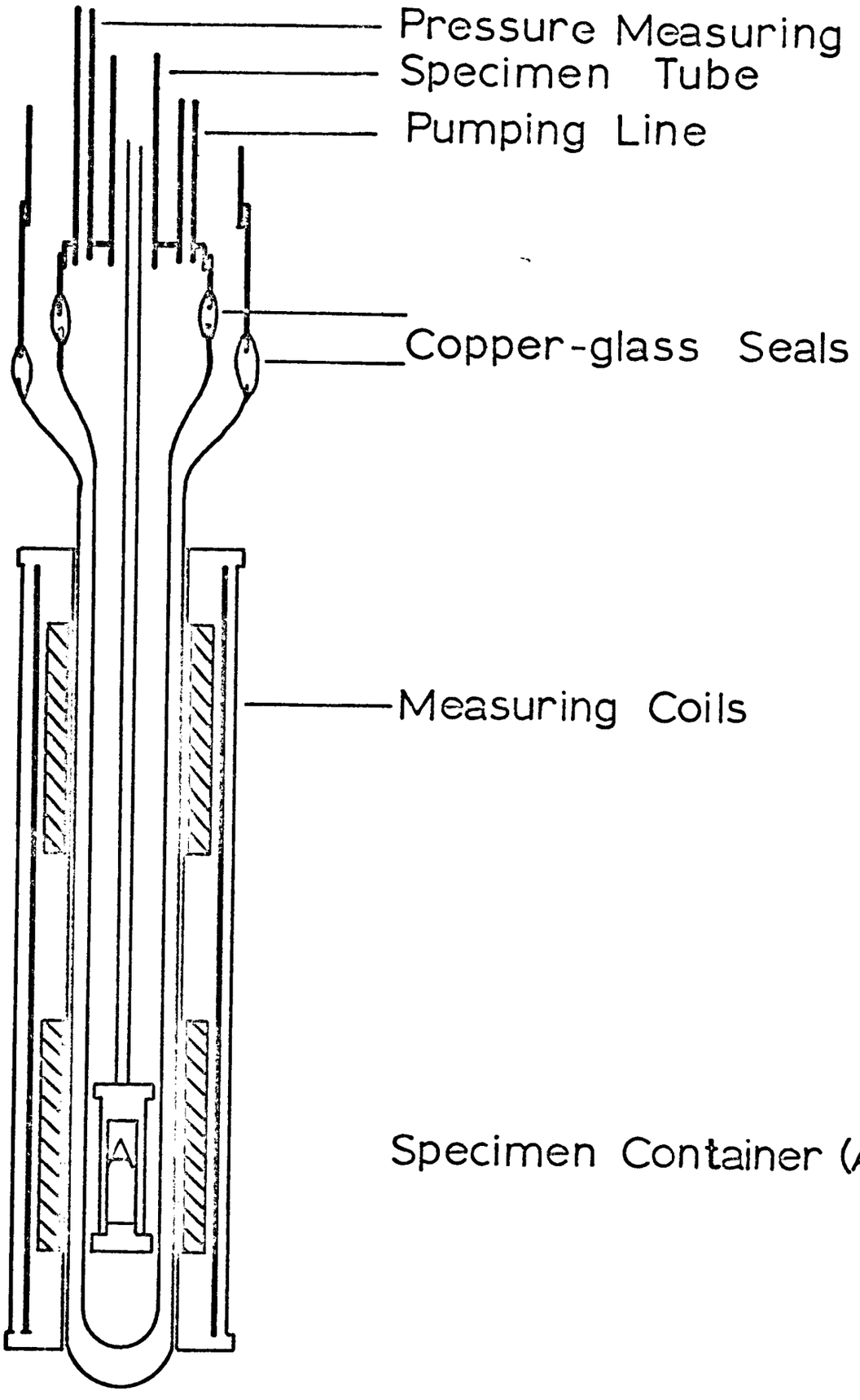
The third piece of apparatus measures susceptibilities by an a.c. mutual inductance technique and has been described by McKim and Wolf[10]. It was used for all hydrogen range measurements and also for the measurements of Chapter 7. The system cannot be used with He^3.

The lower part of the apparatus is shown in Fig.1-4 with the two oppositely wound secondary coils surrounded by a primary coil, both being immersed in liquid hydrogen. The specimen is again in a P.T.F.E. container and can be moved between the centres of the two secondary coils.

The measuring system is a Hartshorn bridge shown schematically in Fig.1-5. The normal operating frequency is 175c/s with the bridge being balanced at both positions of the specimen to give both the real and immaginary parts of the susceptibility.

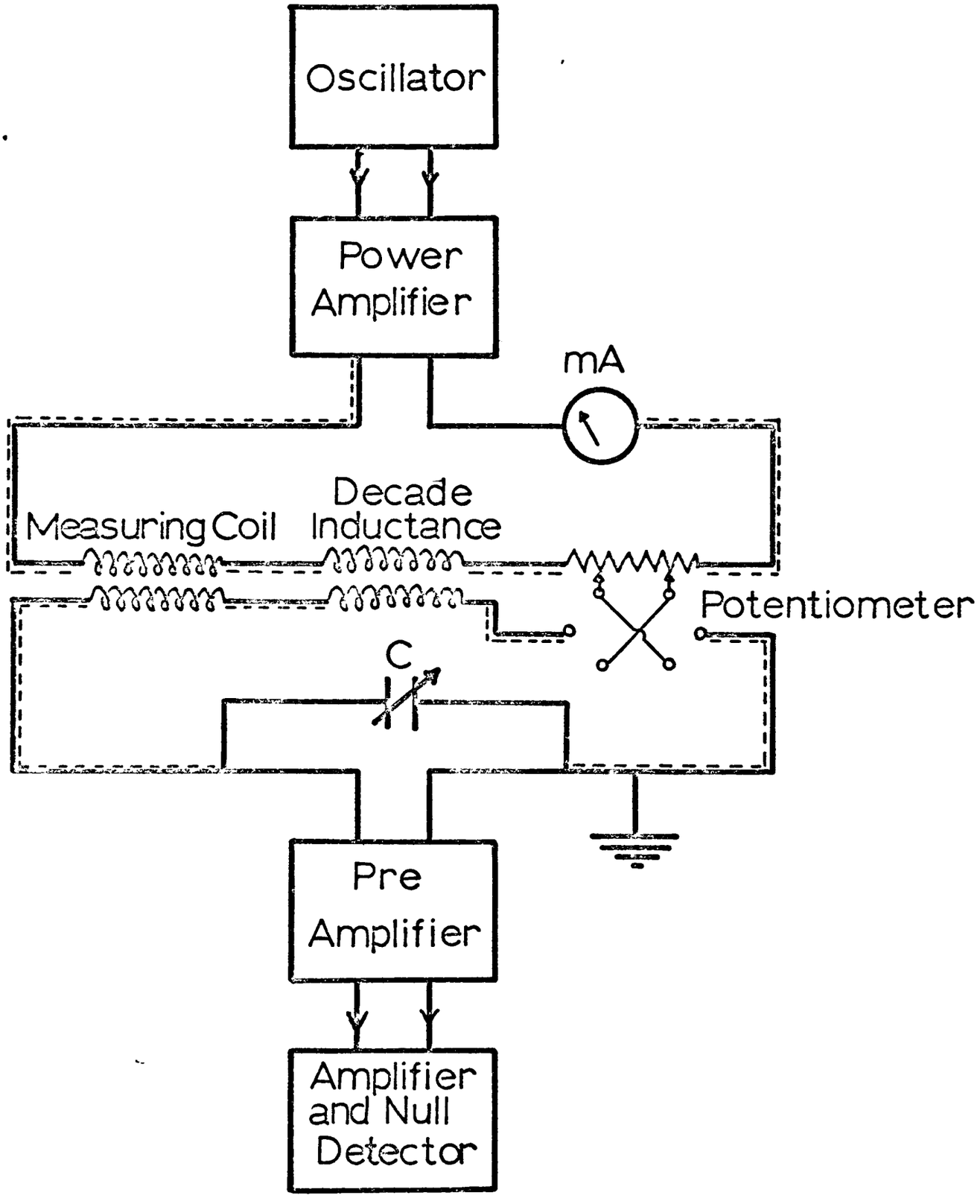
Calibration was again carried out against manganous ammonium sulphate. The reproducibility of results on this apparatus was not quite as good as by

Figure 1-4



Daintree Cryostat (Modified)

Figure 1-5



A.C. Susceptibility Measuring System

the d.c. method although systematic accuracies are comparable. Its main advantage is in simplicity and speed of obtaining results.

1-3. Structure of the Compounds $RAlO_3$.

The first members of the group of compounds $RAlO_3$ (R = rare earth ion) were grown at the Bell Telephone Laboratories by J.P.Remeika, and their structure determined by S.Geller and his co-workers[11] during an extensive study of compounds with the distorted perovskite structure (space group D_{2h}^{16} - Pbnm). The ideal perovskite structure for compounds of the general formula ABX_3 is cubic and can be easily visualized as shown in Fig.1-6 which shows the environment for both an A atom and a B atom.

However of the very many compounds with this formula, nearly all, including perovskite ($CaTiO_3$) itself, are slightly distorted, although retaining basically the ideal configuration. The new unit cell may be tetragonal, orthorhombic, rhombohedral, hexagonal or triclinic depending on the particular distortion and may contain more than one of the original perovskite unit cells.

In the case where A is yttrium or a rare earth

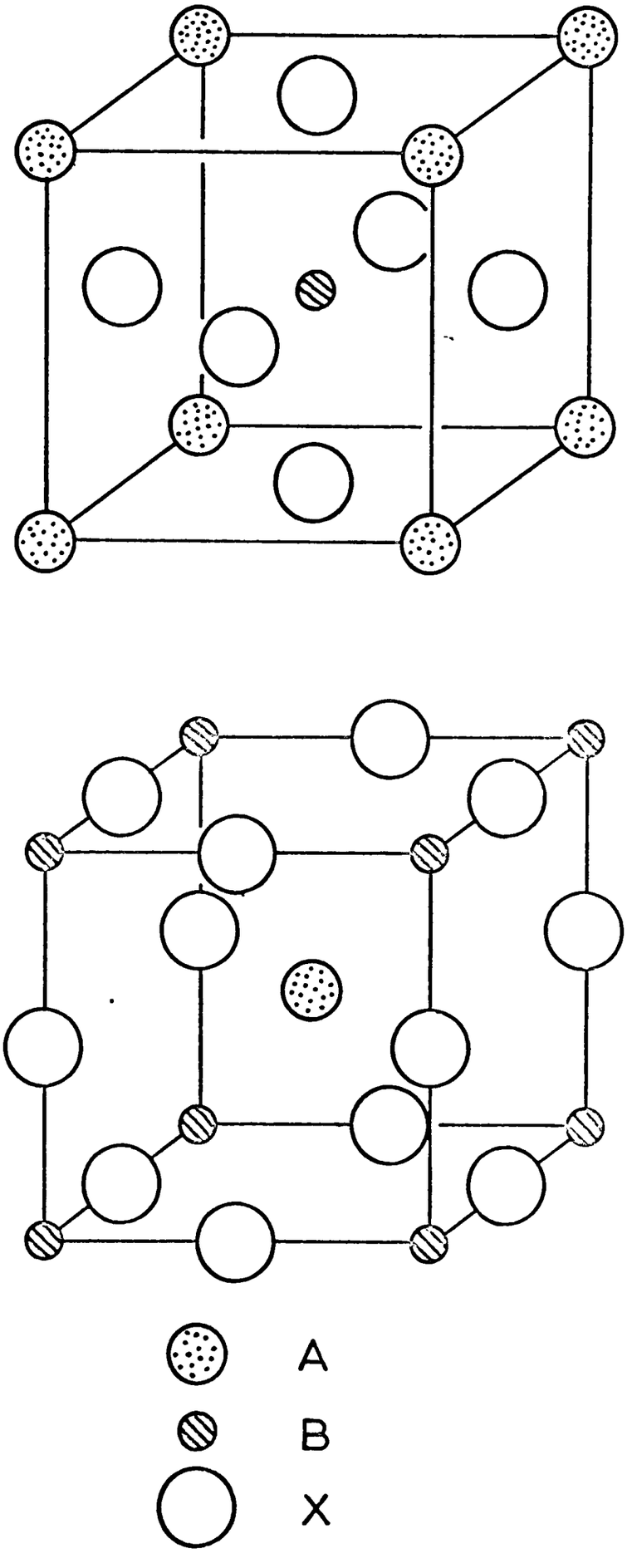


Fig. 1-6 Perovskite ABX_3

ion, B = Al, Fe, Mn, Co, Cr, Sc, Ga or V and X is oxygen, the new structure is orthorhombic Pbnm in all except a few cases. This structure contains four of the old perovskite pseudo-cells, now monoclinic, and the relation between the two is shown in Fig.1-7. It can be seen that the c-axis is common to the two cells but the other two pseudo-cell axes are diagonals between the orthorhombic a- and b-axes. The angle β of the monoclinic cell is at most a few degrees from a right angle and of course depends on the relative ionic sizes. It is 90.6° for $GdAlO_3$ and 90.9° for $DyAlO_3$, the two crystals we are mainly interested in.

The three $RAlO_3$ members which do not have the Pbnm structure are those with R = La, Pr and Nd, which have a less distorted rhombohedral unit cell (space group D_{3d}^5 - $R\bar{3}m$) containing two perovskite units. $LaAlO_3$ has a crystallographic transition back to the cubic phase for temperatures above $435^{\circ}C$ while $SmAlO_3$, which has an angle β of only 90.1°, has a transition from Pbnm to $R\bar{3}m$ at $900^{\circ}C$.

The site positions for the ions in the rare-earth aluminates with the Pbnm structure were given by Geller to be:

• Al

O Gd

Oxygen atoms not shown

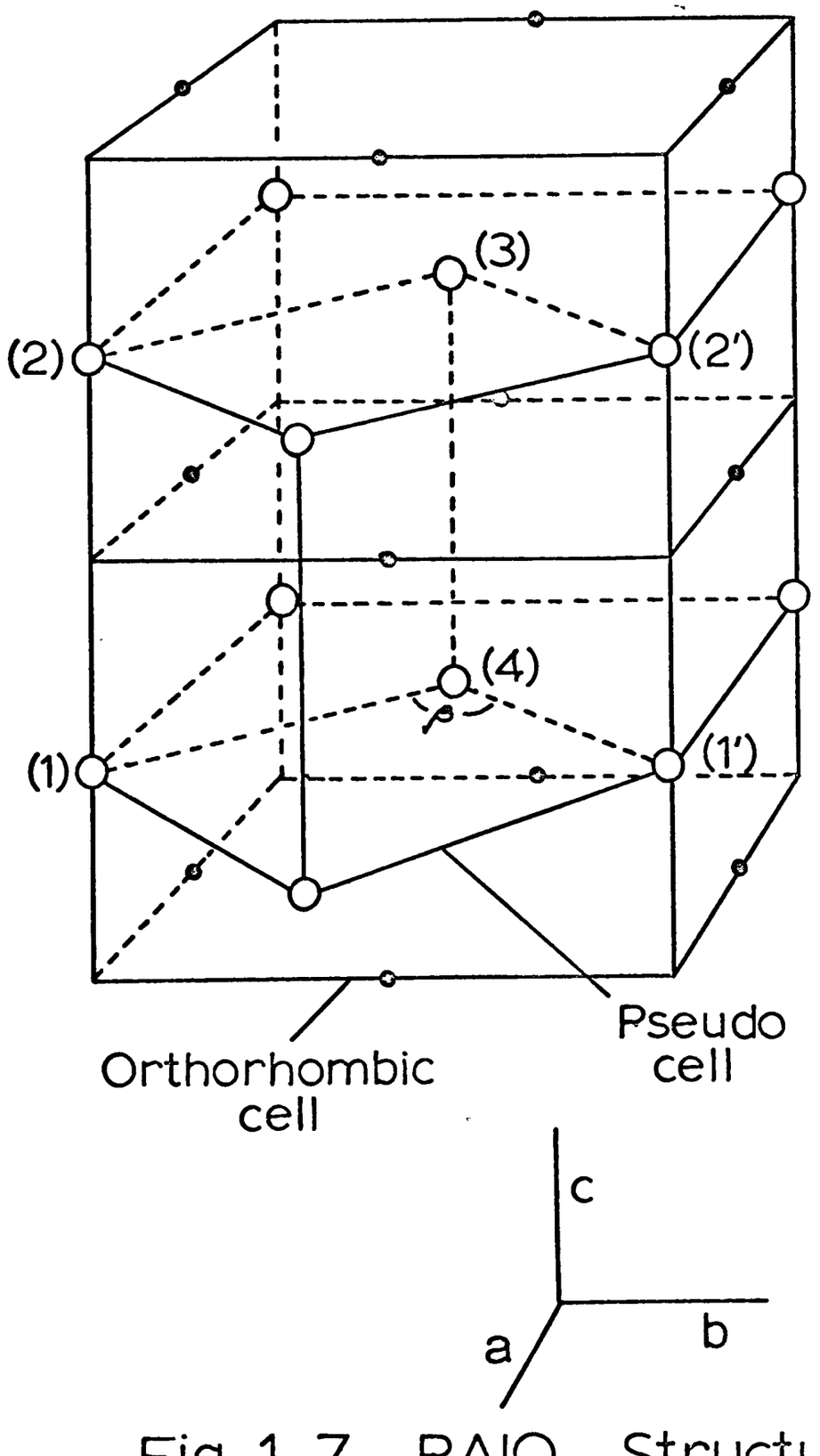


Fig 1-7 $RAlO_3$ Structure

R	4c sites	$x,y,1/4$;	$\bar{x},\bar{y},3/4$;
		$\frac{1}{2}+x,\frac{1}{2}-y,3/4$;	$\frac{1}{2}-x,\frac{1}{2}+y,1/4$.
Al	4b sites	$\frac{1}{2},0,0$; $\frac{1}{2},0,\frac{1}{2}$;	$0,\frac{1}{2},0$; $0,\frac{1}{2},\frac{1}{2}$.
O_I	8d sites	x',y',z';	$\bar{x}',\bar{y}',\bar{z}'$;
		$\frac{1}{2}-x',\frac{1}{2}+y',\frac{1}{2}-z'$;	$\frac{1}{2}+x',\frac{1}{2}-y',\frac{1}{2}+z'$;
		$\bar{x}',\bar{y}',\frac{1}{2}+z'$;	$x',y',\frac{1}{2}-z'$;
		$\frac{1}{2}+x',\frac{1}{2}-y',\bar{z}'$;	$\frac{1}{2}-x',\frac{1}{2}+y',z'$.
O_{II}	4c sites	with different value of x and y.	

Thus the aluminiums are on undistorted special positions in the new cell and are centres of inversion symmetry. However the rare earth ions are displaced in the a-b plane from the special positions they occupied in the cubic structure, but do lie on a mirror plane perpendicular to the c-axis. The positions of the atoms and their relation to the various planes and axes of symmetry can be seen from Fig.1-8.

For the oxygen sites, the distortions may be rewritten as:

8d sites $x' = 1/4 + \alpha$; $y' = 1/4 + \beta$; $z' = 0.05$

4c sites $x = \frac{1}{2} + \lambda$; $y = \bar{\delta}$

where α, β, δ and λ are the small distortions from being on a (1/4, m/4, n/4) site.

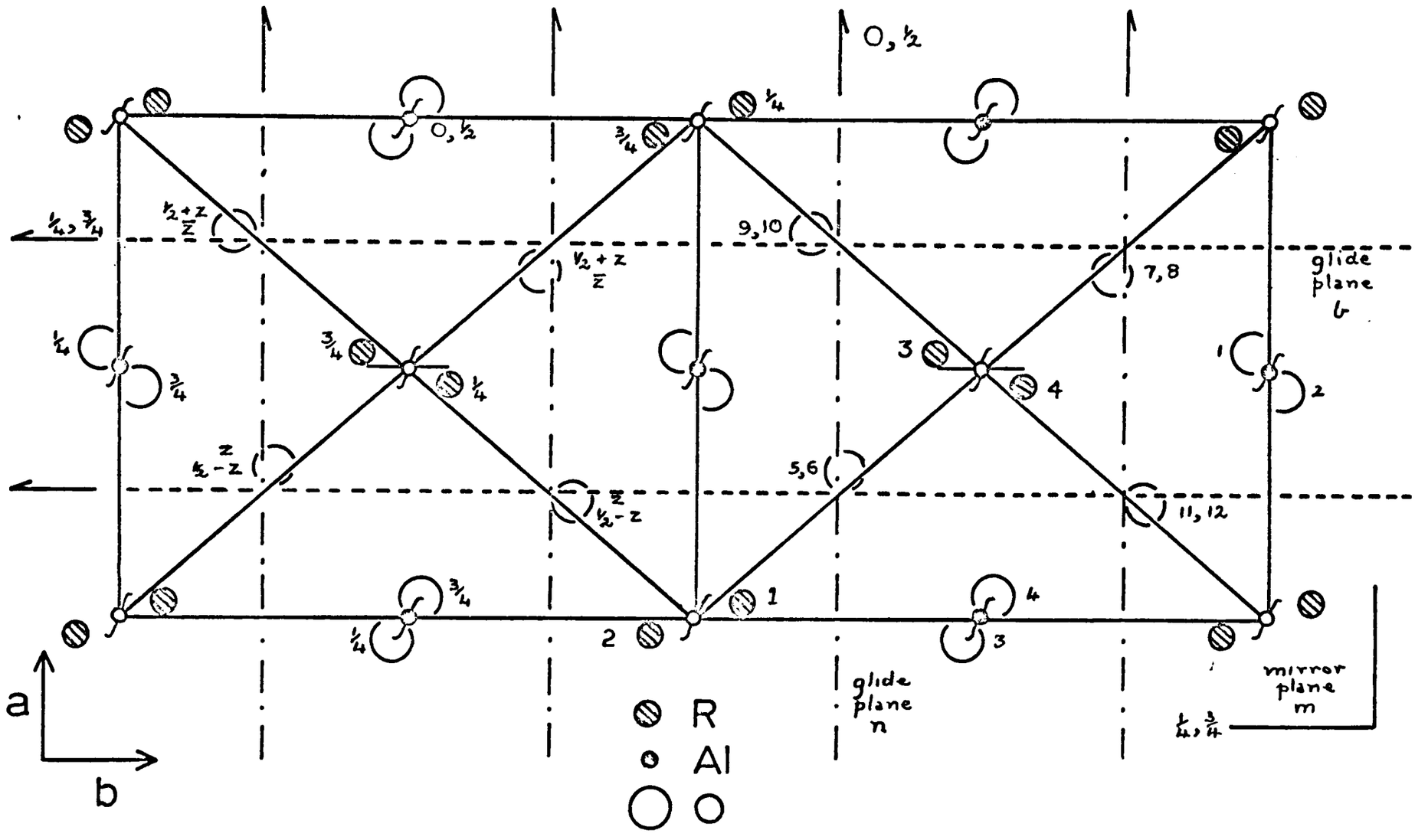


Fig 1-8 Symmetry Elements in Pbnm

Crystallographically, all four rare earth sites are equivalent as can be seen from Figs.1-7 & 1-8. If we start with ion 1 then it is related to ion 4 by the glide plane b and to ion 3 by the diagonal glide n. The inversion centre through the Al site connects 1 to 2', equivalent to 2 in the next unit cell.

Magnetically, sites 1 and 2 are equivalent and sites 3 and 4 are equivalent. The c-axis is a principal axis of the self-energy ellipsoid for both sites. The other two principal axes lie in the a-b plane in such a fashion that one set can be obtained from that belonging to the other site by a reflection in either the a-c or b-c plane. Thus for an external field in either the a-c or b-c plane, all four sites are magnetically equivalent.

1-4. Growth and Orientation of $RAlO_3$ Specimens.

The close connection between the orthorhombic structure of the rare earth aluminates and the undistorted perovskite structure is brought out very strongly by a study of the growth habit of the crystals. Instead of growing along the new axes as one would expect, the (100) and (010) faces are never observed, and the crystal grows along the pseudo-cubic axes to give monoclinic single crystals.

However, because the angle β of the monoclinic cell is very close to 90°, twinning occurs very easily, making the growth of large single crystals difficult. By contrast, single crystals of the isomorphous $GdFeO_3$, which has β = 92.8° can be obtained reasonably easily.

Flux growing is the only method which has so far successfully produced large single crystals of these compounds. This method has the two big advantages of considerably lowering the temperature at which growth can take place, and enabling one to control the growth and nucleation rates. The first advantage is important in these compounds because growth from the melt can only take place at about 2000°C, which requires more complicated furnace equipment, and the highly twinned nature of the resulting crystals indicates that there is possibly a crystallographic transition between this temperature and the flux melt temperature.

The crystals used in the experiments in this thesis were all grown by Mrs.B.M.Wanklyn in this laboratory and only a brief description of the methods used will be given here.

Crystals of $GdAlO_3$ can be grown[12] from a mixture of Gd_2O_3 and Al_2O_3 with several different fluxes

such as PbO/PbF_2 and Bi_2O_3/B_2O_3. However best results were obtained from a $PbO/PbF_2/B_2O_3$ flux to which a small amount of PbO_2 was added to provide an initially oxidizing atmosphere. The B_2O_3 included amounted to only 2% of the total weight, but it plays a very important part in reducing spontaneous nucleation, possibly by reducing the melt viscosity.

The melt was heated to 1290°C and then cooled at 2°C/hr to 790°C in a muffle-type furnace with a downward temperature gradient of 5°C. After completion of the cooling the flux could be removed by boiling in 1:5 HNO_3.

The crystals obtained were very clear, although some contained small but clearly visible inclusions of flux. A large single crystal 6 x 5 x 5mm was chosen for use in the moment and susceptibility measurements and 5gm of good, clear crystals picked out to make up the specific heat sample.

An analysis by Johnson Matthey Chemicals Ltd. on some crystals from the specific heat sample gave the results:

Gd:	69.0 ± 0.5 wt%	(67.8 wt%)
Pb:	0.3 ± 0.5 wt%	(-)

where the figures in brackets are the theoretical proportions for $GdAlO_3$.

Crystals of $DyAlO_3$ could not be obtained[12] from a Bi_2O_3/B_2O_3 flux, but were able to be grown from a $PbO/PbF_2/B_2O_3$ flux. Excess Dy_2O_3 and a high PbO/PbF_2 ratio were necessary to avoid the garnet phase. The best crystals were obtained by slow evaporation of the solution in the flux at constant temperature. The melt was left at 1220°C in a platinum crucible for ten days while a 1mm slit between the crucible and its lid allowed the solution to evaporate.

Again the flux was dissolved in 1:5 HNO_3 and the best resulting single crystal measured 5 x 3 x 2mm. All the resultant crystals were yellowish-brown in colour making the selection of good crystals for specific heat measurements much more difficult. However an analysis by Johnson Matthey on the specimen gave:

Dy:	67.6 ± 0.5 wt%	(68.4 wt%)
Pb:	0.3 ± 0.5 wt%	(-)
Al:	11.7 ± 0.5 wt%	(11.4 wt%)

showing that again very little flux had been included in the crystals.

Since both sets of crystals transmitted light

easily, a polarizing microscope was used to select single crystal specimens. Orientation of the crystals could then be achieved by making use of the natural faces of the crystal and a knowledge of the growth habit.

As already mentioned, the series of compounds grows along the monoclinic pseudo-cell directions with the c-axis common to both the monoclinic and orthorhombic cells (Fig.1-7). Since the convention for labelling orthorhombic axes is $a < b < c$, therefore the orthorhombic b-axis must subtend the angle β of the monoclinic cell.

The angles between the monoclinic faces of the single crystal were then measured on an optical goniometer, thus determining the orthorhombic axes. The whole operation could also be performed on a polarizing microscope alone. When extinction was obtained with the crystal lying in turn on its three (almost) perpendicular faces it was found that in two cases the crystal faces were parallel to the axes of the polaroids and in the third they were at 45°. This latter face is the a-b plane.

The angles between the sides of this face were then measured by aligning them in turn with the cross-hairs of the microscope, and again the b-axis was determined by being opposite the larger angle. Measurement

of angles in this way can be achieved to $\pm 0.1^{\circ}$.

Back reflection X-ray photographs were also taken along the three orthorhombic directions and comparison with these photographs was the only method of orienting crystals without sufficient natural faces to use the first method.

To enable calculation of the demagnetizing factor for correction of the moment and susceptibility measurements, both single crystals chosen were ground down to rough spheres on a diamond wheel. After this operation the $GdAlO_3$ crystal had a diameter of 4mm and a mass of 283mgm and the $DyAlO_3$ crystal a diameter of 2mm and a mass of 78mgm.

1-5. Magnetic Ordering Arrangements in $RAlO_3$ Crystals.

The allowed magnetic ordering arrangements for both the A and B sites in the distorted perovskite structure Pbnm have been worked out by Bertaut[13] and for the A sites also by Hawkes[14] using the theory of magnetic space groups. The derivation will not be repeated here, but some consideration of the results will be of assistance when interpreting the experimental results.

However before detailing the results for the rare earth sites we should first consider the two limitations of the method. The magnetic point group is derived from the crystallographic point group by addition of the time reversal operator and then combination with the coloured Bravais lattices gives the magnetic space group. As so derived, its physical dimensions are identical with those of the crystallographic unit cell, and thus automatically exclude possible magnetic arrangements which require a larger unit cell.

For the two crystals with which we are principally concerned, this restriction does not matter since, a posteriori, the correct magnetic ordering arrangements are obtained.

The second problem is that there has been no experimental verification that there is not a distortion in the crystal structure of $GdAlO_3$ when passing through the Neel temperature. In the case of $DyAlO_3$, neutron diffraction experiments[15] have shown that there is no crystallographic transition.

Returning to the results, it is found that there are eight allowed magnetic arrangements - four with spins in the a-b plane and four with spin direction confined to

the c-axis. Canting is allowed in the a-b plane but is not allowed between the c-axis and the a-b plane.

Table 1-I sets out the spin arrangements and they are shown pictorially in Fig.1-9. The method of site numbering is the same as that adopted in Fig.1-7 and we recall that there are only two magnetically inequivalent sites with 1 = 2 and 3 = 4.

The two conventions of nomenclature for the magnetic groups have both been listed. The first, derived from the shortened International symbol for the crystallographic space group, adds a prime to those elements with which we have associated the time reversal operator.

The second system, due to Bertaut, uses the four symbols F, G, C and A subscripted with one of the crystal axes x, y or z. The main symbol refers to the components of the spins along the axis denoted by the subscript, and has the meaning:

F (+ + + +) Ferromagnetic.

G (+ - + -) Nearest neighbours anti-parallel.

C (+ + - -) Lines of similar spins along c-axis.

A (+ - - +) Planes of similar spins in a-b plane.

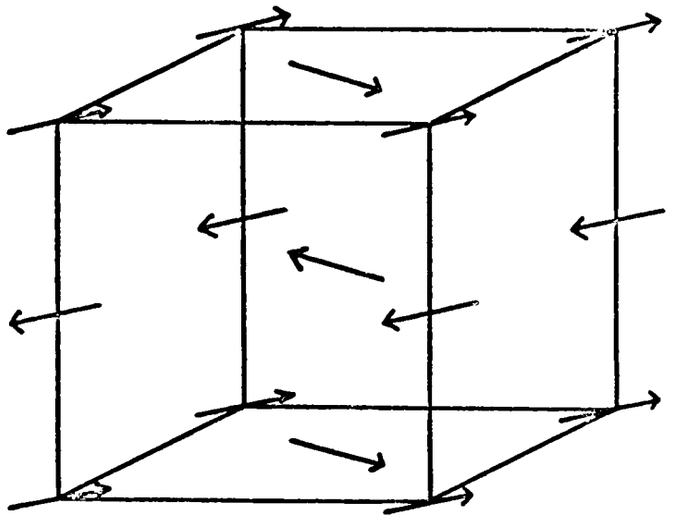
where + and - denote up and down spins on the four sites in turn.

TABLE 1-I

$RAlO_3$ - Allowed Spin Configurations.

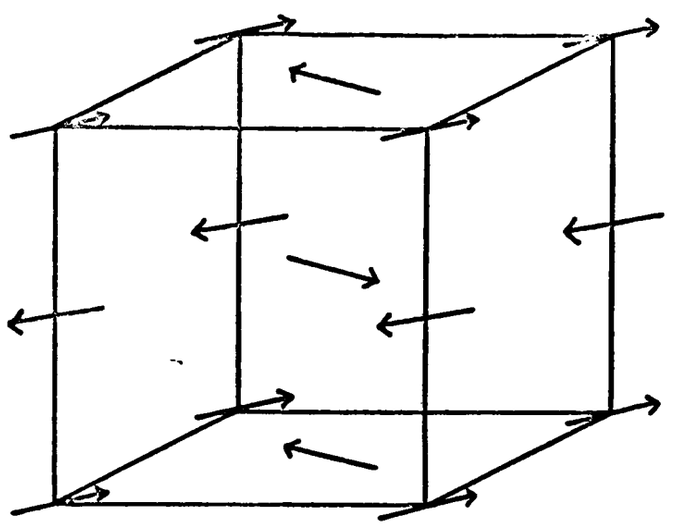
	C_z Pbnm			F_z Pb'n'm			C_xF_y Pb'nm'			F_xC_y Pbn'm'		
Site	S_x	S_y	S_z	S_x	S_y	S_z	S_x	S_y	S_z	S_x	S_y	S_z
1	0	0	↑	0	0	↑	↑	±↑	0	↑	±↑	0
2	0	0	↑	0	0	↑	↑	±↑	0	↑	±↑	0
3	0	0	↓	0	0	↑	↓	±↑	0	↑	±↓	0
4	0	0	↓	0	0	↑	↓	±↑	0	↑	±↓	0

	A_z Pb'nm			G_z Pbn'm			A_xG_y Pbnm'			G_xA_y Pb'n'm'		
Site	S_x	S_y	S_z	S_x	S_y	S_z	S_x	S_y	S_z	S_x	S_y	S_z
1	0	0	↑	0	0	↑	↑	±↑	0	↑	±↑	0
2	0	0	↓	0	0	↓	↓	±↓	0	↓	±↓	0
3	0	0	↓	0	0	↑	↓	±↑	0	↑	±↓	0
4	0	0	↑	0	0	↓	↑	±↓	0	↓	±↑	0



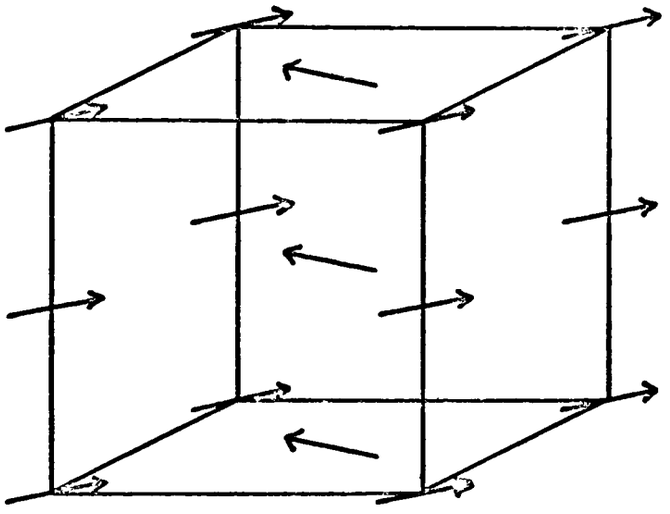
G_xA_y

Pb'n'm'



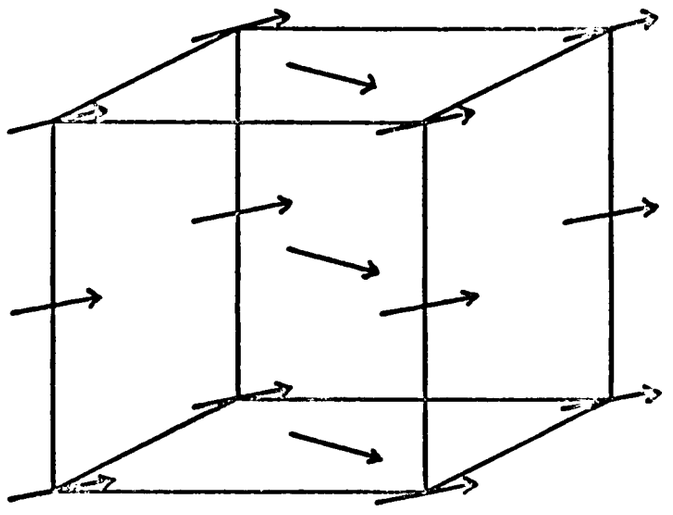
A_xG_y

Pbnm'



F_xC_y

Pbn'm'



C_xF_y

Pb'nm'

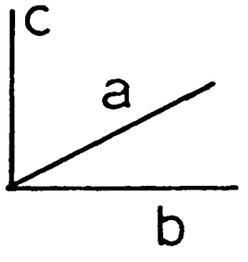
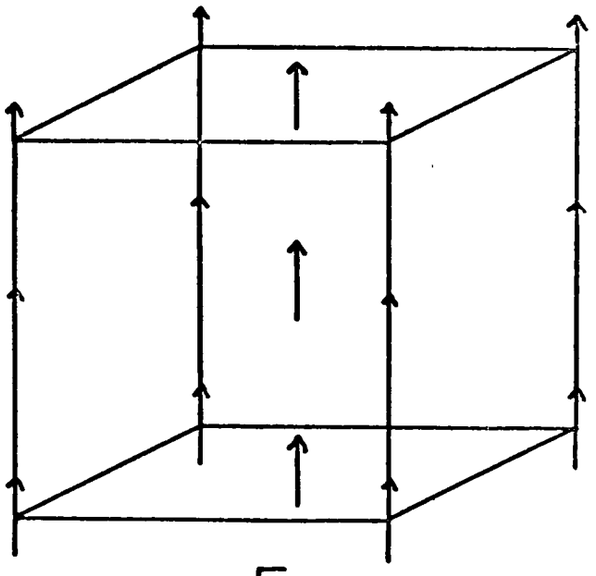


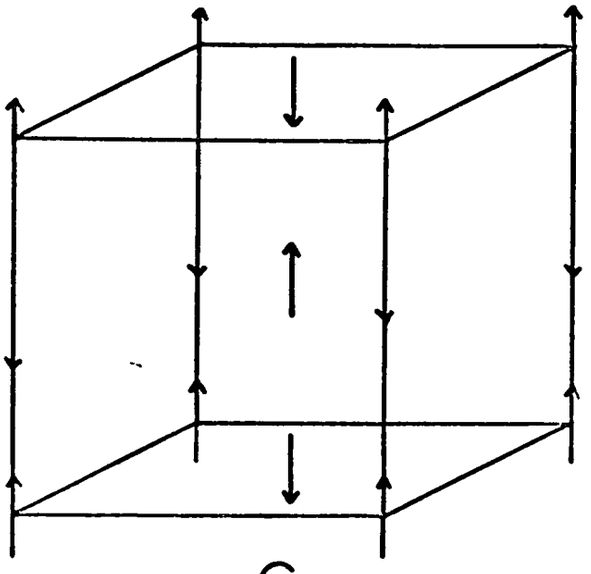
Fig. 1-9(a)

Magnetic Ordering Arrangements



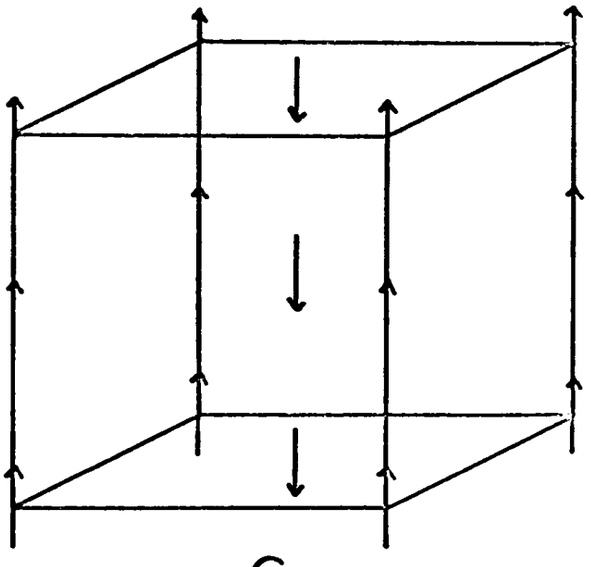
F_z

Pb'n'm



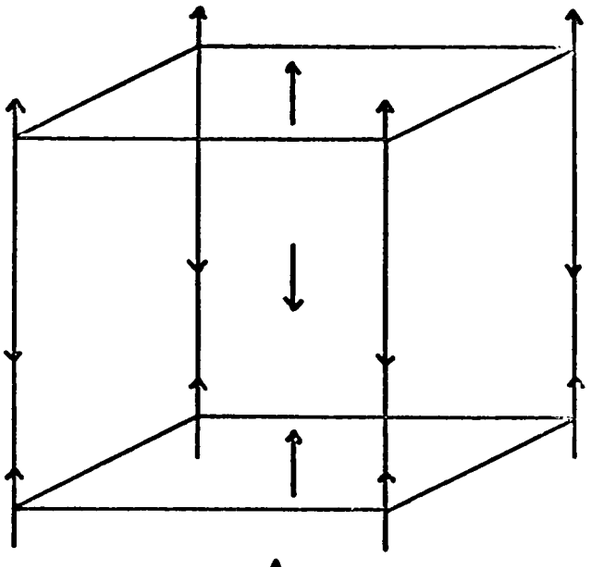
G_z

Pbn'm



C_z

Pbnm



A_z

Pb'nm

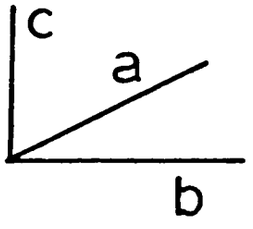


Fig 1-9 (b)

CHAPTER TWO

GADOLINIUM ALUMINATE - EXPERIMENTAL RESULTS.

2-1. Introduction.

The simplest model of an antiferromagnet is one in which all the magnetic ions are divided into two sublattices in such a way that an ion on one sublattice has nearest neighbours only of ions on the other sublattice, and the two sublattices have their direction of net spontaneous magnetization antiparallel. It is fortunate that in $GdAlO_3$, with its nearly simple cubic sub-structure of magnetic ions, very many of the experimental results can be explained on the basis of this simple picture.

Since Gd^{3+} is an S-state ion we would expect any exchange effects to be isotropic and to be suitably expressed by the Heisenberg Hamiltonian:

$$\mathcal{H}_i = -2 \sum_{i<j} J_{ij} \underline{S}_i \cdot \underline{S}_j$$

where the summation is over pairs of equivalent neighbours of type j. In fact we shall find that this exchange is the dominant interaction and that we only

need consider the case where ion j is a nearest neighbour to ion i. We therefore get:

$$\mathcal{H}_i = -2J \sum_{nn} \underline{S}_i \cdot \underline{S}_j$$

where the summation is now over pairs of nearest neighbours.

The other type of internal interaction which we shall need to consider is that due to the crystalline electric field (CEF). The CEF interacts only with the orbital magnetic moment which is zero for a true S-state ion. However spin-orbit coupling slightly reduces the S-state degeneracy, allowing a small orbital moment for the CEF to act on. The CEF interaction in Gd^{3+} is therefore very much smaller than in most rare earth ions where CEF splittings of a few hundred degrees are typical. However we shall see that it does have very profound effects on the experimental results, and finally forces us to change our simple two sublattice approach and consider a more complicated picture.

Following the next section, which deals with measurements on $GdAlO_3$ by other workers, the remainder of the chapter will be devoted to describing the experimental results obtained from measurements of the specific heat, magnetic susceptibility and magnetic

moment. Some interpretation and evaluation of results will be given as they arise, e.g. those for which it is meaningful or helpful to consider under the two sublattice picture. However those interpretations which require the use of the CEF interaction and those which are comparisons between the three types of experiments will be left until the following chapters, when we will have a clearer overall picture of the results and the inadequacies of not considering the CEF interaction.

2-2. Other Magnetic Measurements.

The main published work which has been carried out on undoped $GdAlO_3$ is by Blazey and Rohrer[16] who measured the susceptibility and moment along the principal directions. Their measurements covered the range 1.3 - 100°K and 0 - 200kOe in a pulsed field magnet and they obtained a Néel temperature of 3.89°K.

Their method of taking measurements was to record the time derivatives of the magnetic field, $\partial H/\partial t$, and of the magnetization, $\partial M/\partial t$. Division of these two results on an analogue function generator gives the differential susceptibility $\partial M/\partial H$. In their first paper they quoted the susceptibility as:

$$\chi = \frac{C}{T + 14}$$

and in the second paper as:

$$\chi = \frac{7.99}{T + 4.6}$$

the latter measurement being in good agreement with ours.

However, on integration of the $\partial M/\partial t$ signal to obtain the magnetization, the saturation value obtained was temperature dependent, extrapolating to 7 Bohr magnetons at $T = 0^{o}K$. This is in direct disagreement with our measurements and we feel that it is a relaxation time phenomenon associated with using a pulsed field magnet.

Blazey and Rohrer did not observe any anisotropy between different directions in the a-c plane, but did obtain an anisotropy difference of 3.3kOe between the b-axis and the a-c plane. This anisotropy difference they attributed entirely to dipole-dipole interactions.

From their measurements they found that the only ordering scheme which gave consistent results was one with all nearest neighbours antiparallel. The values obtained for the nearest neighbour and next nearest neighbour exchange constants were:

$$J_1/k = -0.07^{\circ}K$$
$$J_2/k = -0.003^{\circ}K.$$

The optical spectra of Er^{3+} and Dy^{3+} doped crystals of $GdAlO_3$ has been studied by Hawkes[14]. These two ions are very anisotropic, and from comparison of the splittings at $1.4^{\circ}K$ in zero field and above magnetic saturation, Hawkes estimated that nearest neighbour Gd^{3+} ions are canted about 20° from the b-axis in the a-b plane.

The reason for this large angle is that the principal axis of the crystal field, as seen by the Er^{3+} and Dy^{3+} ions, is within 20° of the pseudo-cubic axes, being slightly nearer the orthorhombic a- or b-axis for different energy levels. We shall return to this later when considering the crystal field axes for the gadolinium ions.

From an extrapolation to zero applied field of the field dependent line shifts above magnetic saturation, Hawkes also deduced that the most likely mode of ordering was the one in which all nearest neighbours are antiparallel.

He also observed the spin flop when the external field is applied parallel to the b-axis, and his value

for the "flopping field" of 11.4kOe agrees well with the 11.5kOe obtained by Blazey and Rohrer. By observing the change in the spin flop on rotating the crystal away from the b-axis in the a-b plane, Hawkes suggested that it was most likely that the spins flop in the b-c plane.

From the width of the optical absorption lines Hawkes suggested that there was a small crystal field interaction with a total splitting of the $^8S_{7/2}$ ground state $\lesssim 1^oK$.

White et al.[17] have studied the e.s.r. spectra of Gd^{3+} and Fe^{3+} in the isomorphous, diamagnetic host $YAlO_3$. Their main conclusion which is of relevance here was that the CEF principal axis at the rare earth site was at 28^o to the a-axis in the a-b plane. This result is different to our conclusions in Chapter 4 where we suggest that the principal axis for $GdAlO_3$ is between the b-axis and 45^o to the b-axis (pseudo-cubic axis), although still in the a-b plane.

However doubt is cast on the relevance of the results of White et al. by comparison with the work of Boesch et al.[18] on the n.m.r. of Al^{27} in $GdAlO_3$. The principal axes of the electric field gradient as determined by n.m.r. should be identical with the principal axes of

the e.s.r. crystal field term, V_2. But there is no correlation between White's results for the Fe^{3+} ion in the aluminium site and the results of Boesch unless one reverses the axes a ↔ b in one set of results. The agreement is then almost perfect. The solution of this dilemma is not apparent - either there is a difference in the distortions from cubic symmetry between the $GdAlO_3$ and $YAlO_3$ structures so as to cause this reversal or else there has been a mistake in identification of axes.

2-3. Specific Heat Measurements.

Measurements were made of the specific heat through the range 0.6° - 11°K, which was sufficient to determine the magnetic contribution accompanying the ordering transition. The magnetic specific heat is shown in Fig.2-1 in which the most prominent feature is a lambda-anomaly, characteristic of a phase transition - in this case a magnetic phase transition.

All the measurements were made on a 5gm polycrystalline specimen except for the lowest part of the temperature range from 0.6° - 1.4°K for which the mass was reduced to 1gm in order to reduce the time taken to cool down. The heating interval used varied from

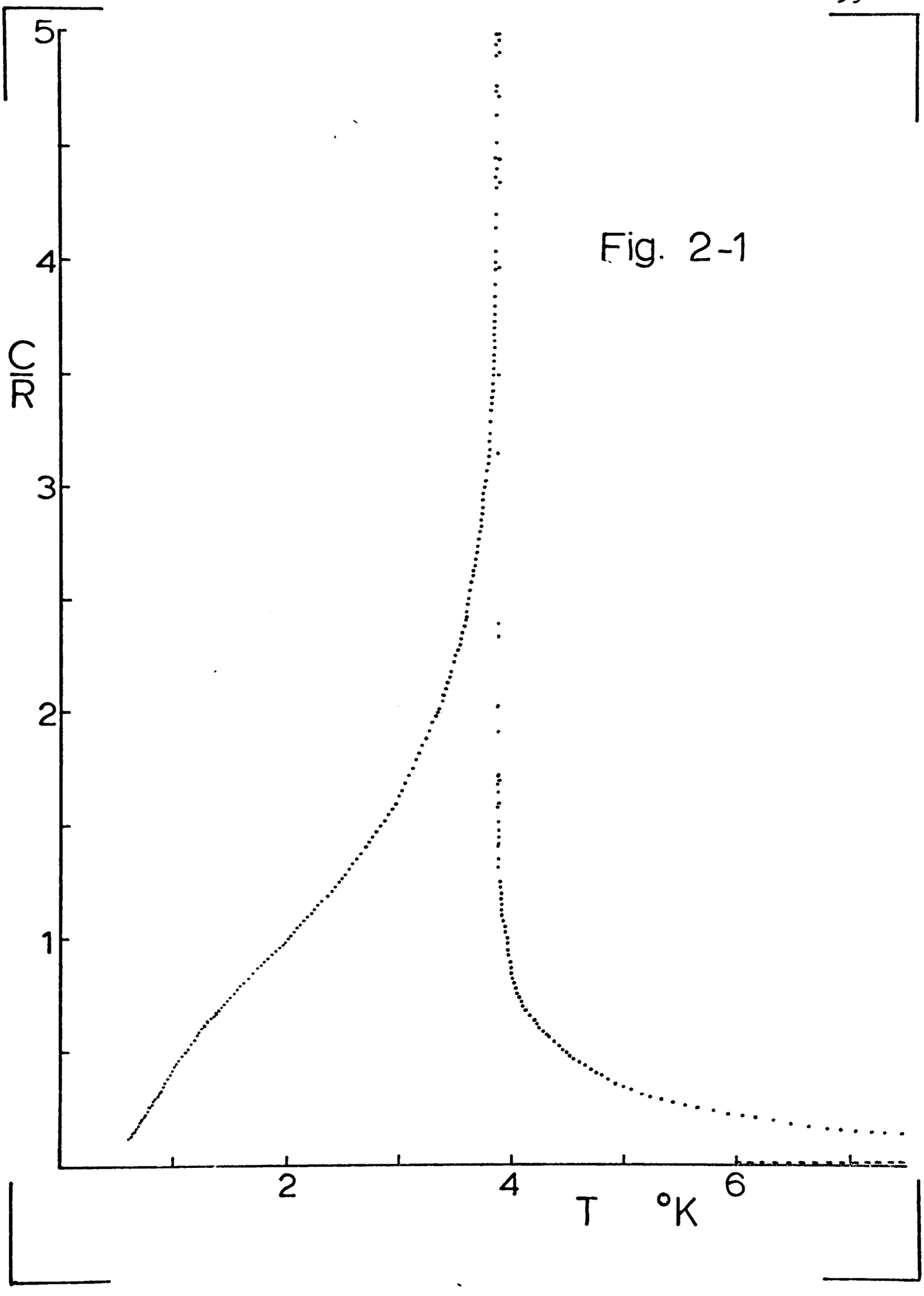


Fig. 2-1

1mdeg in the vicinity of the transition to nearly 200mdeg at $10^{\circ}K$.

The broken curve shown in Fig.2-1 is the lattice contribution which has been subtracted from the measured specific heat. Estimation of the lattice contribution was made by assuming that at these low temperatures it is proportional to T^3, and that the magnetic part far above the lambda-anomaly is proportional to $1/T^2$. The coefficients of these two terms were then determined by plotting CT^2/R against T^5. From the well-defined linear portion between 8° and $11^{\circ}K$ the values

$$C/R = 5.85/T^2 + 2.4 \times 10^{-5} T^3$$

were obtained.

From the coefficient of the T^3 term we can deduce an effective Debye temperature of $214^{\circ}K$. If we now consider the approximation formula for estimation of the Debye temperature from the melting point of a monatomic solid:

$$\theta_D^2 = \frac{9\hbar^2 T_M}{x^2 k M V^{2/3}}$$

where x is a constant ≈ 0.22

T_M is the melting point ($=2343^{\circ}K$)

V is the volume of a unit cell

and M is the mass of one atom,

we find that substituting the atomic mass of gadolinium for M gives a value for θ_D of 206°K.

This close agreement shows that we have chosen the correct value for the mass, confirming that at low temperatures only the heaviest atom is thermally excited. This is expected since only lattice modes having

$$\hbar\omega \leq kT$$

can be thermally excited at temperature T, and the heaviest atom will take part in the lowest frequency modes.

Fig. 2-2 shows the specific heat near the ordering transition on an extended scale. The peak is slightly rounded over a range of 3mdeg near T_N as has been observed in many other specific heat measurements[19]. The effect is due to the fact that we are not measuring a pure, infinite single crystal and all imperfections such as random impurities, both chemical and isotopic, dislocations, vacancies and surface effects have been shown to contribute to the rounding[20]. The fact that the rounding takes place over only 3mdeg is an indication of the good quality of the crystals as rounding up to 15mdeg[21] have been reported in the literature.

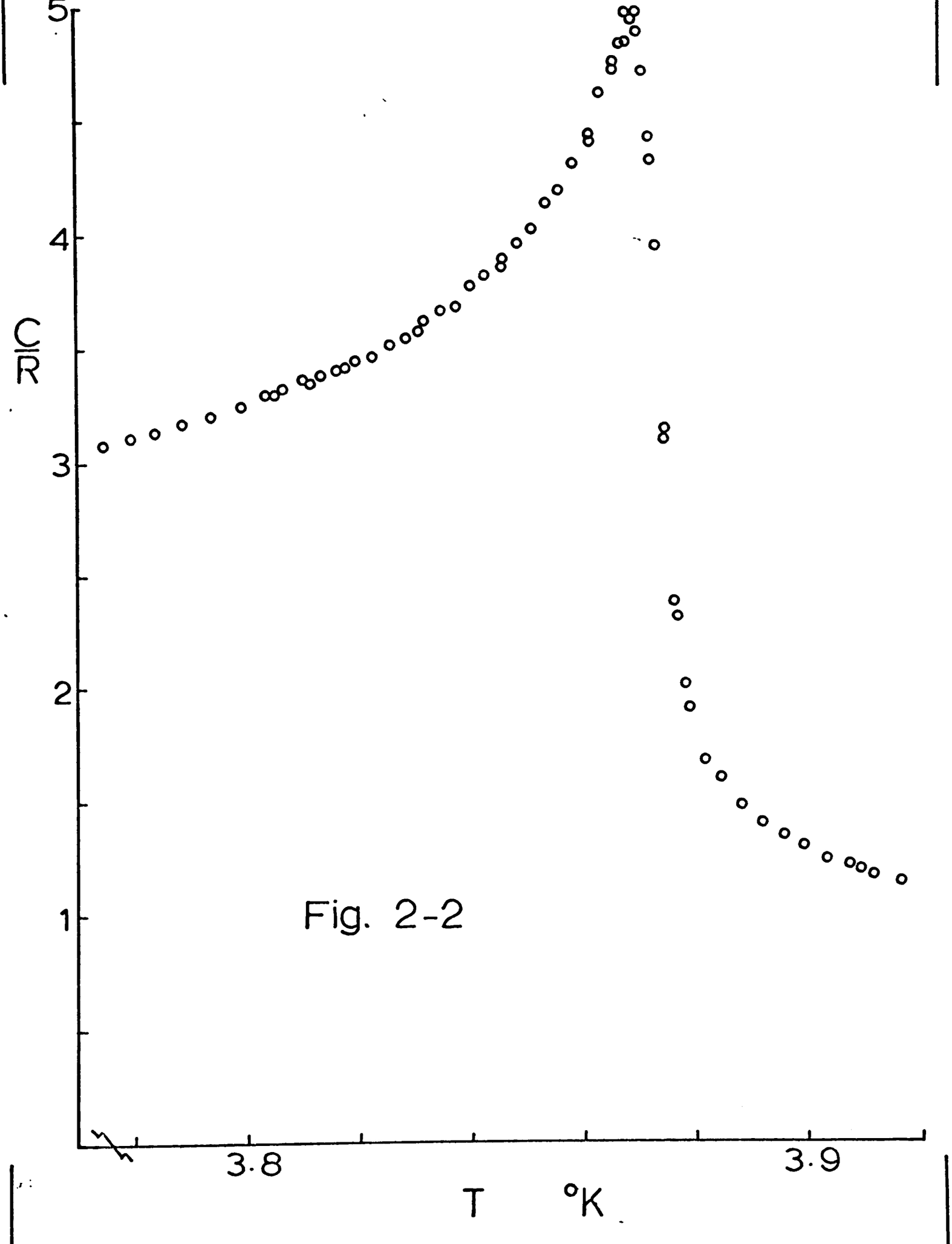


Fig. 2-2

Extension of the approach to T_N in a smooth curve (dotted in Fig.2-2) shows that one would expect the true transition temperature to be 3.870°K. Following Wolf et al.[22] we can obtain a better estimate by using a Mangelsdorf retarded function plot, which was developed[23] as a means of estimating the x-coordinate at the divergence of a logarithmic singularity. As can be seen from Fig.2-3, this method also gives the transition temperature as 3.870°K.

The construction of the plot is carried out by reading temperatures spaced at equal intervals of specific heat and plotting $T(C+\delta C)$ against $T(C)$. The point of divergence is where this line cuts the 45° line $T(C+\delta C) = T(C)$. The method is strictly only true for a logarithmic singularity and as we shall see only the approach to the critical temperature from below is of this form. If applied to the high temperature side an erroneous answer is obtained as has been shown by Wolf et al.

To obtain the form of the singularities above and below the ordering temperature, logarithmic plots were done as shown in Fig.2-4. Fig.2-4(a) shows a semi-log plot of specific heat against $|1 - T/T_N|$ with $T_N = 3.870°$.

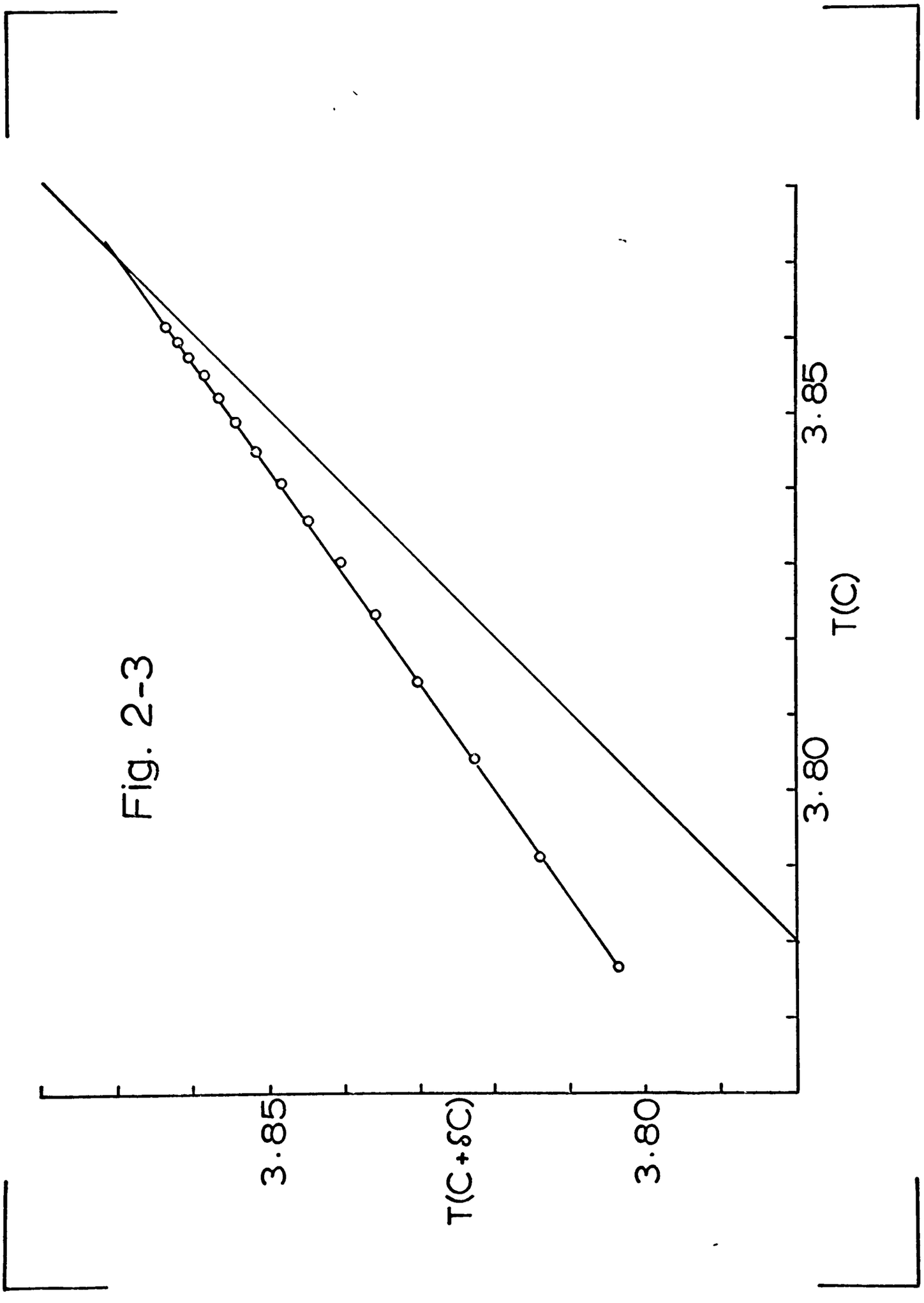
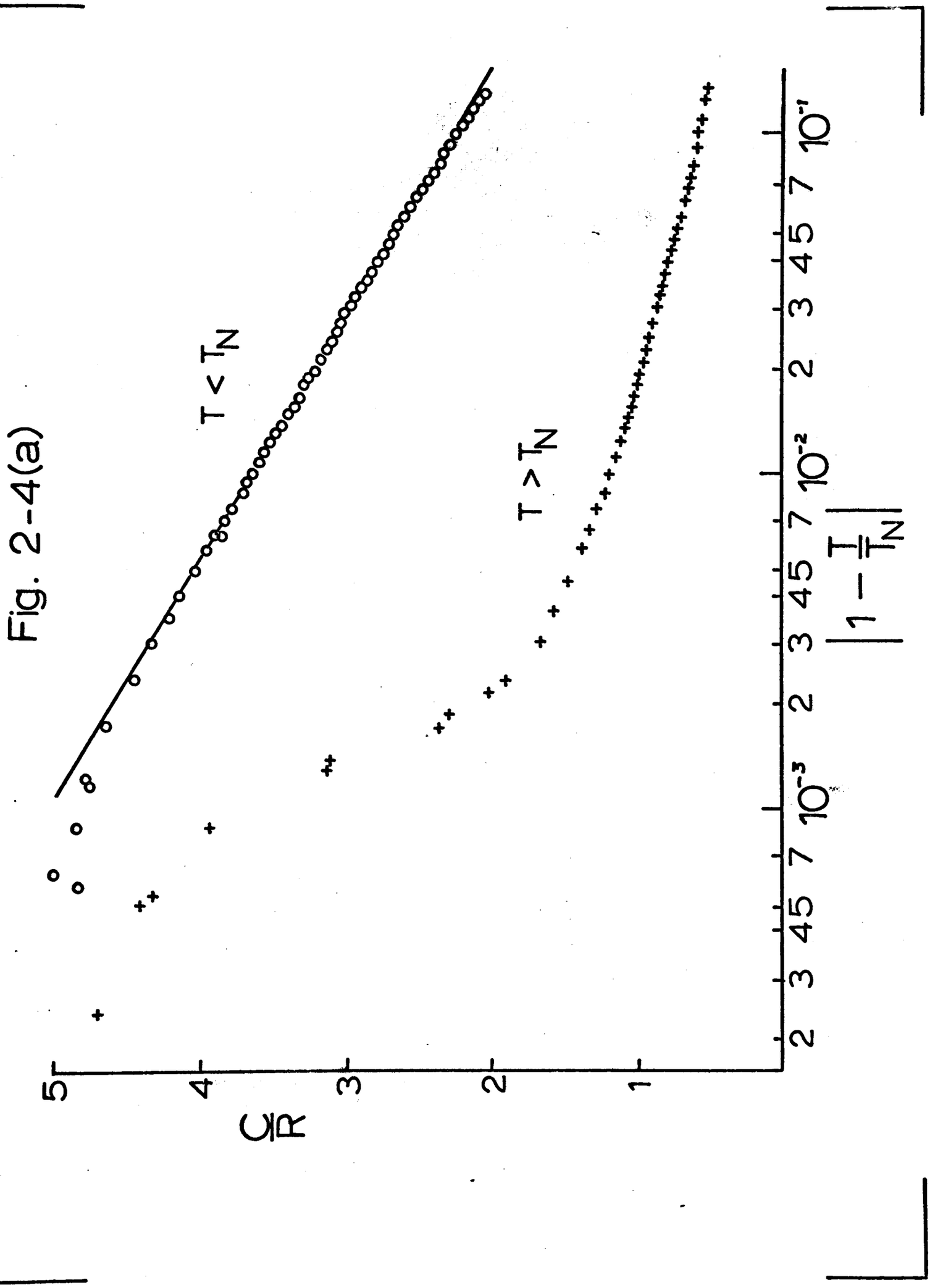


Fig. 2-3


Fig. 2-4(a)
T < T_N
T > T_N
C/R
5
4
3
2
1
2 3 45 7 10^-3 2 3 45 7 10^-2 2 3 45 7 10^-1
|1 − T/T_N|

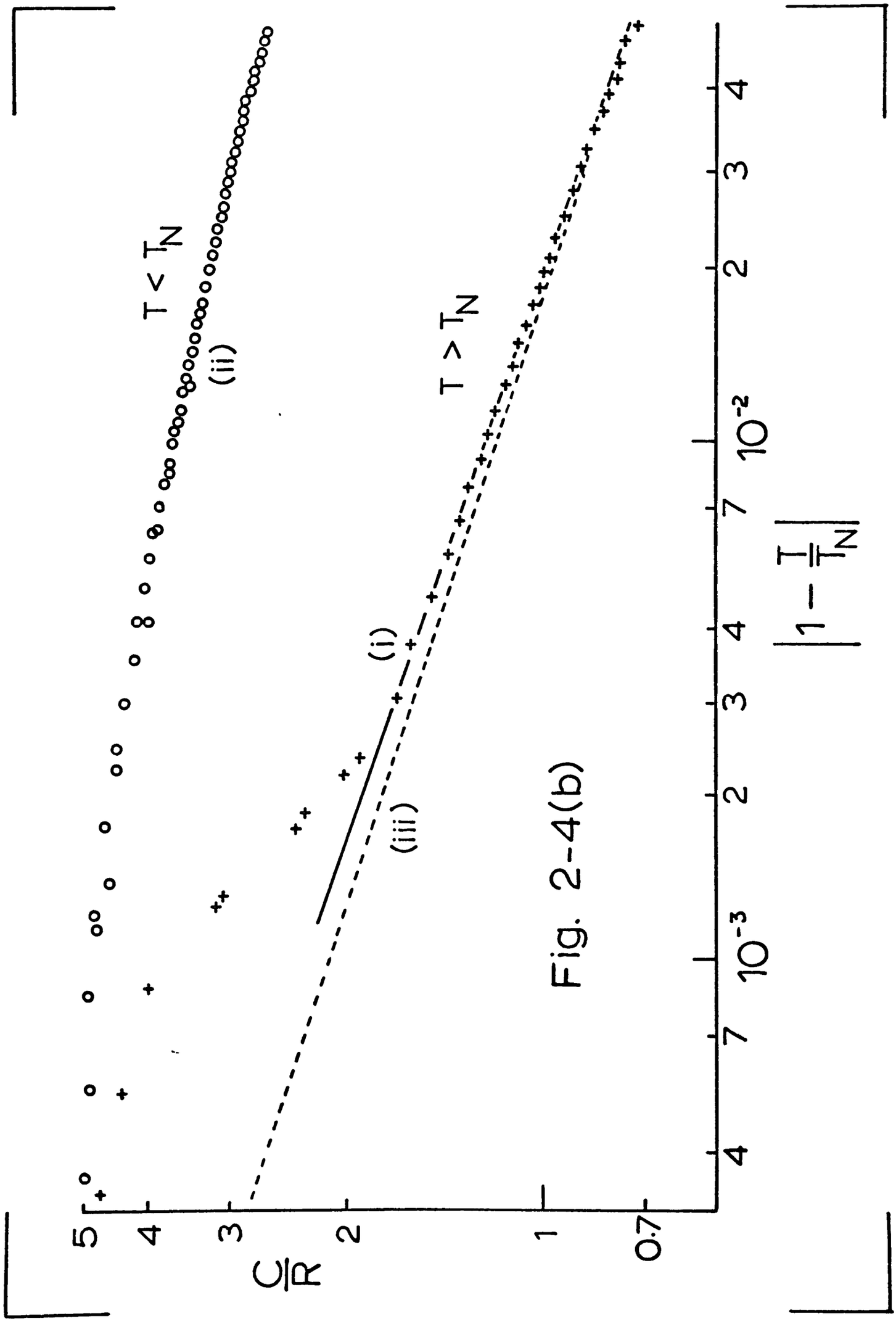

C/R
5
4
3
2
1
0.7
4
7
10^{-3}
2
3
4
7
10^{-2}
2
3
4
$\left|1-\frac{T}{T_N}\right|$
$T < T_N$
(ii)
$T > T_N$
(i)
(iii)

Fig. 2-4(b)

It can be seen that the points for $T<T_N$ fit a good straight line over the region $4\times10^{-3}<(1 - T/T_N)<10^{-1}$, the equation of which is:

$$C/R = -0.605 \ln(1 - T/T_N) + 0.847$$

but the points for $T>T_N$ do not fit a good straight line over any reasonable part of the region.

In Fig.2-4(b) the points have been replotted on a log-log scale and it can now be seen that the points for $T>T_N$ fit a good straight line in the region $3\times10^{-3}<|1 - T/T_N|<5\times10^{-2}$. The equation of this line is:

$$C/R = 0.321\,|1 - T/T_N|^{-0.292}$$

It can be seen that this curve deviates upwards from the straight line at $|1 - T/T_N| = 3\times10^{-3}$ before bending back again where the rounding near T_N takes place. This upward deviation can be removed by choosing $T_N = 3.874^{\circ}K$ instead of $3.870^{\circ}K$ as shown in curve (iii) of Fig.2-4(b). However this curve then deviates away from the straight line sooner as T recedes from T_N. In view of this we have decided that curve (i) represents more accurately the behaviour of a pure infinite single crystal with its Néel temperature of $3.870^{\circ}K$.

As yet we can not put forward any detailed explanation of why the curve should first deviate upwards as T approaches T_N. However as this is the region in which the short range order is changing over to long range order, it is conceivable that the last pockets of disorder or reverse spin short range order could disappear with a rush, i.e. even faster than predicted on the existing crystal models.

An effect similar to this divergence has been explained[24] in measurements of the sublattice magnetization of ferromagnets, which should vary as $(1-T/T_c)^{\beta}$ near the Curie temperature with β approximately equal to 0.33. However for $(1-T/T_c) < 10^{-3}$, β has been observed to change from 0.33 to 0.50 due to the long range dipole-dipole interaction rapidly changing in importance. However in $GdAlO_3$ we shall see later that the dipole-dipole interaction is very small so perhaps some other mechanism, e.g. chemical impurities which may greatly change the local anisotropy, is responsible for the effect on the specific heat curve.

There are, as yet, no theoretical predictions for the accurate shape of the approach to the specific heat singularity for the three dimensional Heisenberg

model, even with only nearest neighbour exchange interactions. For the three dimensional Ising model Gaunt[25] has calculated that the specific heat should diverge as $|1-T/T_N|^{-\alpha}$ with $\alpha = 1/8$ both above and below the critical temperature, regardless of the type of three dimensional lattice.

However for the Heisenberg model[26], the value of α below T_N, is believed to be $\gtrsim 0$, where $\alpha = 0$ corresponds to a logarithmic divergence. Above T_N, the only theoretical information is that $\alpha > 0$, and there seems to be little correlation between the reported experimental values. The range of experimental values can of course be due to the fact that not all compounds whose behaviour is compared with the theory for nearest neighbour Heisenberg exchange actually correspond very well to that ideal system.

Moving away from the critical region the theory of Eisele and Keffer[27] predicts that at temperatures very much lower than the spin wave gap ($T_{AE} = 1.55^{\circ}K$) the specific heat should be proportional to $\exp(-T_{AE}/T)$. In the range $T_{AE} \ll T \ll T_N$ the specific heat should be proportional to T^3.

We did not observe substantiation of either of

these two predictions. In the first case it is possible that our measurements do not extend to sufficiently low temperatures while the required region for the T^3 law can be hardly said to even exist in a crystal for which $T_{AE} = 0.4T_N$.

The total entropy under a magnetic specific heat anomaly should be: R ln(2S+1), where S is the effective spin of the ground state just above the ordering temperature. However the distribution of the entropy above and below T_N depends on the specific form of the magnetic interaction and can thus be compared with the various models for magnetic ordering. Similarly the amount of energy absorbed in heating the sample through the magnetic anomaly can also be obtained from the specific heat curve and this is also sensitive to the form of the magnetic interaction.

The experimental values for these quantities are set out in Table 2-I together with the values for four theoretical models. Since the measured entropy is only 2.4% less than R ln 8 it is evident that an effective spin of 7/2 is the correct one to describe the system. This confirms that above the Néel temperature J is still a good quantum number and therefore the Gd^{3+} ion still has

TABLE 2-I

			$\frac{S_\infty - S_0}{k}$	$\frac{S_\infty - S_N}{k}$	$\frac{E_\infty - E_N}{kT_N}$	$\frac{E_\infty - E_0}{kT_N}$
$GdAlO_3$			2.030	0.280	0.406	1.465
Heisenberg	s.c.	S=7/2	2.079	0.40	0.67	1.67
Heisenberg	f.c.c.	S=7/2	2.079	0.31	0.46	1.49
Heisenberg	sq.	S=7/2	2.079	1.03	1.75	-
Ising	s.c.	S=7/2	2.079	0.15	0.24	1.40

its free-ion orbital S-state. Under these conditions we would therefore expect the main magnetic interaction to be of the isotropic Heisenberg form as pointed out in the previous section.

Comparison of the experimental values with those for the Heisenberg simple cubic system shows that the agreement is not as good as one might have expected. Agreement with the Heisenberg face centred cubic system is much better, and since the main difference between the two is that the f.c.c. lattice has twelve nearest neighbours compared with six for the s.c. lattice, it raises the problem of whether we need to consider next nearest neighbour exchange in order to increase the number of interacting ions.

The answer however is not to be found in next nearest neighbour exchange, but in the one remaining significant feature of the specific heat curve which we have so far not mentioned - the bump at about $1^{o}K$ which is a Schottky anomaly due to the crystal field interaction. We shall show in Chapter 4 that when we have obtained an estimate for the size of the CEF splitting and incorporated it into the values for the energy that agreement with the simple cubic Heisenberg model becomes very good.

2-4. Susceptibility Measurements.

The magnetic susceptibility was measured along the three orthorhombic axes of the single crystal sphere described in Section 1-4. In the pumped hydrogen range the measurements were made using the a.c. mutual inductance apparatus, and the results fitted to the Curie-Weiss law:

$$\chi = \frac{C}{T - \theta} .$$

The values obtained along the a,b and c axes respectively were:

$$\chi_a = \frac{8.11}{T + 4.89}$$

$$\chi_b = \frac{8.09}{T + 4.70}$$

$$\chi_c = \frac{8.13}{T + 4.84}$$

As can be seen, the values for the Curie constant, $Ng^2\beta^2S(S+1)/3k$, are consistent to $\pm 0.25\%$ and the mean value of 8.11 is 3% higher than the theoretical value of 7.875 for $S = 7/2$ and $g = 2$. This is in good agreement with the chemical analysis which showed that there was 2% excess gadolinium above the formula percentage.

The average value of the Weiss θ of 4.81° is a measure of the exchange constant J and will be referred to again in Section 4-5 when all the different ways of

estimating J will be compared.

The differences in values of θ along the crystallographic axes are due to the anisotropy energy between these directions, mainly attributable to the CEF interaction and we will return to them later when we are making quantitative estimates of the CEF. Suffice to say at the moment that they show the b-axis to be the most favoured direction of the three crystallographic axes, which will be borne out when we consider measurements below the ordering temperature.

No evidence was found for a Van Vleck temperature independent term in the susceptibility, which is not surprising since the first excited state is at 46,000^{o}K and therefore the energy denominator $(E_i - E_o)$ is very large.

The helium range measurements shown in Fig.2-5 appear at first glance to be the classic picture of a simple two sublattice antiferromagnet with the susceptibility parallel to the ordering direction going to zero as T approaches 0^{o}K and the two perpendicular directions staying constant.

The position of maximum slope in $\chi_{\parallel}$ corresponds

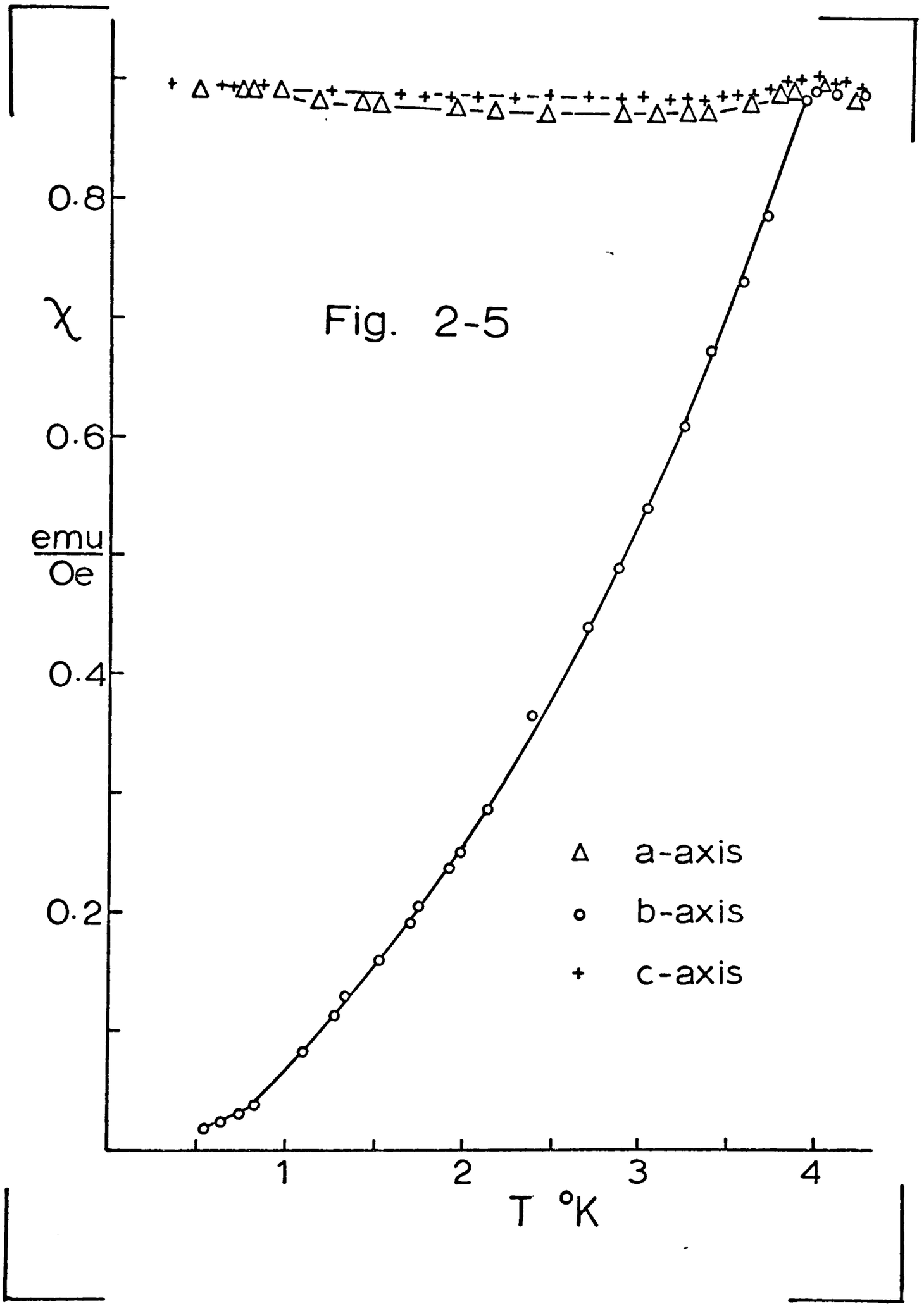


Fig. 2-5

very well to the value of the Néel temperature obtained from the specific heat measurements at $T_N = 3.87^{\circ}K$, and above this there is very little anisotropy.

Closer examination of the curves reveals two differences from the classical molecular field theory picture. The first is that the temperature dependence of $\chi_{\parallel}$ below T_N is somewhat different to that calculated from the MFT formula[28]:

$$\chi_{\parallel} = \frac{C\left(\frac{3S}{S+1}\right) B_s'(x)}{T - \theta\left(\frac{3S}{S+1}\right) B_s'(x)}$$

where $B_s'(x)$ is the differentiated Brillouin function with argument $x = g\beta SH/kT$.

This is shown as the dotted curve in Fig.2-6 together with the experimental curve. The reason for the difference between them is the neglect of anisotropy, so it is of interest to compare also with the theory of Eisele and Keffer[27] which takes account of anisotropy by using the spin flop field as a parameter. This field, H_c, will be fully dealt with in the next section and it suffices here to mention that for $GdAlO_3$ it equals 11.58kOe. The formula they obtain is:

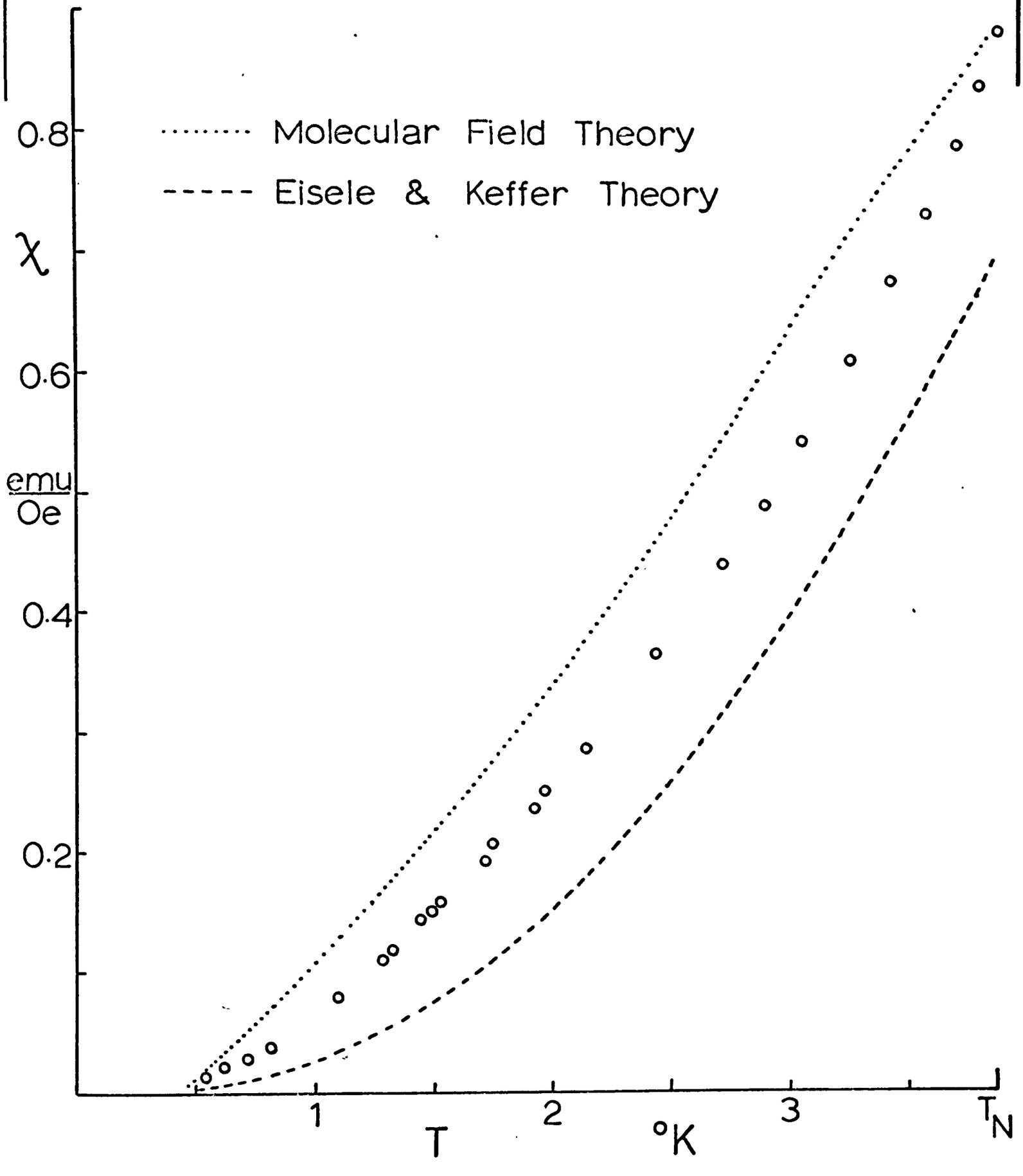

Molecular Field Theory
Eisele & Keffer Theory
0.8
χ
0.6
emu/Oe
0.4
0.2
1
2
3
T °K
T_N

Fig. 2-6

$$\chi_{\parallel} = \frac{Ng\beta}{2\pi^2}\left(\frac{z}{2}\right)^{1.5}\frac{H_c^2}{H_E^3}\sum_n K_2\left(n\frac{g\beta H_c}{kT}\right)$$

where H_E is the exchange field
and K_2 is a Hankel function.

This formula was evaluated by computer and the result is the broken curve in Fig.2-6. It can be seen that it reproduces the shape of the experimental curve well, while being about 20% too small in absolute magnitude.

The second difference from the classical picture can be seen in the enlarged plot of χ_a in Fig.2-7. We might guess that the fall in susceptibility between 1^{o} and $2^{o}K$ is almost certainly another manifestation of the CEF but will leave further discussion until our more complete treatment in Chapter 4.

2-5. Magnetic Moment Measurements.

The most striking feature of the moment experiments is the observation of a "spin-flop" when the magnetic field is applied parallel to the b-axis. This phenomenon, which is depicted in Fig.2-8, is expected in compounds in which the anisotropy energy is much smaller than the exchange energy. The reason for its occurrence

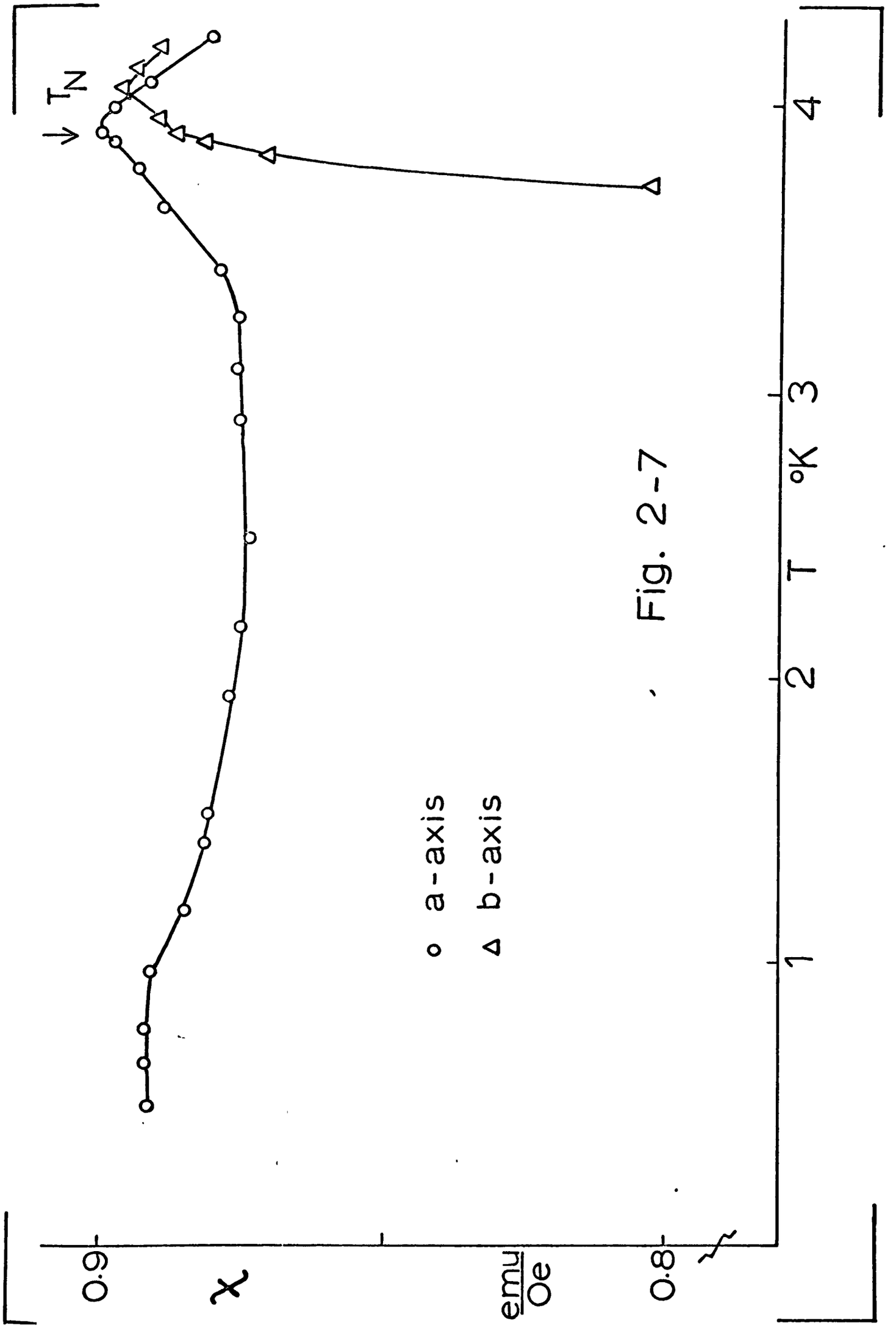


Fig. 2-7

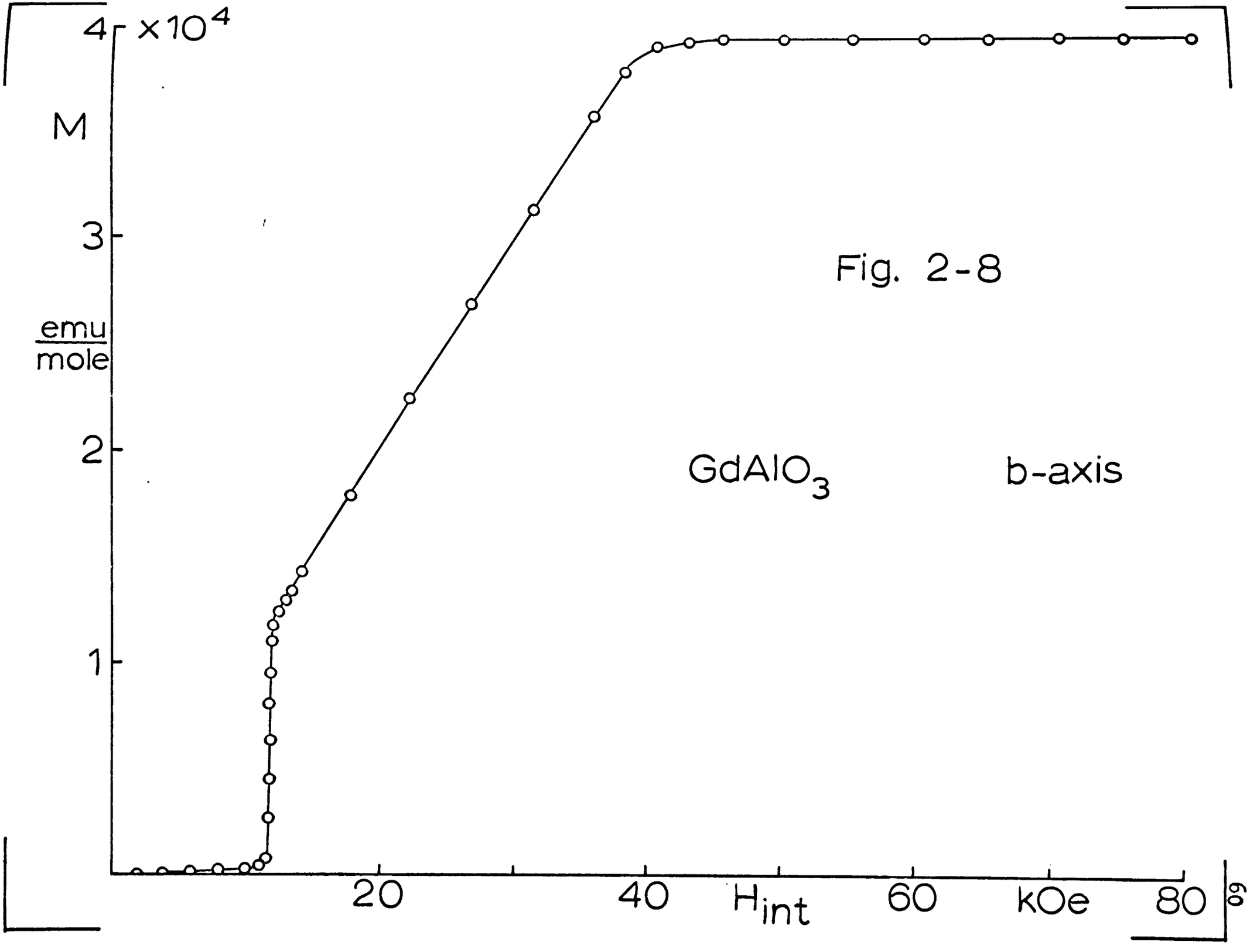


Fig. 2-8

can easily be seen as follows.

The energy of the crystal when the field is applied along the ordering direction may be written:

$$E_{\parallel} = -\tfrac{1}{2}\chi_{\parallel}H^2$$

Similarly, when the magnetic field is perpendicular to the ordering direction, we may write:

$$E_{\perp} = E_A - \tfrac{1}{2}\chi_{\perp}H^2$$

where E_A is the uniaxial anisotropy energy difference between the parallel and perpendicular directions.

For temperatures below T_N we have $\chi_{\perp} > \chi_{\parallel}$ and so $E_{\perp}$ decreases faster than $E_{\parallel}$ until for some field H_c, the two energies will be equal. Above this field, it becomes energetically more favourable for the spins to lie (almost) in the basal plane, thus gaining the anisotropy energy but reducing the external field energy, while still trying to retain antiparallel sublattice alignment and so avoid increasing the exchange energy.

The value of H_c obtained from Fig.2-8 is 11.58kOe which agrees well with the results of Hawkes[14], 11.4kOe, and Blazey and Rohrer[16], 11.5kOe. Above the flop the moment increases linearly with field until saturation is achieved at 39.5kOe. The value of the saturation moment, 39,500emu/mole, corresponds to 7.07

Bohr magnetons per ion.

As the temperature is increased, the curve becomes less sharp and the degeneration of the curve as a function of temperature is shown in Fig.2-9. One interesting feature of the curves is that they all pass through the point (12.0kOe, 11,200emu/mole) to within 1%, which is the experimental error in absolute accuracy between different experiments. Even the curves taken at 3.92°K and 4.02°K, above the Neel temperature, passed through this "magic point", although a similar run at 4.22°K did not.

The area between the moment curve and the straight line between the origin and the magic point is an energy and is in fact a measure of the anisotropy energy introduced by the magnetic ordering. The temperature dependence of this area is shown in Fig.2-10 and is plotted as a fraction of the maximum area of the triangle between the origin and the magic point. We shall return in the next chapter to show how we may make further use of this anisotropy energy and the magic point.

Joenk[29] has derived a theoretical expression for the magnetic moment in the parallel direction as a function of applied field and temperature. His formula:

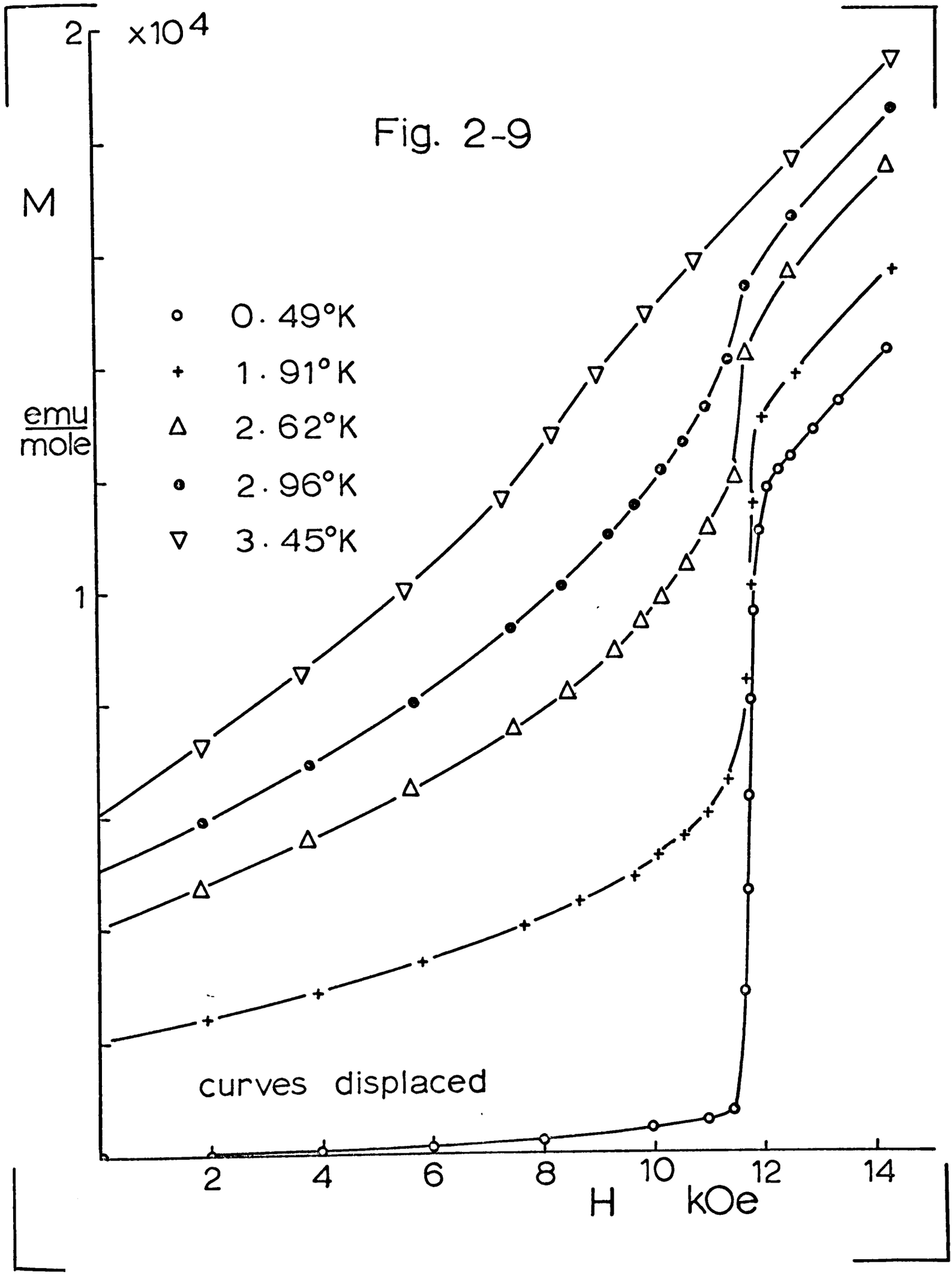

2
×10⁴
M
emu
mole
1
0.49°K
1.91°K
2.62°K
2.96°K
3.45°K
curves displaced
2
4
6
8
10
12
14
H kOe

Fig. 2-9

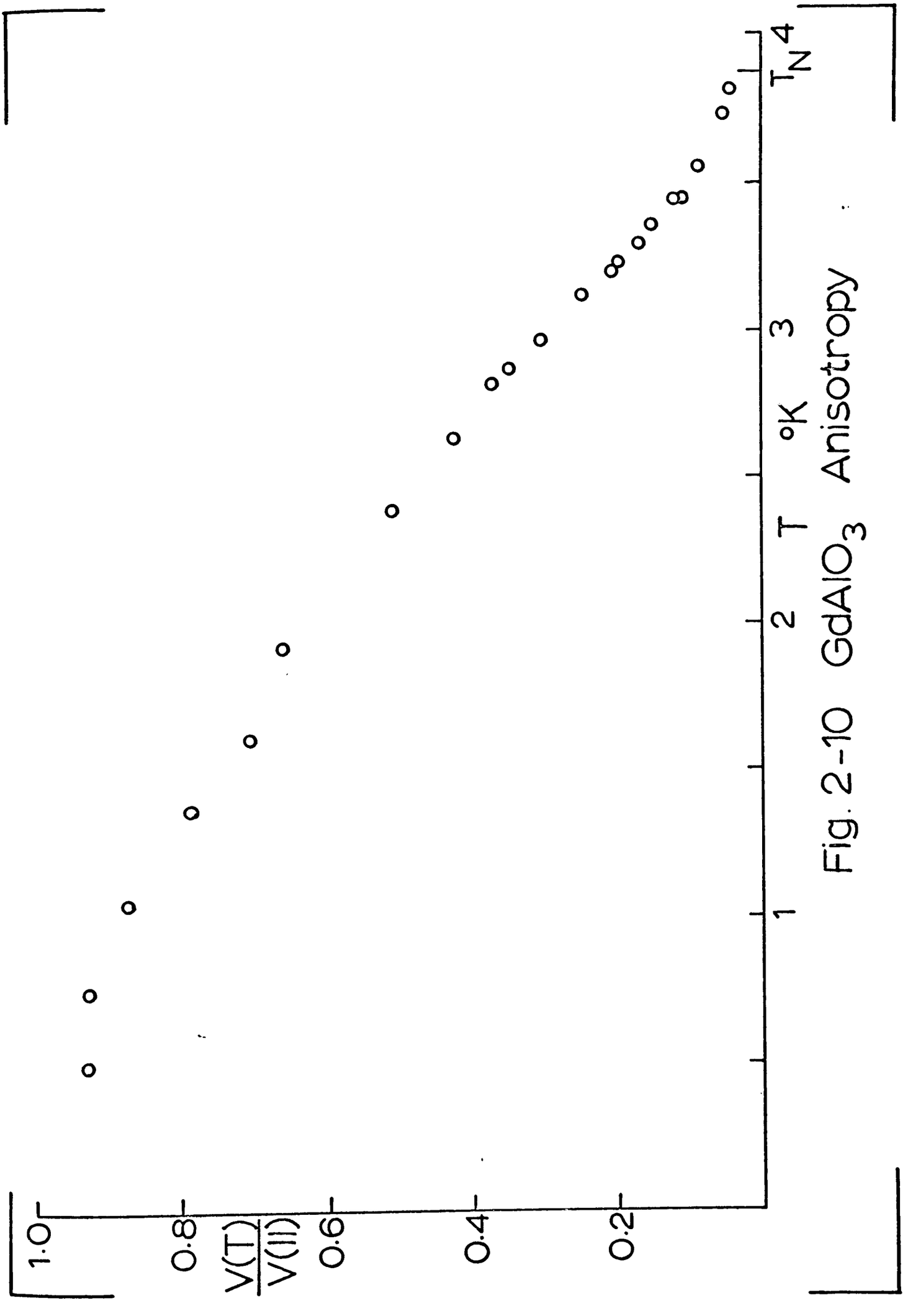


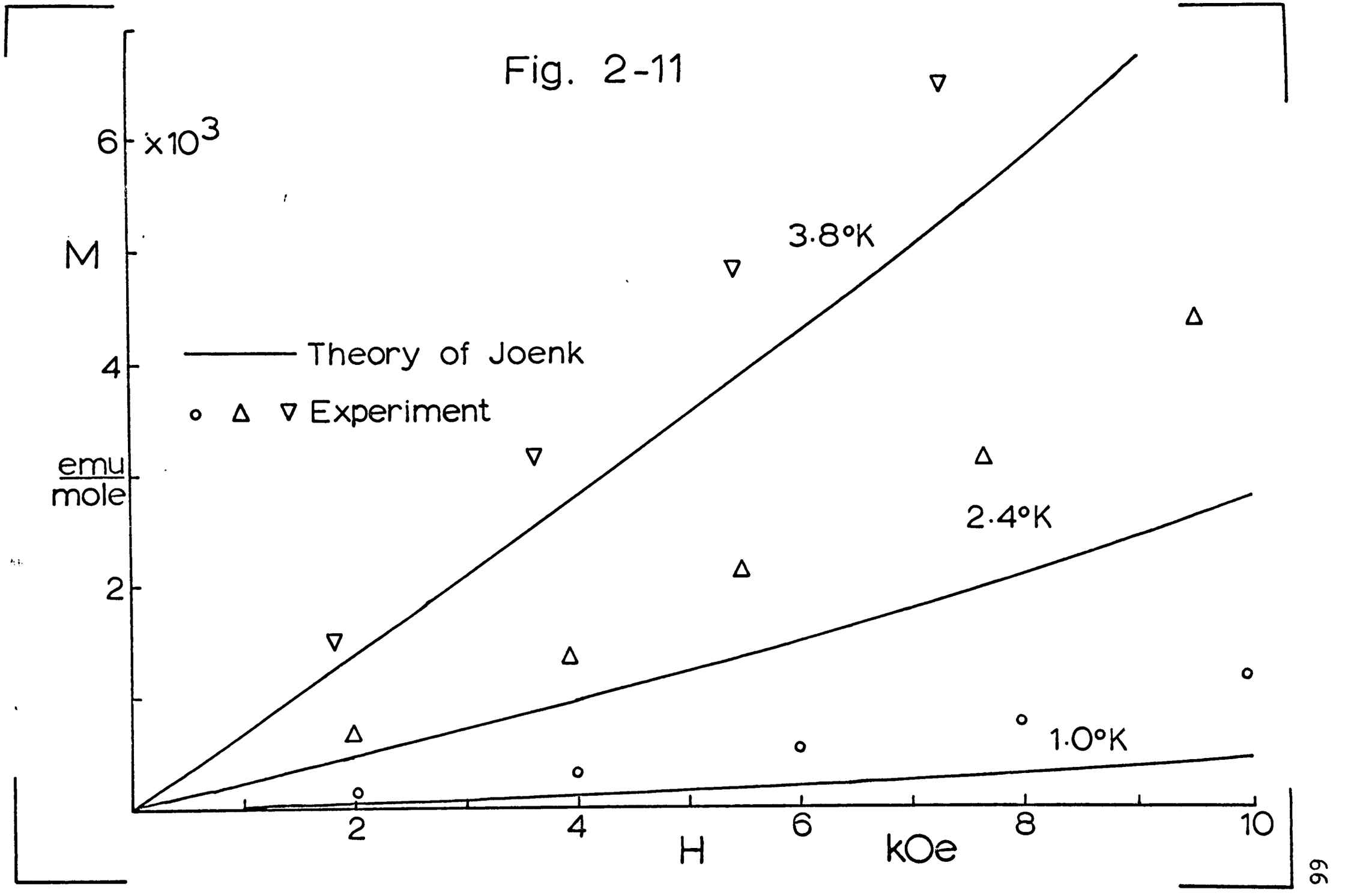
Fig. 2-10 $GdAlO_3$ Anisotropy

$$M(H,T) = \frac{1}{8\pi^2}\left(\frac{z}{2}\right)^{1.5} Ng\beta\left(\frac{H_c}{H_E}\right)^3 \sum_n \sinh\left(n\frac{g\beta H}{kT}\right)\left[K_3\left(n\frac{g\beta H_c}{kT}\right) - K_1\left(n\frac{g\beta H_c}{kT}\right)\right]$$

in terms of the Hankel functions K_1 and K_3 has been evaluated by computer and the results for three different temperatures are shown in Fig.2-11 together with the experimental curves appropriate to these temperatures.

The theoretical curves underestimate the moment over the whole temperature range, but are in fact very good fits to the experimental points taken at a temperature $0.4^{o}K$ lower. This temperature difference remains constant over the whole measured temperature range from $0.5^{o}K$ to T_N but we have been unable to put forward any reason why this should happen. A similar effect can be seen in the analogous susceptibility curve of Eisele and Keffer shown in Fig.2-6.

Measurements of the magnetic moment at $0.5^{o}K$ along the other two orthorhombic axes are shown in Fig.2-12. Both can be seen to rise linearly with field, reaching saturation at 44.4kOe along the c-axis and 45.6kOe along the a-axis. The saturation moments of 39,500 and 39,400 emu/mole respectively show that the g-tensor is indeed isotropic and all the results are within 1% of 7 Bohr magnetons per ion.


Fig. 2-11
6
x10^3
M
4
emu
mole
2
Theory of Joenk
Experiment
3.8°K
2.4°K
1.0°K
2
4
6
8
10
H
kOe

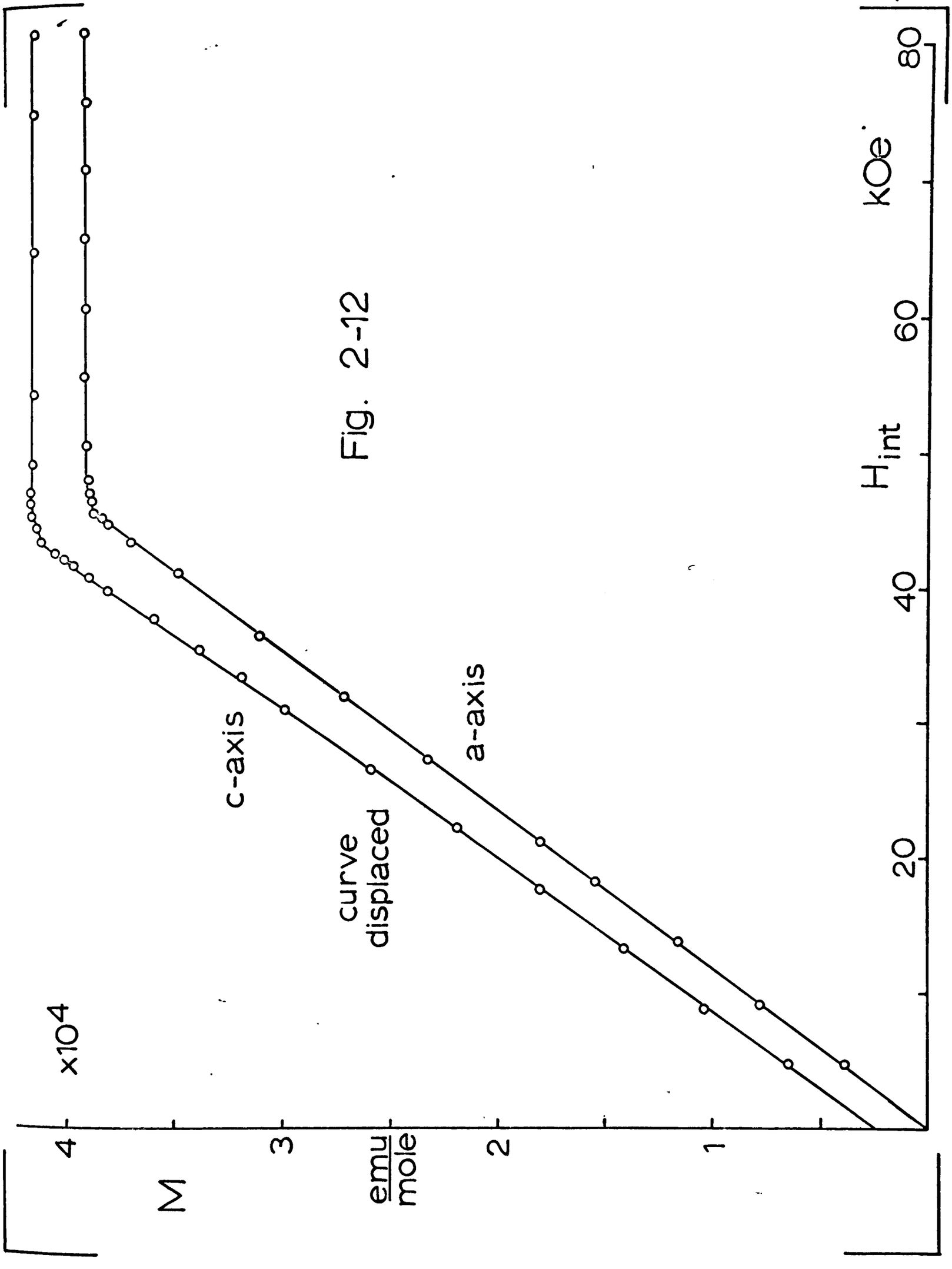

M
x10⁴
emu/mole
4
3
2
1
c-axis
curve displaced
a-axis
20
40
60
80
H_int
kOe

Fig. 2-12

From these measurements we can obtain an important piece of information. The simple theory of the spin flop given at the start of this section showed that above H_c the spins flop to the basal plane. However in $GdAlO_3$ the symmetry of the anisotropy energy is orthorhombic and not uniaxial, so that there will be a preferred direction for the spins to flop towards.

According to molecular field theory the value of the saturation field along the parallel direction is $2H_E - H_A$, and along a perpendicular direction is $2H_E + H_A$, where H_E is the exchange field and H_A the anisotropy field.

From these simple formulae we can get the values of the anisotropy fields from the b-axis to the other two axes as:

$$H_A^{bc} = 2.45\text{kOe}$$

$$H_A^{ba} = 3.05\text{kOe}$$

This implies that since the c-axis is a direction of smaller anisotropy than the a-axis, then the spins flop in the b-c plane. This is in agreement with the conclusions of Hawkes[14] from optical measurements and could also have been deduced from the hydrogen range susceptibility measurements in the preceding section.

There the values of the Weiss θ can be seen to again be in the order $\theta_b < \theta_c < \theta_a$ indicating that the c-axis is the second most favourable axis, but we shall leave a quantitative comparison between these results until our fuller discussion of crystal field effects.

As can be seen in Fig.2-12, the approach to saturation along the a-axis is perfectly linear with field and has a very sharp knee region of less than 2kOe. However the moment along the c-axis is only linear up to 33kOe, at which field it deviates slightly upwards, the bulge having its maximum deviation at about 42.5kOe.

With increase in temperature this bulge increases in size and moves to lower fields. The position of the bulge maximum is difficult to estimate, but its motion with temperature is not linear, appearing to follow a curve more like the sublattice magnetization. Extrapolated to $T = 0^{\circ}K$, the maximum appears to be at the knee of the curve, 44.4kOe, as near as can be estimated. Above the Neel temperature, the bulge disappears completely. An interpretation of the cause of this bulge will be given in Chapter 4 when we are considering the four sublattice model for $GdAlO_3$.

2-6. Summary.

After a brief description of the two major interactions in $GdAlO_3$, Heisenberg nearest neighbour exchange and the crystal field interaction, the results, conflicting at times, of other workers using optical, resonance and high field moment techniques were described.

The results of the specific heat measurement showed a lambda anomaly at 3.870°K and a Shottky anomaly at about 1°K. Part of the susceptibility and magnetic moment measurements could be explained on the basis of a simple two sublattice antiferromagnet ordering parallel to the b-axis, and deductions about the orthorhombic symmetry anisotropy from both sets of measurements showed that the spins flop in the b-c plane.

Several details were left to be explained later in a full description of the crystal field effects and the use of a four sublattice picture. These were:

(i) the disagreement between the distribution of energy and entropy above and below T_N with the model of a Heisenberg simple cubic antiferromagnet,

(ii) a comparison between the anisotropy as estimated by moment and susceptibility measurements,

(iii) estimates of the value of the exchange constant J,

(iv) the reason for the jump in χ_a between 1 and $2^{o}K$,

(v) the reason for the temperature dependent bulge in the magnetic moment along the c-axis.

CHAPTER THREE

GADOLINIUM ALUMINATE

SUBLATTICE MAGNETIZATION and the PHASE DIAGRAM.

3-1. Introduction.

The simplest model for understanding the phenomenon of cooperative magnetism is the molecular field theory (MFT) due originally to Weiss[2], in which each magnetic ion is considered to be in an effective field made up of its interactions with all its neighbours. In other words, if we start with the Heisenberg Hamiltonian

$$\mathcal{H}_{ij} = -2 \Sigma J_{ij} \underline{S}_i \cdot \underline{S}_j$$

where the summation is over pairs, then we can write it in the form

$$\mathcal{H}_{ij} = -g\beta \underline{H}_E \cdot \underline{S}_i$$

where we have now introduced an effective field $\underline{H}_E$ such that

$$\underline{H}_E = \frac{2}{g\beta} \sum_j J_{ij} \underline{S}_j .$$

Although this model enables us to reproduce qualitatively many of the phenomena associated with magnetic ordering, e.g. a sharp peak in the specific heat,

a spontaneous magnetization and a divergence in χ for $J_{ij} > 0$, or a decreasing $\chi_{\parallel}$ and a constant $\chi_{\perp}$ for $J_{ij} < 0$, its quantitative agreement with experiment is not good.

In some cases it predicts an incorrect mathematical form for the approach to the critical points $T = 0$ or $T = T_N$, e.g. a linear increase in the specific heat for $T \lesssim T_N$, and of course by neglecting short range order it cannot deal with phenomena just above the ordering temperature.

However once we have obtained the formulae for the various measurable quantities in terms of the interaction parameters it is now possible to use MFT in a different way. Taking two such formulae, we can eliminate the explicit dependence on the interaction between them, arriving at a formula directly connecting two measured quantities.

Although the original formulae from first principles may have given quantitatively poor results, these new formulae are much more accurate[30,31]. The reason is that by removing the explicit dependence on the form of the original interaction, we have effectively allowed the inclusion of any other interaction which has a similar effect on our two experimentally measured

quantities.

This is equivalent to stating that the internal consistency of the MFT is very much better than its accuracy in ab initio calculations. This fact is important to us here because of the crystal field interaction which, even if included as an additional term in the Hamiltonian, still does not give quantitatively correct answers - although certainly being an improvement.

The internal consistency allows us to obtain one experimental quantity which we are not able to measure - the sublattice magnetization. As an example of its accuracy, the sublattice magnetization will be worked out in several different ways, including use of the "magic point" in the moment curves mentioned in Section 2-5.

As an even more stringent test we will use two of these derived formulae to work from the parallel susceptibility to the specific heat results via the sublattice magnetization.

In Section 3-3 the moment measurements will be used to derive the magnetic phase diagram in the H-T plane between the paramagnetic, antiferromagnetic and spin-flop phases.

3-2. Fisher's Relation.

From a study of the correlation functions between the spins on different ions near the Néel temperature, Fisher[32] derived a relation, in a manner analogous to that described previously for MFT, between the specific heat and susceptibility. This formula, or Fisher's relation as it has become known, is:

$$\frac{C}{R} = A \frac{\partial}{\partial T}(\chi_{\parallel} T)$$

where A is a slowly varying function of temperature.

The unusual feature of the relation is that it is expected to remain smooth as the temperature passes <u>through</u> the ordering transition - a region where most functions have at least a discontinuous change of gradient.

For the purposes of testing this relation it was found more convenient to calculate as:

$$\chi_{\parallel} T = \frac{1}{A} \int \frac{C}{R} \, dT$$

The resulting curve is shown in Fig.3-1, where the origin of the energy scale on the y-axis has been chosen arbitrarily. It can be seen that there is only a very small bump at the ordering temperature, and then the curve settles down on the same line as below T_N.

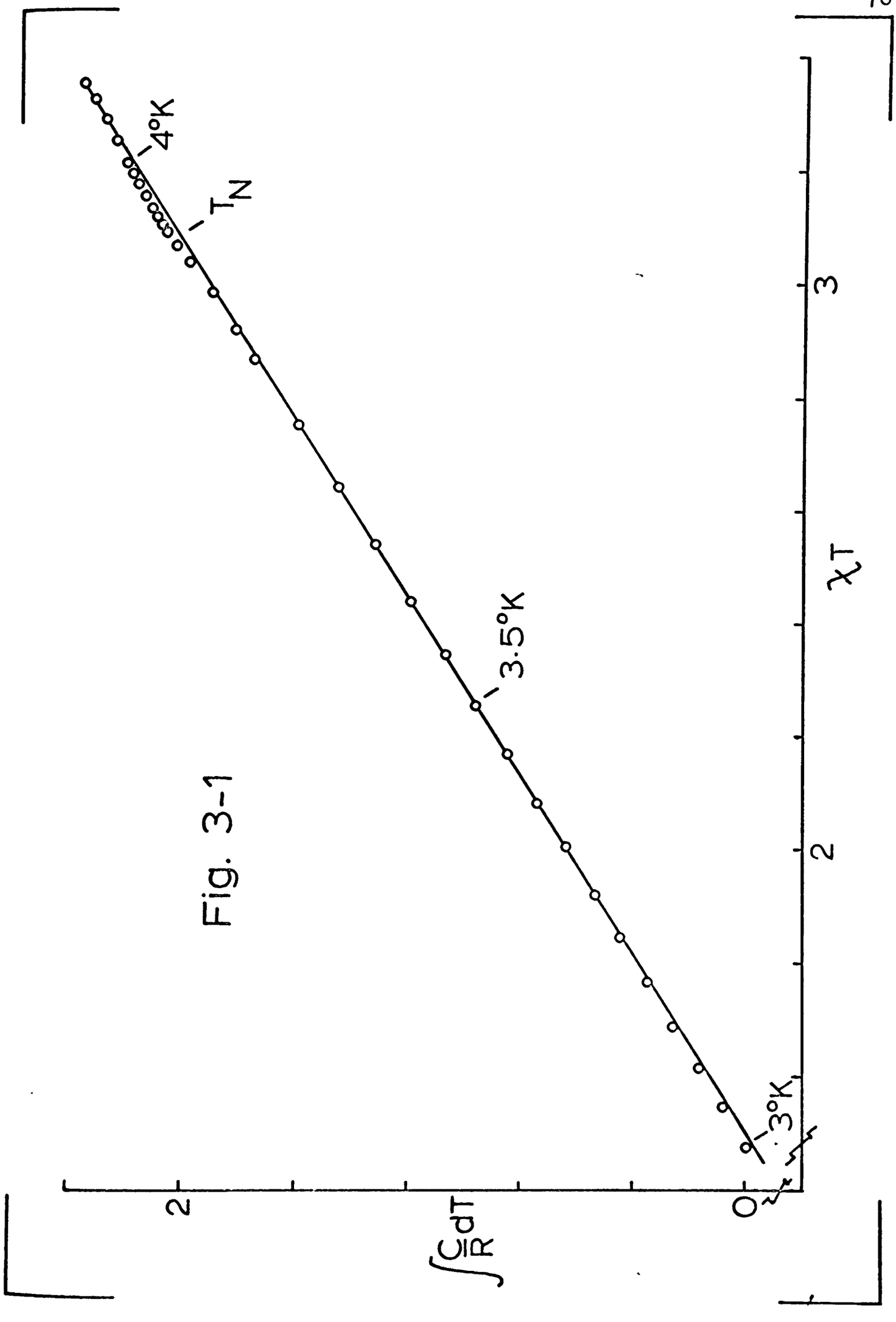


Fig. 3-1

From the slope of the line we obtain the value of A as:

$$A = 1.09 \times 10^8 \ Oe^2/^oK.$$

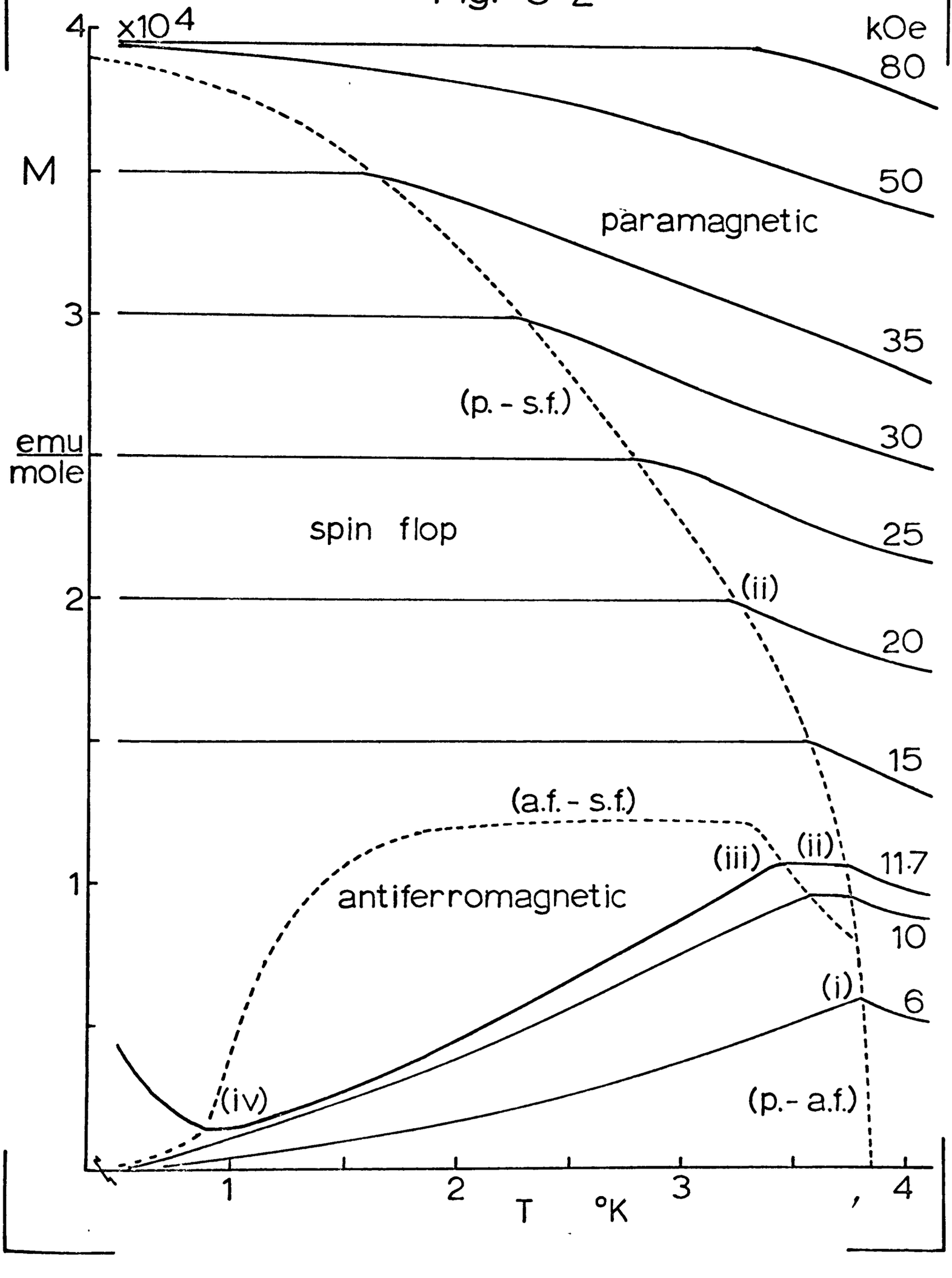
3-3. The Magnetic Phase Diagram.

There are several ways in which one can obtain the division of the H - T plane into the paramagnetic, antiferromagnetic and spin-flop phases, probably the easiest being nuclear magnetic resonance. It is however, reasonably straight forward to derive it from moment measurements along the parallel direction by a method first used by Gijsman et al[33].

Their technique is to replot the moment measurements as isoerstedic lines on an M - T diagram, a technique which requires measuring the magnetic moment at many temperatures below T_N. A plot of this kind is shown in Fig.3-2 where only a few representative isoerstedic lines have been drawn.

The boundary of the paramagnetic region is defined by the point where the isoerstedic line stops rising with decreasing temperature. This applies both to the paramagnetic - antiferromagnetic (p.-a.f.), point (i) in Fig.3-2, and the paramagnetic - spin-flop (p.-s.f.) boundaries, point (ii). If the isoerstedic line has a

Fig. 3-2

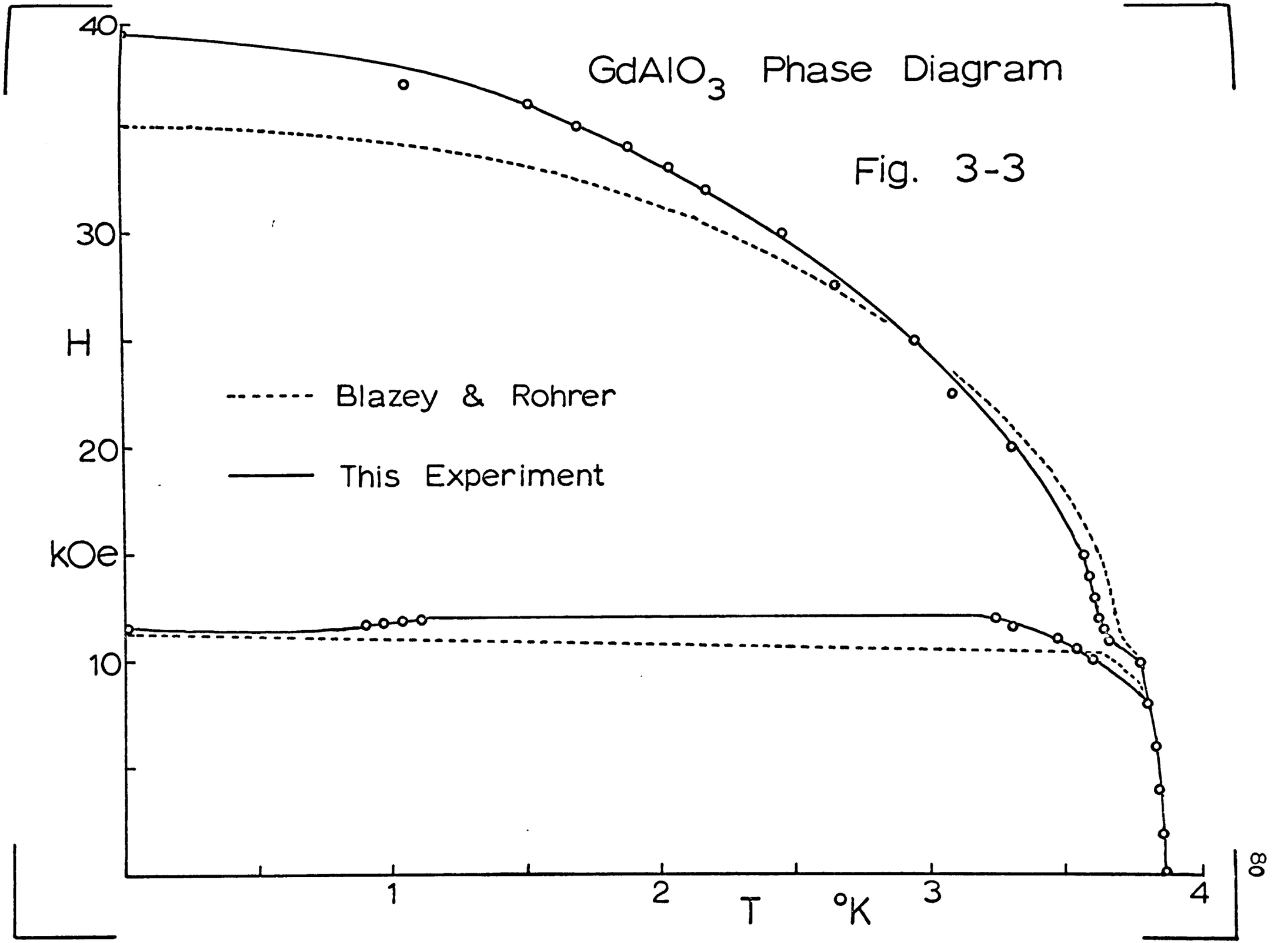

4
x10 4
kOe
80
M
50
paramagnetic
3
35
(p. - s.f.)
30
emu
mole
spin flop
25
2
(ii)
20
15
(a.f. - s.f.)
(iii)
(ii)
11.7
1
antiferromagnetic
10
(i)
6
(iv)
(p.- a.f.)
1
2
3
4
T °K

horizontal part followed by a decrease with decreasing temperature as at point (iii), the point where the decrease starts in the a.f.-s.f. boundary.

Using these interpretations, the phase diagram has been deduced as in Fig.3-3. An unusual effect was observed around 1°K where several of the isoerstedic lines started increasing again with decreasing temperature as at point (iv) in Fig.3-2. This was interpreted as being a drop in the p.-s.f. boundary to a lower field value as shown in Fig.3-3.

The reason for the drop is probably that in this temperature range the second lowest energy level ($S_z = +5/2$) is being depopulated and the crystal is rapidly approaching the state of completely aligned sublattice magnetizations (except for the zero point deviation). In this state we may expect that the sublattices will turn more readily to the spin-flop state, because there is no way they can partly achieve this state by spin deviations as at higher temperatures.

It is unfortunate that in using this method of obtaining the phase diagram,. points can only be obtained when a phase boundary crosses an isoerstedic line. This means that there are no points on the p.-s.f. boundary


GdAlO3 Phase Diagram
Fig. 3-3
40
30
20
10
H
kOe
Blazey & Rohrer
This Experiment
1
2
3
4
T °K

over a region of 2^{o} where the phase boundary stays within 0.1kOe of 12kOe.

The broken curve on Fig.3-3 is the phase diagram obtained by Blazey and Rohrer[16]. The agreement at low values of field is quite good, but the curves diverge at high field as the relaxation time begins to significantly affect their pulsed field measurements. For small values of field, their results may be more accurate than ours, since they directly measure $\partial M/\partial H$ at a given temperature, rather than having to interpolate $\partial M/\partial H$ between two measured temperatures as in our method.

However there does seem to be a significant difference in the a.f.-s.f. boundary, where their curve has the unusual property of dropping with increasing temperature. Simple theory predicts that the spin-flop field should rise with increasing temperature[9] as:

$$\frac{H_c(T)}{H_c(0)} = \frac{1}{(1 - \chi_{\parallel}/\chi_{\perp})^{\frac{1}{2}}}$$

since there is less energy to be gained by flopping to the basal plane as $\chi_{\parallel}$ approaches $\chi_{\perp}$. Previously published phase diagrams[35] all show H_c increasing with temperature although not nearly as sharply as predicted by the above formula.

It is interesting that both phase diagrams in Fig.3-3 show a small pocket of spin flop phase extending down into the antiferromagnetic region. The difference between the sizes of this pocket is not regarded as significant, because the criterion for choosing the boundary position is somewhat open to individual interpretation. The error is not correctly represented by the scatter of the points as this is only the error in being consistent to one interpretation.

3-4. Sublattice Magnetization from the Susceptibility.

As already mentioned in Section 2-4 the molecular field theory formula for the parallel susceptibility is given by:

$$\chi_{\parallel} = \frac{C\left(\frac{3S}{S+1}\right) B_s'(x)}{T - \theta\left(\frac{3S}{S+1}\right) B_s'(x)} \qquad \ldots(3\text{-}1)$$

where $B_s'(x)$ is the differentiated Brillouin function with argument $x = g\beta HS/kT$.

In the same theory the sublattice magnetization is given by:

$$\mathcal{M} = \tfrac{1}{2}Ng\beta S B_s(x) \qquad \ldots(3\text{-}2)$$

It was pointed out by Hornreich and Shtrikman[31] that by effectively eliminating x between these two equations one could obtain the infrequently measured sublattice magnetization from the much more common susceptibility measurements. The simplest way of carrying out this elimination is numerically, using tables of $B_s(x)$ and $B_s'(x)$ as found for example in Appendix 1 of Smart[36].

The only essential feature of the calculation is that the value of $\chi_{\parallel}(T_N)$ must equal that predicted by MFT or the derived sublattice magnetization will not go to zero at T_N. Fortunately our value of $\chi_{\parallel}(T_N) = 0.890$ was sufficiently close to that predicted by MFT (0.887) to avoid the necessity of using some kind of scaling factor normalization.

The resulting curve obtained, using our experimentally measured mean value for $\theta = -4.81\,^{\circ}K$, is shown as the continuous line in Fig.3-4. The scales used are in the reduced units

$$m = \frac{\mathcal{M}}{\frac{1}{2}Ng\beta S}$$

$$\tau = \frac{T}{T_N}$$

Since we had no experimentally measured values of the sublattice magnetization for comparison it was

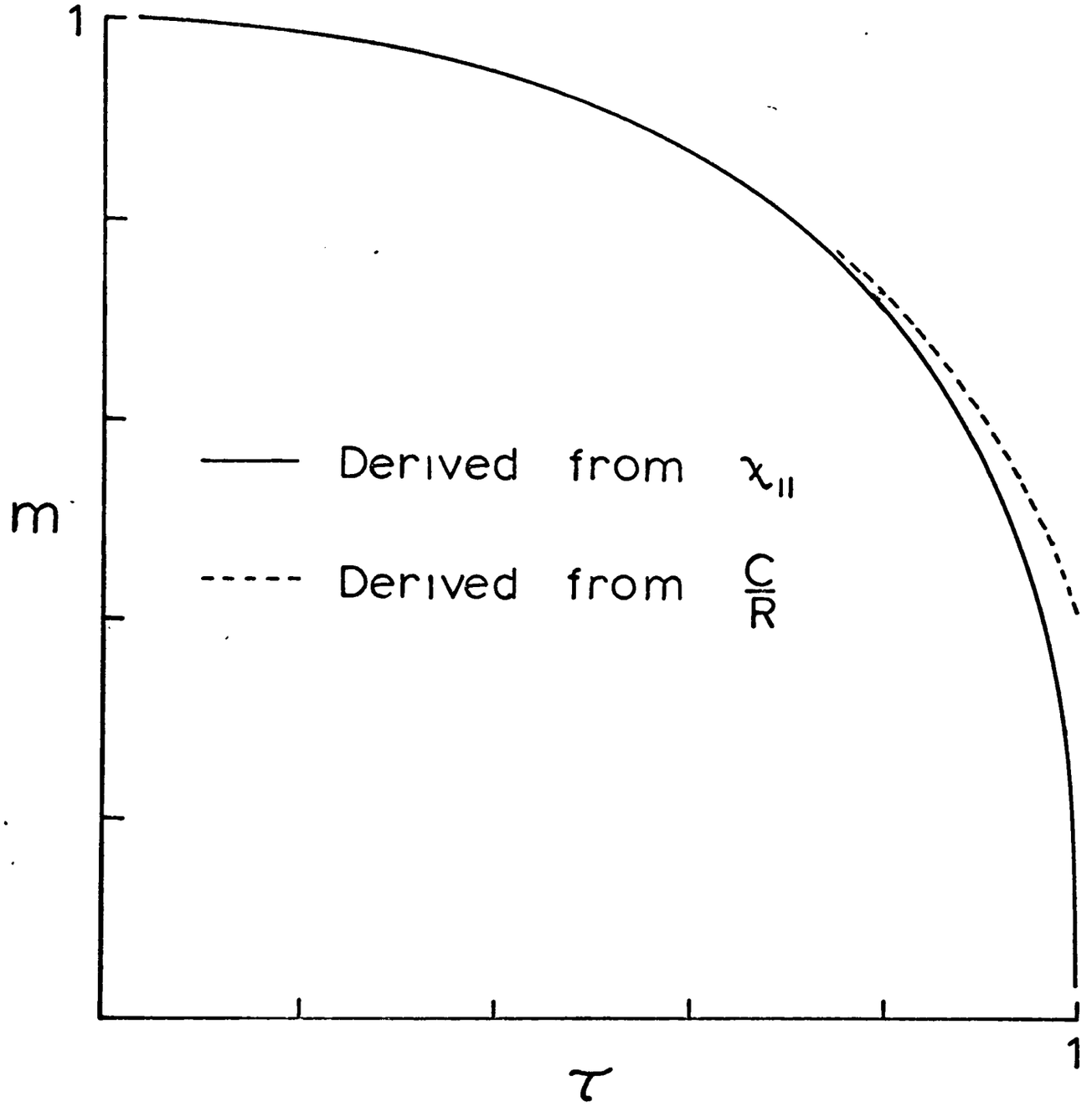


Fig. 3-4

decided to carry the calculation one stage further using the MFT relation between the sublattice magnetization and the specific heat

$$C = 2\gamma \frac{\partial \mathcal{M}^2}{\partial T}$$

where the molecular field constant γ is related to the exchange constant J by:

$$\gamma = \frac{2zJ}{Ng^2\beta^2}$$

If we for a moment anticipate and use the value $J/k = -0.067^{\circ}$ obtained in the next chapter, we get, in terms of the reduced quantities:

$$\frac{C}{R} = -1.29 \frac{\partial m^2}{\partial \tau} \qquad \ldots(3\text{-}3)$$

This curve is plotted in Fig.3-5 together with the experimentally measured specific heat points. The agreement is seen to be surprisingly good and is in fact perfect up to $\tau = 0.6$.

Considering the severity of the test, when we have used two relationships between measured quantities, one of which involved the differentiation of the second power, Fig.3-5 is a striking proof of the internal consistency of the molecular field theory.

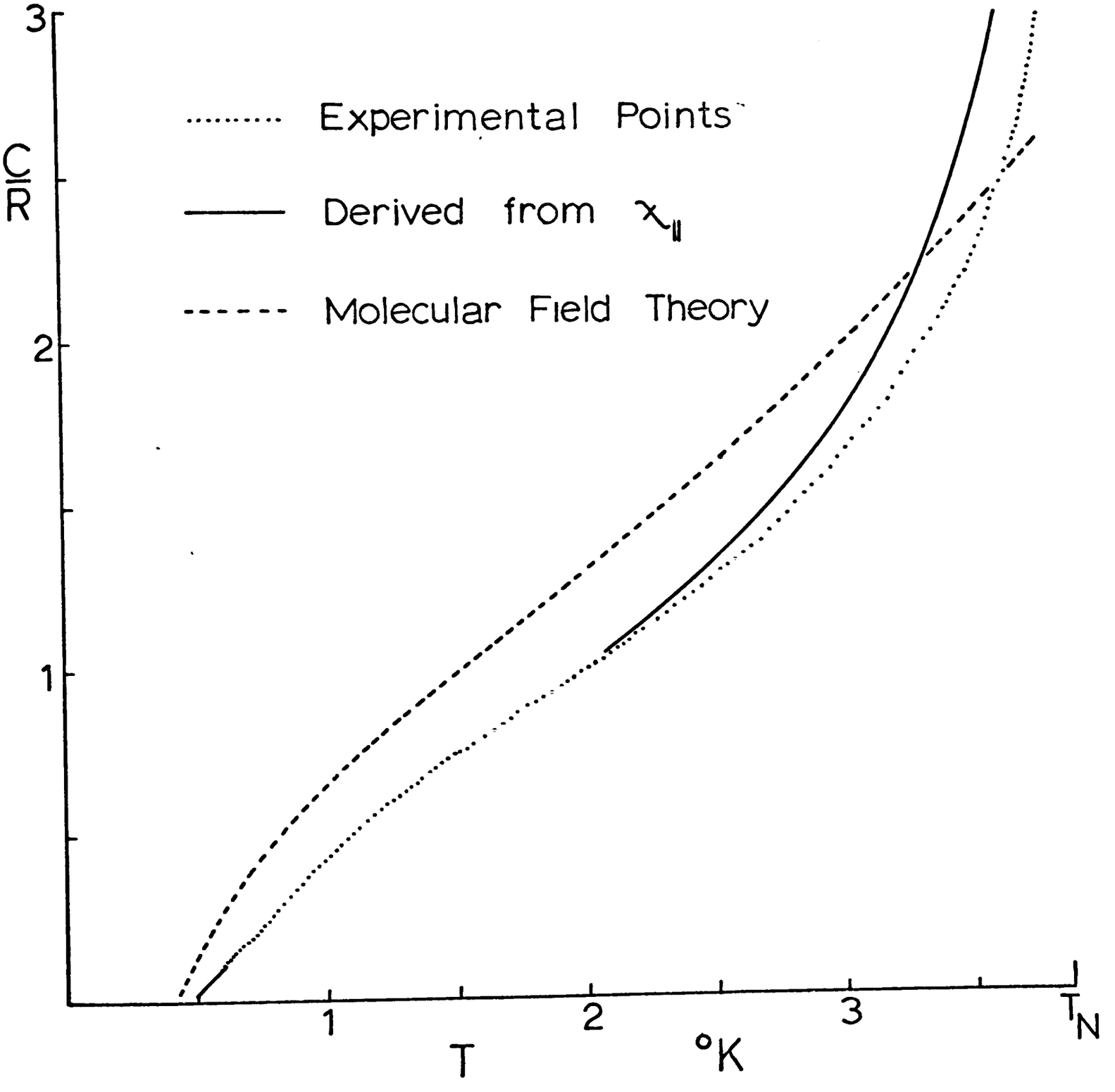

3
2
1
C/R
Experimental Points
Derived from $\chi_{\parallel}$
Molecular Field Theory
1
2
3
T_N
T °K

Fig. 3-5

3-5. Sublattice Magnetization from the Specific Heat.

Since the specific heat curve derived in the previous section did not accurately follow the experimental points in the region around T_N it was considered worth while to reverse the procedure in Eq.3-3 to obtain some estimate of how much error may have been introduced into the sublattice magnetization curve.

The resulting curve from this formula,

$$m(\tau) = \left[1 - \frac{1}{1.29T_N}\int_0^{\tau}\frac{C}{R}\,d\tau\right]^{\frac{1}{2}}$$

is shown as the broken curve in Fig.3-4. As expected from the consistency of the previous results the difference between the curves is not very great, although there is a large possible error for $\tau>0.95$ where the curve is dropping very steeply.

3-6. Sublattice Magnetization by Molecular Field Theory.

The simple MFT formula for sublattice magnetization, Eq.3-2, does not take any account of anisotropy effects. It is derived by assuming an internal field, H_E, for which we may write down the partition function:

$$Z = \sum_{S_z=-S}^{S} \exp(g\beta S_z H_E/kT)$$

From this is follows directly that:

$$\frac{\langle S_z \rangle}{S} = m = \frac{1}{Z} \sum_{S_z} S_z \exp(g\beta S_z H_E / kT) \quad \ldots(3\text{-}4)$$

Substituting the MFT approximation for H_E,

$$g\beta H_E = 2zJ\langle S_z \rangle$$

turns Eq.3-4 into a self consistent equation which is readily soluble numerically.

It is easy to introduce an anisotropy term into this calculation by adding an additional term into the partition function. We will choose the simplest type of anisotropy - a uniaxial $D\left[S_z^2 - 1/3\ S(S+1)\right]$ term - a decision which will be justified in the next chapter.

Our new partition function becomes:

$$Z_A = \sum_{S_z} \exp\left[\left\{2zJS_z\ S_z - D\left[S_z^2 - 1/3\ S(S+1)\right]\right\}/kT\right] \quad \ldots(3\text{-}5)$$

and the formula for the reduced sublattice magnetization

$$\frac{\langle S_z \rangle}{S} = \frac{1}{Z_A} \sum_{S_z} S_z \exp\left[\left\{2zJS_z\langle S_z \rangle - D\left[S_z^2 - 1/3\ S(S+1)\right]\right\}/kT\right]$$

This equation was solved by computer for different values of D both positive and negative. The results for $D/k = -0.05^{\circ}K$ and $-0.10^{\circ}K$ as well as for $D = 0$ are shown in Fig.3-6. It can be seen, in comparison with the curve derived from $\chi_{\parallel}$, that although the increasingly

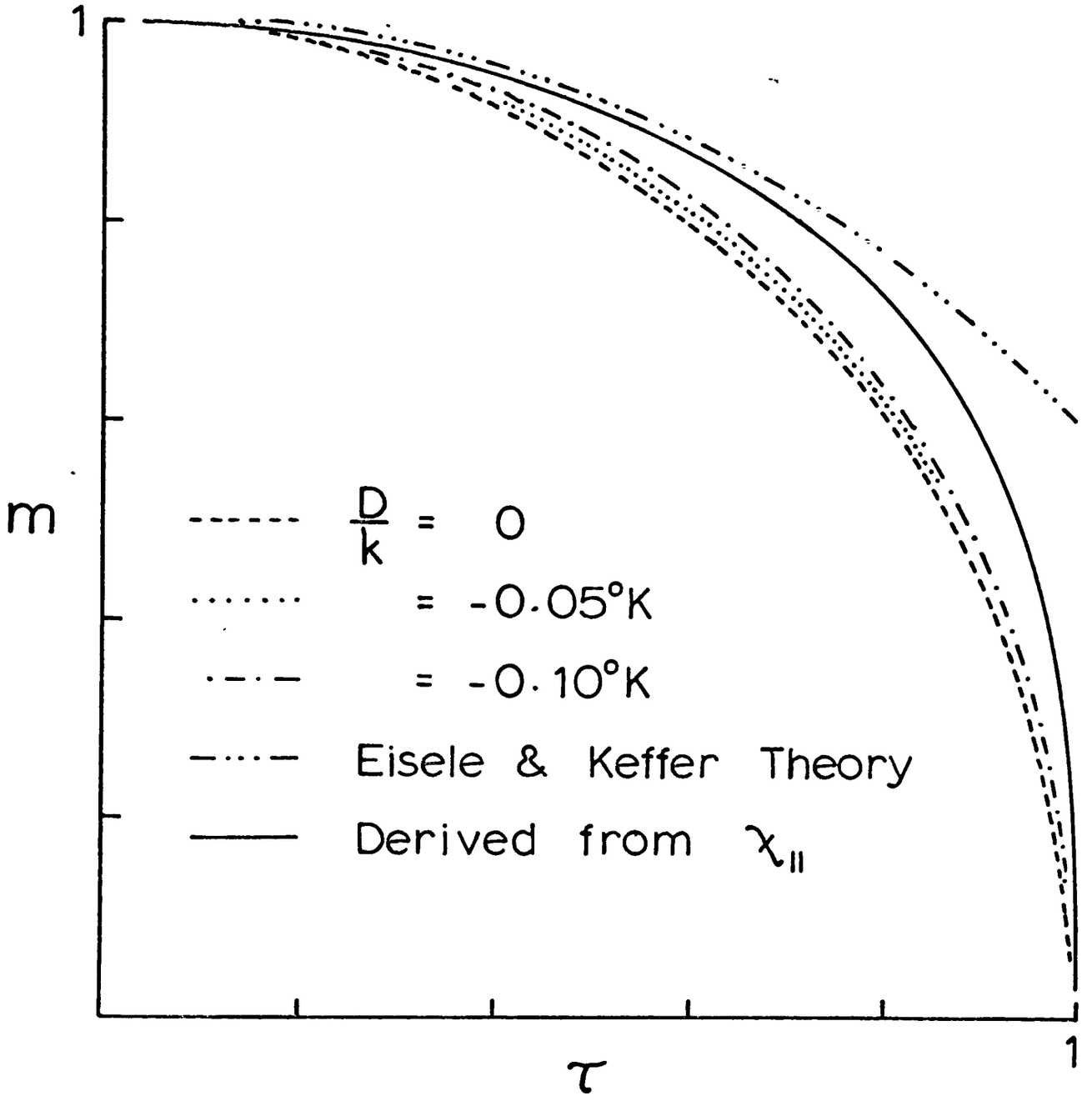

1
m
$\frac{D}{k}$ = 0
= -0.05°K
= -0.10°K
Eisele & Keffer Theory
Derived from χ_{II}
1
τ

Fig. 3-6

large negative values of D move the curve in the right direction, the rate is slow, and a much larger value of D would be needed to make the curves agree. In the next chapter we shall show that the value $D/k = -0.05^{\circ}K$ should be the most appropriate.

The specific heat can be obtained from these results using Eq.3-3 and is shown as the broken curve in Fig.3-5. As can be seen the curve does exhibit a bump at the right temperature but the absolute magnitude of the result is not correct.

This illustrates well how MFT very easily produces qualitatively correct results, but in calculations from values of the interaction parameters will not give quantitative results even when, as in this case, very nearly the correct values of the two major interactions are included.

The theory of Eisele and Keffer[27], which has been mentioned before, also derives a formula for the sublattice magnetization using the exchange constant, J, and the spin flop temperature, T_{AE}, as parameters. Their formula is:

$$m = 1 - \frac{1}{6S}\left(\frac{z}{2}\right)^{1.5}\left(\frac{k}{2zSJ}\right)^{2}\left[\frac{6}{\pi^{2}}\, T_{AE}T \sum \frac{1}{n} K_{1}\left(\frac{nT_{AE}}{T}\right)\right]$$

This formula has been evaluated by computer and the result is also shown in Fig.3-6. Since the formula is derived from spin wave theory it can only be expected to be valid at low temperatures, where we can see that it slightly overestimates the effect of the anisotropy.

3-7. Sublattice Magnetization from the Anisotropy Energy.

It has been shown by Zener[37] that the anisotropy energy in ferromagnets is simply related to the spontaneous magnetization when this is due to short range interactions only.

His calculations have been extended by Pincus[38] to antiferromagnets and the resultant formula may be given in the form:

$$\frac{V(T)}{V(\parallel)} = \left[\frac{m(T)}{m(\parallel)}\right]^{\frac{1}{2}n(n+1)}$$

or

$$\frac{V(T)}{V(0)} = \left[\frac{m(T)}{m(0)}\right]^{\frac{1}{2}n(n+1)}$$

where V(T) is the anisotropy energy at temperature T, and V(0) and V(∥) refer to its values at T = 0 and in the completely aligned Néel state respectively.

The index n is the order of the principal surface harmonic of the anisotropy energy which for the

distorted perovskite structure Pbnm is 2[17]. The formula is only valid for low temperatures.

A graph of V(T) for $GdAlO_3$ has already been given in Fig.2-10 and the question now arises as to what we should take for V(0) or V(∥). The triangular area in the moment curve (Fig.3-7, broken lines) should correspond to V(∥) provided $\chi_{\parallel}$ is zero at T = 0. This seems to be true experimentally and so we can use the former of Pincus' formulae.

The results are shown in Fig.3-8 and it can be seen that the low temperature limit is not unity but 0.977. This difference seems to be a direct measurement of the spin deviation although one word of caution should be mentioned about the experimental accuracy. The measurement will be extremely sensitive to any misalignment of the crystal although this was believed to be better than 1^{o}.

A table of theoretical estimates for the spin deviation is given by Keffer[39]. The spin wave theory prediction for a simple cubic lattice is:

$$\delta m = \frac{0.078}{S} = 0.022$$

A linked cluster calculation carried out by Davis[40] for the simple cubic lattice gives the value

Fig. 3-7

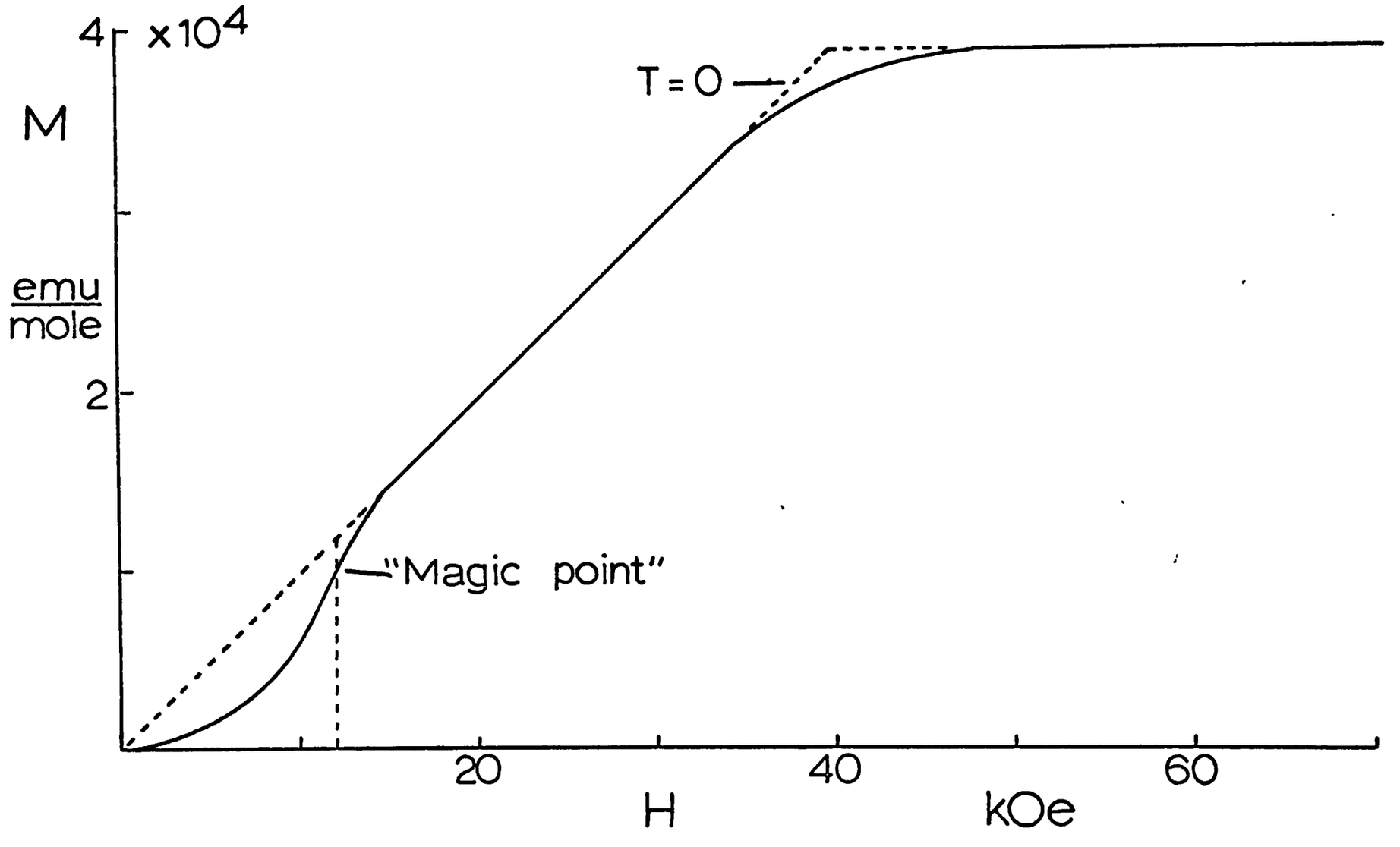
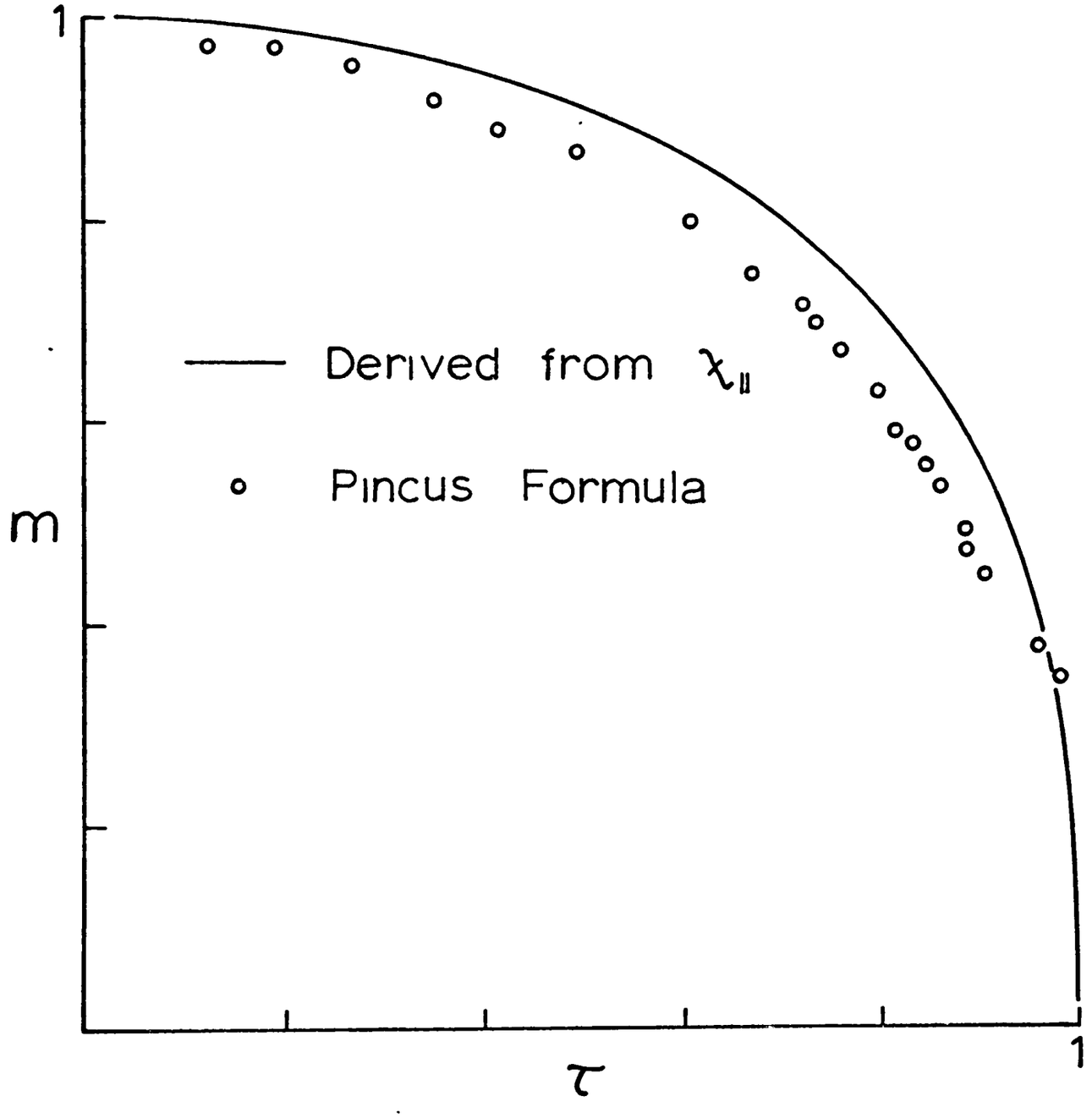


Fig. 3-8



$$\delta m = 0.0249$$

for S = 5/2 and the value for S = 7/2 should be slightly less than this.

The agreement between these predictions and our value of $\delta m = 0.023$ can be seen to be very good. However it should be remembered that all previously measured values[41] have been considerably less than the theoretical estimates and it is believed that the current theoretical estimates are too large. This is because they have been calculated in the presence of an infinitesimal anisotropy which serves only to define a preferred direction in the crystal, whereas in real crystals the finite anisotropy plays a considerable role in reducing the spin deviation.

3-8. Sublattice Magnetization from the Spin Flop Area.

Instead of using the formula of Pincus as in the previous section, it should be possible to derive a similar result by using molecular field theory to write down the energy of the two points which are common to all the moment measurements. These are the origin (M=0, H=0) which we shall call point 1, and the "magic point" (11,200 emu/mole, 12.0 Kg) which we shall call point 2. Then the area under the spin flop which we measure is simply the difference between the energies of these two

points.

It is interesting that this implies that in the idealized picture of a spin flop at T = 0 where M = 0 for $H < H_c$ and then a vertical rise at $H = H_c$, there is no energy difference between states 1 and 2.

In state 1, we have no applied field, so if we consider only the exchange interaction on a molecular field approximation and a DS_z^2 term to incorporate the anisotropy, we have the same partition function as in Eq.3-5.

$$Z_1 = \sum_{S_z} \exp\left[\left\{g\beta H_E m S_z - D\left[S_z^2 - 1/3\ S(S+1)\right]\right\}/kT\right]$$

From this it follows immediately that the energy of state 1 is:

$$E_1 = -N \frac{\sum \left(\frac{1}{2}g\beta H_E m S_z - DS_z'^2\right) \exp\left[\left(g\beta H_E m S_z - DS_z'^2\right)/kT\right]}{\sum \exp\left[\left(g\beta H_E m S_z - DS_z'^2\right)/kT\right]} \quad ..(3\text{-}6)$$

where the factor of $\frac{1}{2}$ is to avoid summing all the exchange interactions twice, and we have put $S_z'^2 = S_z^2 - 1/3S(S+1)$.

In state 2, after the flop, we have a situation where the sublattice magnetizations are in the b-c plane, although individual spins need not necessarily be in the b-c plane.

In a two sublattice model, let the resultant sublattice magnetizations both be inclined at an angle θ

to the c-axis. The resultant field on each sublattice must then be along this direction and so we can take it as our axis of quantization. If we then consider just the z-components of the spins along the direction θ, we have three components for the energy of each ion in an applied field H:

$$E_{ex} = -g\beta H_E m' S_z \cos 2\theta$$

$$E_h = -g\beta H S_z \sin\theta$$

$$E_{cef} = D\left[S_z^2 - 1/3\ S(S+1)\right]\sin^2\theta$$

where the sublattice magnetization m' is not equal to its value m below the flop.

If we simplify the notation by writing:

$$P = g\beta(H_E m' \cos 2\theta + H \sin\theta)$$

then we have the partition function

$$Z = \Sigma \exp\left[(PS_z - DS_z'^2 \sin^2\theta)/kT\right]$$

the energy of state 2 as

$$E_2 = -N \frac{\Sigma(P'S_z - DS_z'^2\sin^2\theta)\ \exp\left[(PS_z - DS_z'^2\sin^2\theta)/kT\right]}{\Sigma \exp\left[(PS_z - DS_z'^2\sin^2\theta)/kT\right]} \quad ...(3\text{-}7)$$

and the magnetic moment

$$M = Ng\beta \frac{\Sigma S_z \exp\left[(PS_z - DS_z'^2\sin^2\theta)/kT\right]}{\Sigma \exp\left[(PS_z - DS_z'^2\sin^2\theta)/kT\right]} \sin\theta \quad ...(3\text{-}8)$$

where P' differs from P in having a factor $\frac{1}{2}$ in the exchange term as in Eq.3-6.

We still need one further equation before we can solve the problem and this is provided by the condition that the resultant of our three effective fields must be along the direction θ. This gives us the equation

$$g\beta H \cos\theta + D\cos^2\theta = g\beta H_E m' \sin 2\theta \quad \ldots(3\text{-}9)$$

We are now in a position where, by inserting the experimental values for M and H, we can solve equations (3-8) and (3-9) self-consistently for the only unknown $H_E m'$ as a function of temperature.

We do not need to separate these two variables for the result can then be put into Eq.3-7 to give us the energy of state 2 as a function of temperature. We now use our initial premise that:

$$E_1 - E_2 = \text{Spin Flop Area}$$

to obtain E_1 from our experimentally measured areas.

Now the only unknown in Eq.3-6 is the sublattice magnetization m, so this equation may be solved for each temperature at which we have measured the spin flop to give us the temperature dependence of the sublattice magnetization.

This procedure was carried out by computer and the results obtained are shown in Fig.3-9 together with

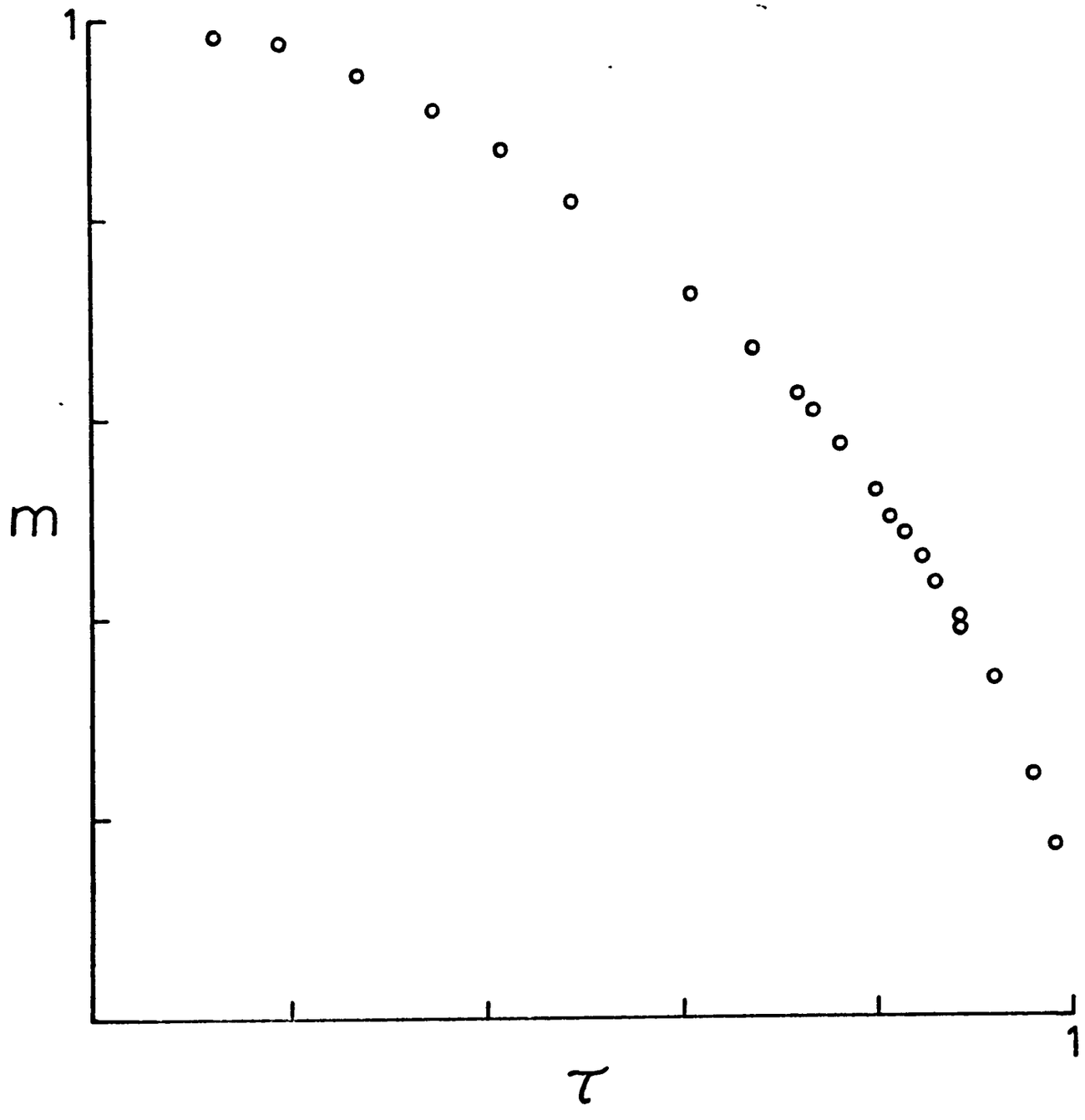


Fig. 3-9

the curve from Section 3-4, which was derived from $\chi_{\parallel}$ by the method of Hornreich and Shtrikman.

The present method can be seen to underestimate the sublattice magnetization and there is clearly scope for improving the theory. The most obvious deficiency is the omission of the other two components of the spin which do not have a zero average effect on the magnetic moment. Although one must remember that molecular field theory does not give good estimates for the energy, it should be possible to obtain closer correlation than that shown in Fig.3-9.

If the curve is extrapolated to T = 0 it would seem once again that it does not reach the value m = 1. However in this case the difference is $\lesssim 0.5\%$ which correlates much better with experimental values[41] for the spin deviation. Our present theory should be better at the low temperature end when most of the spins will be in the +7/2 state and our neglect of the other two spin components is less serious.

3-9. Summary.

The main theme of this chapter has been to show the large difference in accuracy of the molecular field

theory when performing calculations from first principles, contrasted to its accuracy when used for comparing two sets of experimental results.

To show this the sublattice magnetization was calculated in six different ways. In general, the methods which used MFT to derive the sublattice magnetization from another set of experimental results gave better results than the method which used MFT from experimentally derived parameters.

Another method, due to Eisele and Keffer, also worked from experimentally derived parameters using spin wave theory and gave a much better fit than the similar MFT method for the low temperature region, but as expected deviated markedly near the Néel temperature.

Two of the derived sublattice magnetizations were obtained from the area contained under a spin flop curve, and were unusual in obtaining a finite spin deviation at $T = 0$.

The magnetic phase diagram on the H - T plane was obtained from measurements of the magnetic moment and compared with the phase diagram obtained by Blazey and Rohrer.

Fisher's relation, that a graph of specific heat against $\frac{\partial}{\partial T}(\chi_{\parallel} T)$ should be a linear function while passing through the Néel temperature, was tested and found to be valid.

CHAPTER FOUR

GADOLINIUM ALUMINATE

The EXCHANGE and CRYSTAL FIELD INTERACTIONS.

4-1. Introduction.

This chapter will be concerned entirely with the various interactions in $GdAlO_3$ and estimates of their magnitudes and effect on the physical properties of the crystal.

Magnetic ordering can be achieved by magnetic dipole-dipole interactions or by the electrostatic exchange interactions. The relative contributions of these mechanisms will be calculated including both the effect of Heisenberg (or Ising) $\underline{S}_i \cdot \underline{S}_j$ exchange and Dzialoshinskii-Moriya $\underline{S}_i \times \underline{S}_j$ exchange.

We have already observed in the magnetic moment and susceptibility measurements evidence of an orthorhombic symmetry anisotropy. An interpretation of the cause of this anisotropy in terms of the crystal field parameters will be given.

Finally explanations for some of the questions left unanswered at the end of Chapter 2 will be given, together with the prediction of an effect which we can not observe experimentally - a temperature dependence of the direction of the sublattice magnetizations.

4-2. Consideration of Possible Interactions.

The easiest interaction to consider first is the dipole-dipole interaction. This had already been dealt with by Hawkes[14], but the values of the distortion parameters x and y (see section 1-3) were not known and consequently he evaluated the dipole fields using the distortions for $GdFeO_3$ (x = -0.018, y = 0.062), and also for x = y = 0, assuming that the distortions for $GdAlO_3$ lay between these values.

The full crystallographic parameters for $GdAlO_3$ have recently been determined by Gee[42], who obtained the values x = -0.01, y = 0.038. Accordingly the values of the dipole fields for each of the eight allowed magnetic configurations have been evaluated using the new parameters and the values given in Table 4-I. In the case of the arrangements in the a-b plane, when canting is allowed, the dipole fields have been evaluated for the

TABLE 4-I

Dipole Fields for $GdAlO_3$.

Configuration	Field (kOe)
G_x	+0.10
G_y	-0.30
G_z	+0.20
A_x	+5.97
A_y	+6.05
A_z	-12.02
C_x	-3.19
C_y	-3.32
C_z	+6.51
F_x	-0.01
F_y	+0.10
F_z	-0.10

+ indicates a favourable field.

- indicates an unfavourable field.

Lattice parameters: a = 5.247A x = -0.010

b = 5.304A y = +0.038

c = 7.447A

two cases of the moments aligned parallel to each of the a- and b-axes, i.e. for the case A_xG_y we have evaluated the dipole field for pure A_x and pure G_y.

For the case we are most interested in, G_y, it can be seen that the dipole field gives rise to a small and unfavourable contribution to the magnetic ordering. Note the small magnitude of the dipole fields for the G and F configurations all of which vanish identically for an undistorted simple cubic lattice.

This result implies that exchange must be the cause of the magnetic ordering. Of the two types of exchange of the form $\underline{S}_i \cdot \underline{S}_j$ and $\underline{S}_i \times \underline{S}_j$ the former must always be allowed. It is therefore more convenient to consider the latter as applied to this crystal structure.

The Hamiltonian for Dzialoshinskii exchange is:

$$\mathcal{H} = \underline{D}_{ij} \cdot \underline{S}_i \times \underline{S}_j$$

and there are several group theoretical rules governing the allowed form of the vector coefficient $\underline{D}_{ij}$. The first of these is the rule that if $\underline{S}_i$ and $\underline{S}_j$ are connected by inversion symmetry then $\underline{D}_{ij} = 0$. This means that there can be no coupling between ions 1 and 2 on Fig.1-7.

The second rule states that if $\underline{S}_i$ and $\underline{S}_j$ lie in a mirror plane then $\underline{D}_{ij}$ must be perpendicular to the

mirror plane. In other words coupling is allowed between ions 1 and 4, with $\underline{D}_{ij}$ being parallel to the c-axis, and similarly between the next nearest neighbours 1 and 1'.

Coupling is also allowed between ions 1 and 3 which are connected by the glide plane, n. In this case $\underline{D}_{ij}$ must be parallel to the symmetry plane, i.e. it lies in the a-c plane. However since ions 1 and 3 are next nearest neighbours, this coefficient should be much smaller than that between ions 1 and 4.

Thus if this kind of coupling is significant (which it is in the isomorphous orthoferrites) we would expect to have exchange coupling only between neighbours in the a-b plane, and we would obtain results characteristic of a two dimensional antiferromagnet. In fact our results have been characteristic of a three dimensional antiferromagnet (see e.g. Table 2-I) and so we must conclude that Dzialoshinskii-Moriya exchange is not important in deciding the magnetic ordering of gadolinium aluminate. This is not surprising since it is expected that this type of coupling should be small for S-state ions.

This only leaves exchange of the $\underline{S}_i \cdot \underline{S}_j$ type to consider as the cause for magnetic ordering, and we saw

when considering the specific heat results in section 2-3 that they fitted much better to the pattern of the three component Heisenberg $\underline{S}_i.\underline{S}_j$ exchange, than to the single component Ising $S_{iz}S_{jz}$.

The origin of the anisotropy must also be considered, and the mechanism should be capable of predicting the b-axis as the ordering direction.

Two possible methods of producing the anisotropy have already been considered under the exchange mechanisms. Dzialoshinskii-Moriya exchange we concluded to be negligible and dipole-dipole interactions, while finite, are too small to even account for the anisotropy of about 3kOe, in addition to being in the wrong direction.

This leaves the crystal field interaction as the most likely candidate as cause of the anisotropy. We can calculate the Gd-O distances between the twelve surrounding oxygens of a gadolinium ion using the parameters determined by Gee. For the two different oxygen sites he obtained the values:

4c sites	$x = 0.070$	$y = 0.490$	$z = 0.250$
8d sites	$x' = -0.286$	$y' = 0.287$	$z' = 0.041$

Fig.4-1 shows the detailed arrangement of oxygen

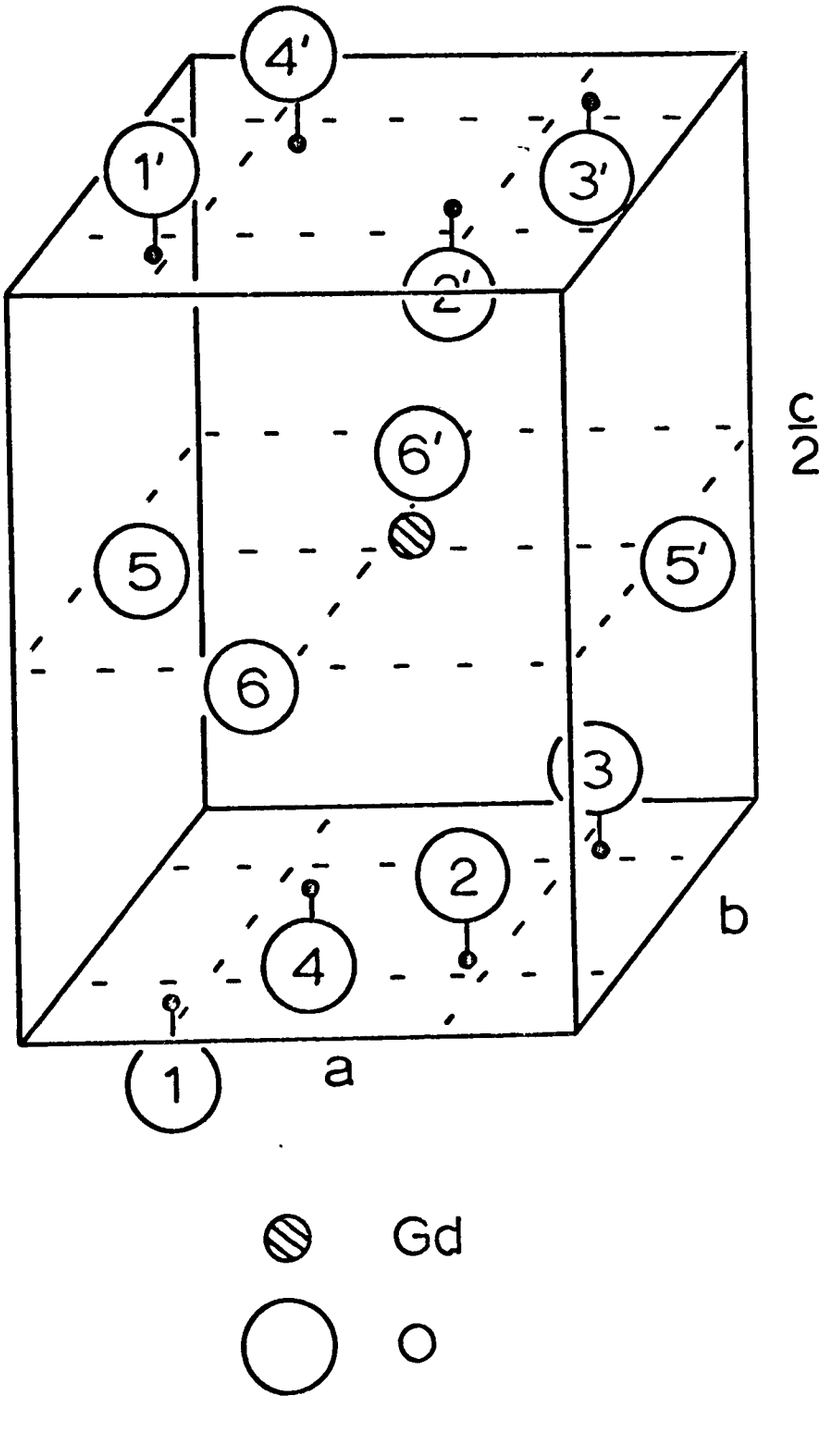


Fig. 4-1

atoms surrounding a gadolinium atom. Since the gadolinium site is on a mirror plane it is equidistant from the pairs of oxygens above and below (e.g. 1 and 1') However it is not equidistant from the equivalent ions (5,5') and (6,6').

From Table 4-II we can see that the major anisotropy is provided by the ions (1,1') along a direction midway between the a- and b-axes. We can also see that since 5' - 5 is greater (0.61A) than 6' - 6 (0.48A) then this will result in the direction of principal anisotropy moving nearer to the b-axis.

If we carry out a point charge calculation from these parameters we obtain the value 38° from the b-axis as the direction of principal anisotropy. This compares well with the results of Hawkes[14] on Er^{3+} and Dy^{3+} in $GdAlO_3$ and also with the value for $DyAlO_3$[43] (33°). We would expect the angle to be larger than that for the more distorted $DyAlO_3$ since it must coincide with the pseudo-cubic axis (45°) when the distortions go to zero.

Thus an anisotropy due to the CEF does lead us to expect that the b-axis will be most favoured of the orthorhombic axes. Further it predicts that the principle axis of the anisotropy will be influenced towards the pseudo-cubic axis by the oxygens of type 1.

TABLE 4-II

Gadolinium - Oxygen Distances.

Oxygen	Distance
1	3.17A
2	2.30A
3	2.51A
4	2.64A
5	2.33A
5'	2.94A
6	2.44A
6'	2.92A

Under these assumptions of the nature of the ordering and anisotropy interactions we can now go ahead and estimate the size of the parameters involved.

4-3. Crystal Field Parameters from Moment Measurements.

The magnetic moment measurements described in Section 2-5 give us an estimate of the anisotropy between the three crystallographic axes. This is only sufficient to determine two parameters and it is fortunate that White et al.[17] have shown from their experiments on $YAlO_3$ that the quadratic CEF term is very much more important than either the fourth or sixth order terms.

In deriving formulae for the saturation fields we shall leave the direction of the CEF axes general and denote the two axes as the α- and β-axes where the α-axis makes an angle $\pm\lambda$ with the b-axis for each of the two inequivalent magnetic sites. We may now write the CEF Hamiltonian as:

$$\mathcal{H}_{CEF} = DS_\alpha^2 + E(S_c^2 - S_\beta^2) \qquad \ldots(4\text{-}1)$$

and using the MFT, write down an expression for the energy of the crystal when an external field, H, is applied along each of the orthorhombic axes in turn. For simplicity we have left out the term -1/3 DS(S+1) which

would disappear on differentiation anyway.

Using the appropriate diagram in Fig.4-2 we may write the energy for each case as:

$$E_a = -\tfrac{1}{2}Ng\beta SH(\cos\theta_1+\cos\theta_2) - \tfrac{1}{3}NzJS^2\left[\cos2\theta_1+\cos2\theta_2+\cos(\theta_1+\theta_2)\right]$$
$$+\tfrac{1}{2}NDS^2\left[\sin^2(\theta_1+\lambda) + \sin^2(\theta_2-\lambda)\right]$$
$$+\tfrac{1}{2}NES^2\left[\cos^2(\theta_1+\lambda) + \cos^2(\theta_2-\lambda)\right]$$
$$- \tfrac{1}{4}Ng\beta S\left[4790(\cos^2\theta_1 + \cos^2\theta_2) - 5978\cos\theta_1\cos\theta_2 + 3028\sin\theta_1\sin\theta_2 - 3620\right]$$

$$E_b = -Ng\beta SH\cos\theta - \tfrac{1}{3}NzJS^2(\cos2\theta + 2 - 4\sin^2\theta\cos^2\eta)$$
$$-\tfrac{1}{2}Ng\beta S(A_x\sin^2\theta\sin^2\eta + F_y\cos^2\theta + G_z\sin^2\theta\cos^2\eta)$$
$$+NDS^2(\sin^2\theta\sin^2\eta\sin^2\lambda + \cos^2\theta\cos^2\lambda)$$
$$+NES^2(\sin^2\theta\cos^2\eta - \sin^2\theta\sin^2\eta\cos^2\lambda - \cos^2\theta\sin^2\lambda)$$

$$E_c = -Ng\beta SH\cos\theta - \tfrac{1}{3}NzJS^2(\cos2\theta + 2 - 4\sin^2\theta\cos^2\eta)$$
$$-\tfrac{1}{2}Ng\beta S(A_x\sin^2\theta\sin^2\eta + G_y\sin^2\theta\cos^2\eta + F_z\cos^2\theta)$$
$$+NDS^2\sin^2\theta\cos^2(\lambda-\eta) + NES^2\left[\cos^2\theta - \sin^2\theta\sin^2(\lambda-\eta)\right]$$

where we have introduced the nearest neighbour exchange constant J, between the z nearest neighbours as

$$H_{ex} = -2J\,\Sigma\,\underline{S}_i\cdot\underline{S}_j$$

The appropriate dipole fields are obtained from Table 4-I

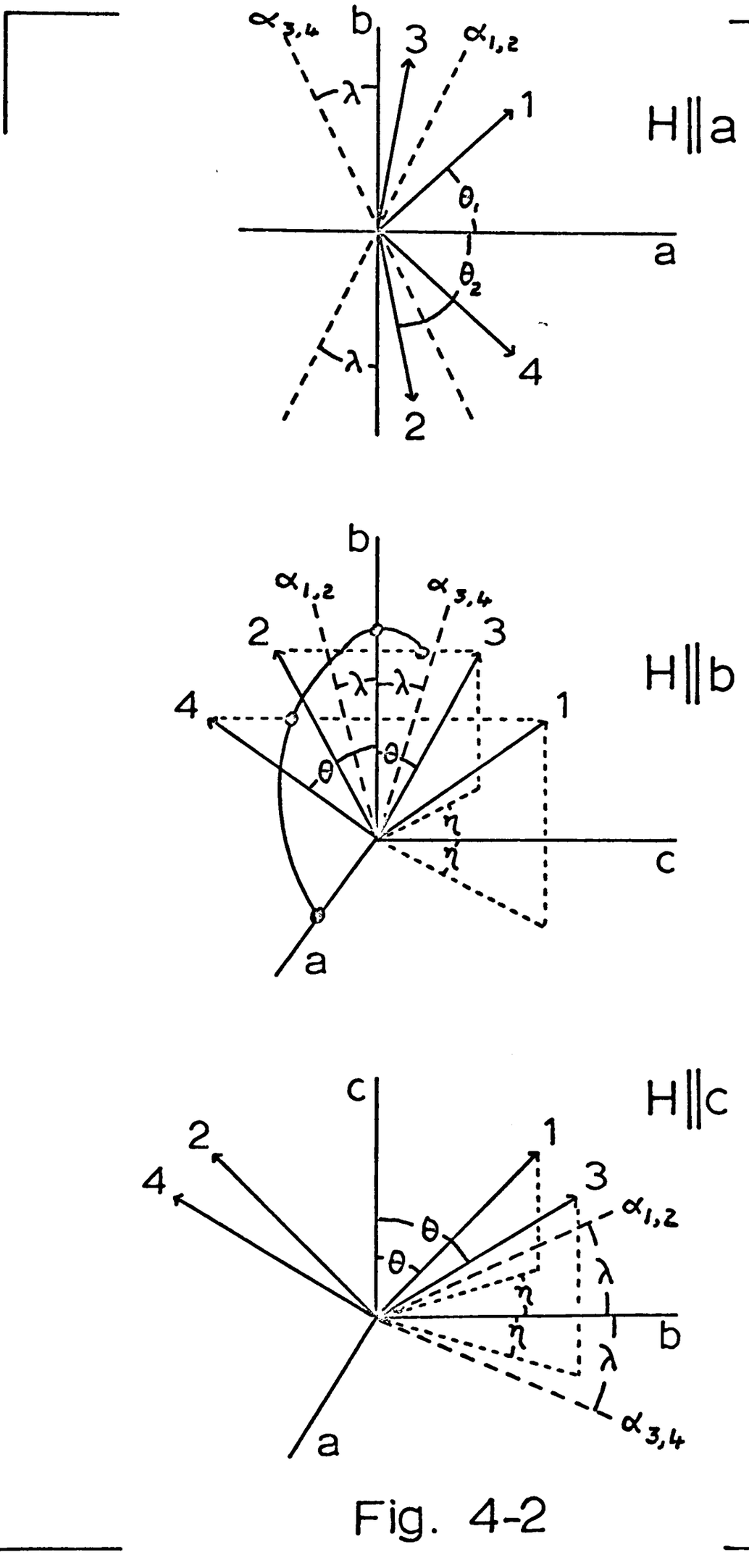


Fig. 4-2

except the a-axis where the configuration does not correspond to an F, G, C or A mode and these have therefore been calculated numerically.

Differentiating each of the above three expressions with respect to θ and then letting $\theta \to 0$ enables us to find the applied field necessary to achieve magnetic saturation along each of the three axes. The results are:

$$H_a^{sat} = -4z\frac{JS}{g\beta} - \frac{2S}{g\beta}(D + E)\cos 2\lambda - 287$$

$$H_b^{sat} = -\frac{4}{3}z\frac{JS}{g\beta}(1+2\cos^2\eta) + 2\frac{DS}{g\beta}(\cos^2\lambda - \sin^2\lambda\sin^2\eta)$$
$$+ 2\frac{ES}{g\beta}(\sin^2\eta\cos^2\lambda - \sin^2\lambda - \cos^2\eta)$$
$$+ A_x\sin^2\eta - F_y + G_z\cos^2\eta$$

$$H_c^{sat} = -\frac{4}{3}z\frac{JS}{g\beta}(1+2\cos^2\eta) - 2\frac{DS}{g\beta}\cos^2(\lambda-\eta) + 2\frac{ES}{g\beta}\left[1+\sin^2(\lambda-\eta)\right]$$
$$+ A_x\sin^2\eta + G_y\cos^2\eta - F_z$$

Differentiation of the last two energy expressions w.r.t. η allows us to also find the appropriate value of η and so solve the above three equations for J, D and E. For the c-axis this differentiation is carried out in Section 4-7 for H = 0 but the answer is in fact independent of H and so we may use the T = 0 value of $\eta = 8.9^\circ$

For the b-axis the surprising but simplifying answer $\eta = 0$ is obtained showing that (within the MFT approximation) the moments do flop exactly in the b-c plane.

At this stage we need to insert a value for λ. If we take $\lambda = 0$ we get:

$$D/k = -0.050^{\circ}K$$

$$E/k = -0.005^{\circ}K$$

However if we insert the more realistic value $\lambda = 38^{\circ}$ obtained in the previous section we get:

$$D/k = -0.293^{\circ}K$$

$$E/k = -0.112^{\circ}K$$

It can be seen that the values depend enormously on the estimate of λ and it is fortunate that for most purposes we only require the components along the orthorhombic axes.

4-4. CEF Parameters from Susceptibility Measurements.

As already mentioned, the Weiss θ as measured in the hydrogen range susceptibility measurements has a dependence on the CEF. This dependence has been calculated by Roberts, Murray and Dabbs[44] for the case of a DS_z^2 term only.

In order to obtain values analogous to those of the previous section, we have extended the calculation of Roberts et al. to include an E term as well.

The method is to take the Hamiltonian for the system:

$$\mathcal{H} = D\left[S_\alpha^2 - 1/3\ S(S+1)\right] + E(S_c^2 - S_\beta^2) + g\beta\underline{H}.\underline{S}$$

and evaluate the coefficient of H^2 in $Tr(\mathcal{H}^2)$ for the cases where H is parallel to each of the α, β and c axes.

The results are:

$$\chi_\alpha = \frac{C}{T + \frac{D}{15k}(2S-1)(2S+3)}$$

$$\chi_\beta = \frac{C}{T - \left[\frac{D}{30k} + \frac{E}{10k}\right](2S-1)(2S+3)}$$

$$\chi_c = \frac{C}{T - \left[\frac{D}{30k} - \frac{E}{10k}\right](2S-1)(2S+3)}$$

where C is the molar Curie constant = $Ng^2\beta^2\ S(S+1)/3k$. These formulae reduce to the results of Roberts et al. if we put E = 0.

Converting these formulae to the orthorhombic axes (and substituting S = 7/2), we get for the difference in the θ values from the mean $\theta = 4.81^\circ K$, due to the exchange:

$$k\,\delta\theta_a = 4D\sin^2\lambda - (2D + 6E)\cos^2\lambda$$

$$k\,\delta\theta_b = 4D\cos^2\lambda - (2D + 6E)\sin^2\lambda$$

$$k\,\delta\theta_c = -2D + 6E$$

There is also a small contribution due to the dipole field given by:

$$k\,\delta\theta_i = g\beta F_i(S+1)/3$$

Substituting the θ values from Section 2-4 and again putting $\lambda = 38^\circ$ gives:

$$D/k = -0.115^\circ K$$

$$E/k = -0.030^\circ K$$

These values differ by over a factor of 2 from those obtained in the previous section - a difference which can be reduced but not removed by altering the size of λ. The reason can be seen quite quickly from a consideration of the errors involved.

In both cases we have had to subtract two numbers of the same magnitude. The accuracy of the intercepts of the moment curves is ± 0.1kOe giving an error in the CEF values of $\pm$ 4%. However the accuracy of the Weiss θ values is probably $\pm 0.1^\circ K$ giving a possible error of over 100%.

Therefore we conclude that the estimates of D

and E obtained in the previous section are very much more accurate, and they will be used for the remainder of the chapter when we need to insert values for the crystal field parameters.

4-5. Estimates of the Exchange Parameter.

All theories of magnetic ordering must assume some kind of interaction parameter which then occurs in the expressions for the various measurable quantities.

In the case of $GdAlO_3$ we have shown that all the experimental evidence so far can be explained in terms of the Hamiltonian:

$$\mathcal{H} = -2 \Sigma J_{ij} \underline{S}_i \cdot \underline{S}_j + D\left[S_\alpha^2 - 1/3\ S(S+1)\right] + E(S_c^2 - S_\beta^2) \quad .(4-2)$$

where the summation only needs to run over pairs of nearest neighbours, and we have defined the α, β and c axes in Section 4-3.

Most of the theories on co-operative magnetism deal with a Hamiltonian comprising only our first term for deriving estimates of the nearest neighbour exchange parameter J. However, many of the measured properties are sensitive to the size of crystal field interactions as became evident for example in Section 3-6, when the ordering temperature increased as D became more negative.

This result is physically reasonable because the CEF is helping to lower the energy of the $S_z = \pm S$ states and thus increasing $|\langle \underline{S}_i \cdot \underline{S}_j \rangle|$.

Of course in the graph of these results (Fig.3-6), this effect is not apparent since it is plotted on a reduced temperature scale. In any case it has been shown by Lines[45] that this simple MFT calculation does not give a good quantitative estimate of the effect of the CEF on T_N, and he has calculated, using the Green's function approach, a more accurate estimate with the results presented in the form of a graph of $T_N(D) / T_N(0)$ against D/J.

In view of this, it was decided to put a DS_z^2 type term into the Hamiltonians for several other methods of estimating J and see if the consistency of the values obtained for J could be improved.

The results are shown in Table 4-III and are quoted in terms of the exchange field rather than the exchange constant J. The two are simply related by:

$$g\beta H_E = 2zSJ.$$

A brief explanation of the derivation of the results in Table 4-III will be given. In all cases the value of D chosen to take account of crystal field effects,

TABLE 4-III

Values of the Exchange Field.

Method	T_N	χ	Moment	Sp.ht.
MFT $\chi(T_N)$		21.8		
MFT 2s/1 saturation			21.0	
MFT 4s/1 saturation			20.4	
MFT spin flop			20.7	
MFT energy				21.2
BPW/GF T_N	19.8			
BPW $\chi(T_N)$		20.2		
HTE/GF T_N	21.6			
HTE Sp.ht. tail				21.4
GF T_N	20.6			
GF $\chi_\perp(0)$		21.0		

$$J/k = -3.20 \times 10^{-5} H_E$$

MFT Molecular Field Theory.

BPW Bethe-Peierls-Weiss cluster.

HTE High Temperature Expansion.

GF Green's Function method.

is that between the b-axis and the average in the a-c plane. This is equivalent to the case $\lambda = 0$ considered in Section 4-3 and gives $D/k = -0.050^{\circ}K$.

In all cases the starting formula used is that appropriate to simple cubic, $S = 7/2$, nearest neighbour Heisenberg exchange.

The three values derived from the Néel temperature of 3.870° were obtained using the formulae of Smart[46], Rushbrooke and Wood[47] and Lui and Lee[48] respectively, while incorporating the effect of the CEF by use of Lines' graph mentioned above. (Note that Lines' Hamiltonian uses a J which is twice the magnitude of ours.) Since Lines' results are given in terms of the ratio D/J, we must first estimate a value for J to find the CEF contribution to T_N and then substitute the part of T_N due to the exchange into the other three formulae. The new value of J obtained can then be used to re-estimate the CEF contribution and so on, until the value of J stops altering as we go around the loop. As Lines' results are only plotted for $S = 1$ and $S = \infty$, interpolation was carried out on a 1/S scale to obtain the value for $S = 7/2$.

It is also proved in Lines' paper that the

value of χ at the Néel temperature is independent of D, so the values there were obtained directly from the formulae of Smart[46]. Smart also quotes formulae for the constant coupling approximation which give identical answers to the BPW figures for large values of S and so are not given here.

Lines[49] has evaluated the temperature dependence of $\chi_\perp$ using a Green's function approach, and the result from his formula is given for T = 0, where we have assumed that this is independent of D in a similar manner to $\chi(T_N)$. From the discussion in Section 3-7 and consideration of the experimental results, we have taken the spin deviation at T = 0 to be 0.3%.

The method of estimating the exchange field from the values of applied field necessary to achieve saturation have already been given in Section 2-5 for the two sublattice model and in Section 4-3 for the four sublattice model with canted crystal field axes.

The spin flop field can also be evaluated on this latter model using molecular field theory. The resultant expression is:

$$H_E = (H_\parallel^2 - H_c^2)/2H_\parallel$$

where the CEF dependence is correctly included in $H_\parallel$,

the applied field required for magnetic saturation in the parallel direction.

(Note that the spin flop which we have taken is that corresponding to the minimum free energy, usually written:

$$H_c^2 = 2H_E H_A - H_A^2$$

As has been pointed out by Anderson and Callen[50] two different formulae can be obtained from the spin wave instability conditions which predict a difference between the fields at the a.f.→s.f. and the s.f.→a.f. transitions. The minimum free energy solution lies between these two values.)

From the Hamiltonian Eq.4-2 we can say that the energy of the system at T = 0 is:

$$E_o = NzJS^2\left[1 + \frac{0.6}{zS}\right] + \frac{2}{3}NDS(S+1)$$

where the extra factor in the exchange term is to take account of the antiferromagnetic ground state problem[39]. Since at high temperatures the magnetic energy is zero, we can equate $-E_o$ to the energy as measured under the specific heat curve.

The other estimate from the specific heat is obtained by assuming that at high temperatures we may

write the specific heat as an expansion

$$\frac{C}{R} = \frac{\langle E_i^2 \rangle}{k^2 T^2} + \text{higher order terms.}$$

Using the properties:

$$\langle (S_i . S_j)^2 \rangle = 1/3\ S^2(S+1)^2$$

$$\langle Sz^4 \rangle = 1/15\ S(S+1)(3S^2+3S-1)$$

and the expression[51] for the dipole contribution for simple cubic lattices.

$$\frac{C}{R} = 2.8\left[\frac{N_v g^2 \beta^2\ S(S+1)}{3kT}\right]^2$$

where N_v is the number of atoms per unit volume, we can derive the coefficient of $1/T^2$.

In a collection of data such as Table 4-III, where different degrees of confidence could be attached to the individual datum, it is difficult to know how to estimate the "best" value. However it is encouraging to note that both the mean and the median give the value H_E = 21.0kOe ($J/k = -0.0671^{\circ}K$) and we shall therefore take this as our estimate of the nearest neighbour exchange for $GdAlO_3$ with a probable error of $\pm$ 2%.

The formulae used in this section depend on J in several different ways e.g. the specific heat $1/T^2$ tail depends on zJ^2 while most other coefficients vary

as zJ. Also any possible second nearest neighbour exchange can produce positive or negative contributions. In view of the consistency of the results obtained we can conclude that we have chosen the correct model for the interactions and are justified in neglecting second nearest neighbour exchange.

4-6. Miscellaneous Explanations.

We have now answered two of the questions left at the end of Chapter 2 and will here try and deal with the remaining ones.

The ground work necessary for seeing the cause of the discrepancy between the measured entropy and energy values and those for the Heisenberg simple cubic $S = 7/2$ system in Table 2-I has been done in the preceding section. We showed there that the energy under the specific heat curve is reduced by the ratio:

$$1 + \frac{2D(S+1)}{3zJS\left(1 + \frac{0.6}{zS}\right)}$$

due to the CEF.

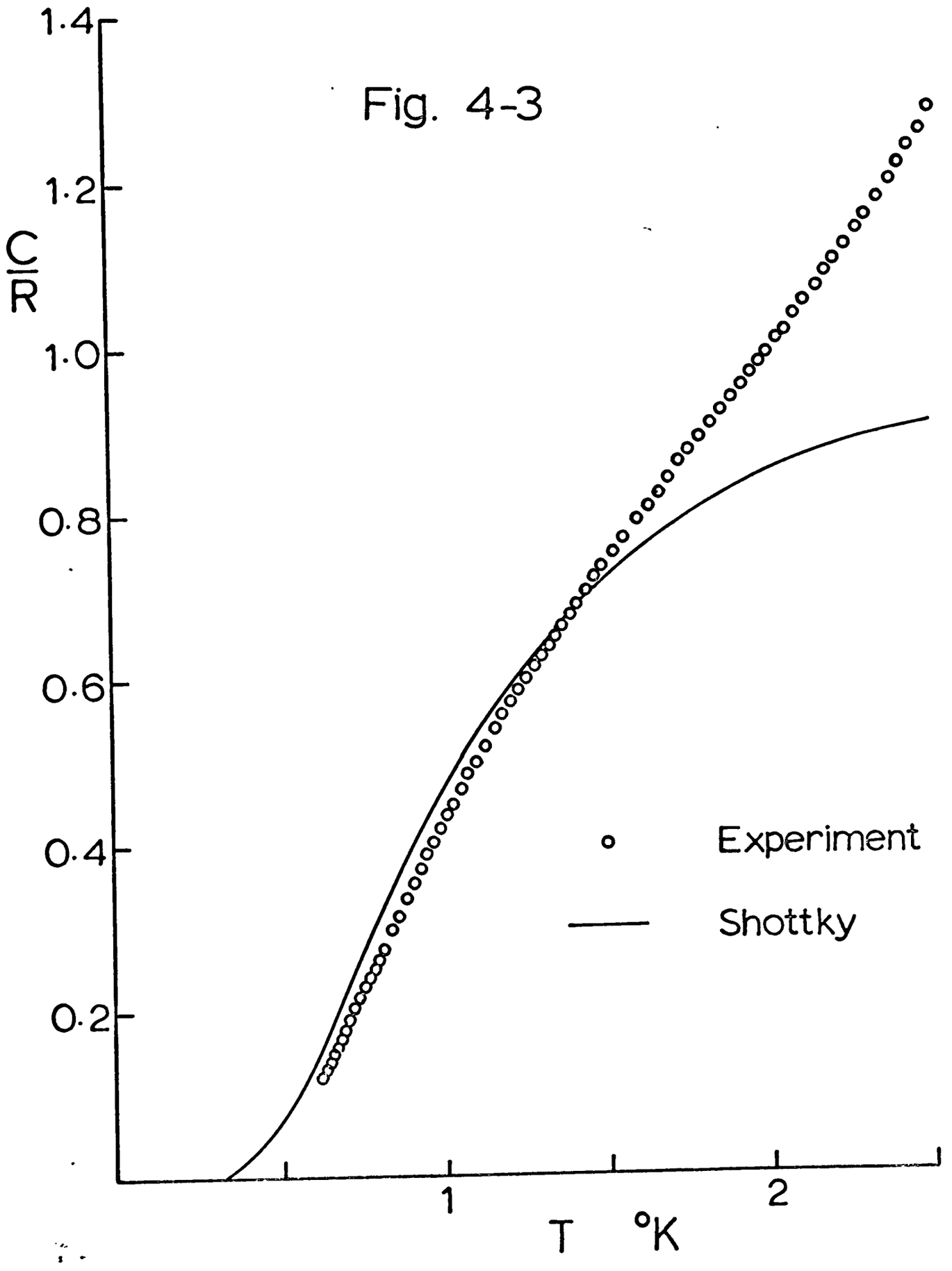
If we then increase our measured value for the energy of 1.465 by this ratio, we obtain the value 1.65 which is in good agreement with the predicted value of 1.67.

Unfortunately there is no simple way of working out the change in the energy distribution above and below the ordering temperature except by carrying out a lengthy and difficult high temperature expansion. However we do notice that most of the energy loss has been from the high temperature part. This can be explained by considering that the CEF has increased the ordering temperature, as shown in the previous section, and thus altered the energy distribution in favour of the low temperature part. Thus the total energy loss would be borne mainly by the high temperature tail.

We can check our values of the exchange and CEF parameters by considering that at low temperatures, when the sublattice magnetization and hence the exchange field is constant, then the specific heat should resemble a Shottky anomaly. Fig.4-3 shows the calculated Shottky specific heat from the split levels using the parameters from Sections 4-3 and 4-5, together with the experimental points and it can be seen that the fit is very good up to $1.2^{o}K$ ($\tau = 0.31$).

This is as good an agreement as we can expect since at this temperature the sublattice magnetization is starting to drop thus upsetting our assumed level splittings. The Shottky picture then becomes invalid

Fig. 4-3



and the λ-anomaly assumes the dominant role.

Finding a quantitative explanation of the temperature dependent bump in the c-axis moment curves is difficult. However a qualitative explanation could be as follows.

In zero applied field the sublattice magnetizations do not lie along the b-axis but are canted slightly in the a-b plane. When field is applied along the c-axis they will start turning towards it in the plane containing the c-axis and their initial direction. But the question arises whether they always stay in this plane or whether at some stage they find it energetically favourable to change their canting either towards the b-c plane or further away from it, with resultant increase in moment.

A simple molecular field theory calculation shows that the exchange, CEF and dipole energies all vary as $\cos^2\phi$ as we move away from the b-c plane so that there can be no change in the angle of minimum energy. However one effect has been neglected and that is the change in the effective sublattice magnetization from the equilibrium value at H = 0 to completely aligned at magnetic saturation. This will increase the effect of

the exchange term and so reduce the canting angle.

As so described we would expect the effect to be larger and to happen at lower fields when the sublattice magnetization is weaker, i.e. at temperatures near the ordering temperature, and this is in fact what is observed. It also explains why the temperature dependence of the position of the bump resembles that of the sublattice magnetization, because a fraction of the saturation moment, roughly equal to the sublattice magnetization, can be obtained before the value of the effective sublattice magnetization must begin to increase.

In their experiments on EuTe and $CoCl_2$, Jacobs and Silverstein[52] observed a moment in the perpendicular direction which increased faster than linearly with field near saturation. They attributed this also to an increase in the sublattice magnetization, but only from the equilibrium value in the antiferromagnetic state, when there will be a zero point spin deviation, to complete alignment in the saturated state.

Another qualitative explanation can be used to explain the peculiar temperature dependence of χ_a shown in Fig.2-5. As will be calculated in the next section, the canting angle of the four sublattice magnetizations

is a function of temperature, getting nearer to the b-axis as the temperature decreases.

However for temperatures just below T_N there is a considerable component of sublattice magnetization along the a-axis and thus the susceptibility starts to fall as one expects for a parallel direction. However as the temperature decreases further, the effective parallel component along the a-axis becomes smaller and so the susceptibility starts rising again to join the other perpendicular direction.

4-7. The Canting Angle.

We have now seen that the direction of the resultant sublattice magnetizations for each of the four sublattices is determined by competition between three interactions.

The dominant interaction is antiferromagnetic exchange, but this does not define a direction in the crystal. Its effect is merely to stipulate that a sublattice should try and lie antiparallel to the other two sublattices with which it interacts. Magnetic symmetry already states that it must lie exactly anti-parallel (or parallel) to one of these but the relationship

between the other two is such that they must be at equal angles $\pm\eta$ on opposite sides of the b-c plane. These conditions are best satisfied if the sublattices are parallel to the crystal axes in a G_x, G_y or G_z mode.

The dipole-dipole interactions are very small for these G modes, but as can be seen from Table 4-I, large favourable dipole fields are obtained for the A_x, A_y and C_z modes. Table 1-I shows that C_z is not allowed with any of the G modes by magnetic symmetry but the combinations A_xG_y and G_xA_y are allowed.

This leaves the crystal field interaction to decide between these two possibilities and since the low temperature state appears to be nearly simple antiferromagnetic alignment along the b-axis it must favour the A_xG_y mode and hence the CEF principal axis must be nearer to the b-axis as shown in Section 4-2.

However the first two of these three interactions are temperature dependent and therefore we can expect that the canting angle will also be a function of temperature, commencing at a direction determined mainly by the CEF at the Néel temperature, and the low temperature position being fixed mainly by the exchange.

If we differentiate w.r.t. η the formula given in Section 4-3 for the energy along the b-axis, we obtain the formula for the canting angle, η, as:

$$\tan 2\eta = \frac{(D+E)\ S \sin 2\lambda}{4/3\ zJSm^2 + g\beta m(A_x - G_y) + (D+E)S \cos 2\lambda}$$

At the Néel temperature we have $m = 0$ and so $\eta = \lambda$. A plot of η against temperature using the sublattice magnetization derived from $\chi_{\parallel}$ in Section 3-4 and the value $\lambda = 38^{\circ}$ is given in Fig.4-4. At low temperatures the canting angle is 8.9°.

Unfortunately it is very difficult to test the accuracy of this temperature dependence experimentally since the usual method for determining the direction of sublattice magnetization, neutron diffraction, is virtually eliminated by the enormous neutron absorption cross-section of natural gadolinium.

4-8. Summary.

We have now completed our study of the magnetic properties of gadolinium aluminate. All the observed effects can be explained on the basis of a four-sublattice system with dominant nearest neighbour Heisenberg exchange and negligible second nearest neighbour exchange. The

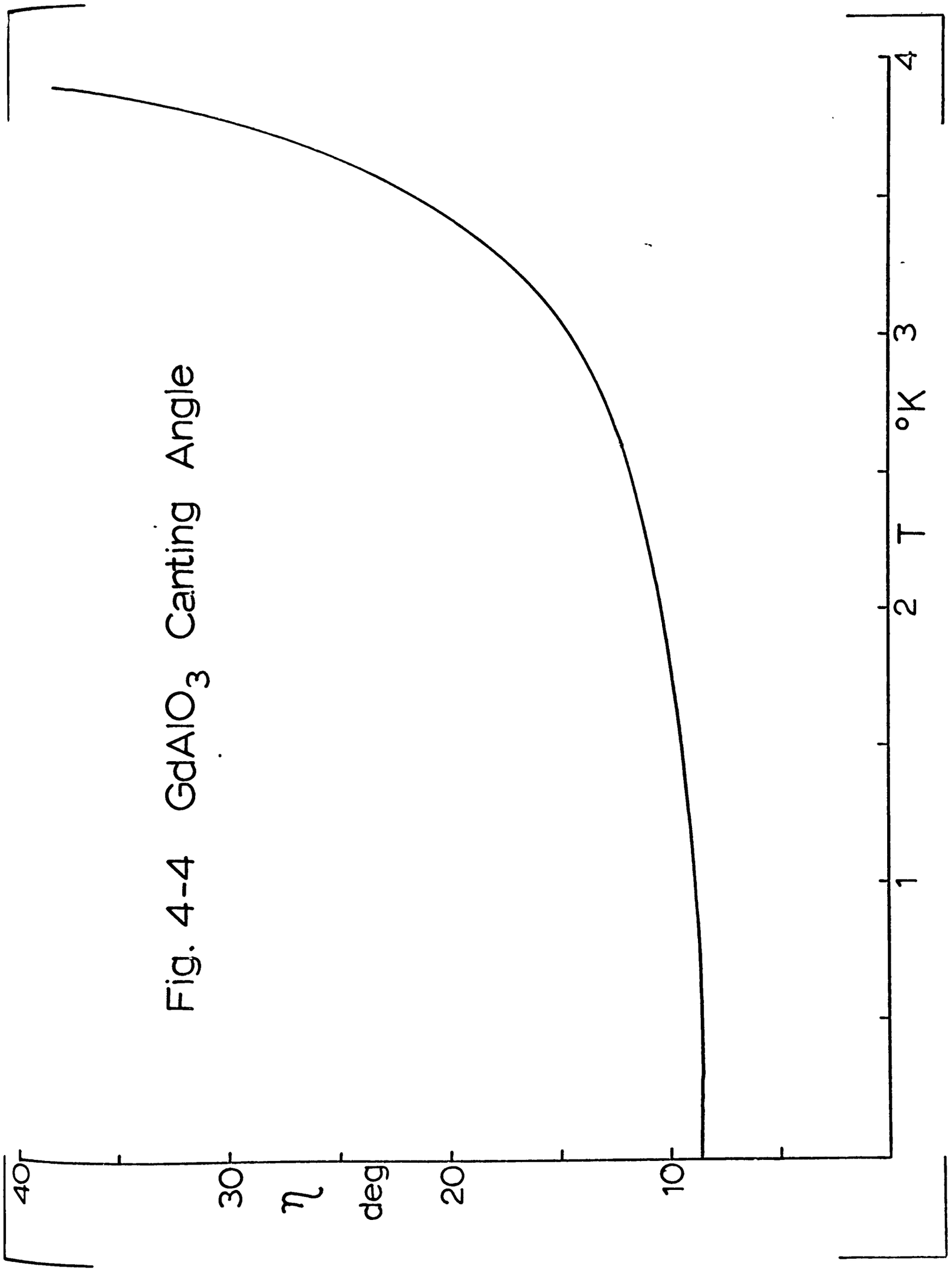


Fig. 4-4 $GdAlO_3$ Canting Angle

exchange constant was evaluated to be:

$$J/k = -0.0671^{\circ}K \pm 0.0013^{\circ}K.$$

The dipole-dipole interaction was found to have only a small effect on the magnetic ordering and the second most important interaction is the crystalline electric field (CEF). This is principally of second order and the coefficients were determined to be:

$$D/k = -0.293^{\circ}K$$

and

$$E/k = -0.112^{\circ}K$$

for the principal axis at 38° to the b-axis in the a-b plane.

All the questions left unanswered at the end of Chapter 2 have now been explained and to conclude a prediction has been made of the change in canting angle of the sublattices as a function of temperature.

CHAPTER FIVE

DYSPROSIUM ALUMINATE - EXPERIMENTAL RESULTS.

5-1. Introduction.

In contrast to the simplicity of the interactions in gadolinium aluminate, a much more complicated picture is presented by dysprosium aluminate.

The major difficulty is the introduction of very large anisotropy caused by the crystal field splitting. This is of the order of hundreds of degrees and consequently it is only the lowest lying Kramers' doublet of the $^6H_{15/2}$ ground state which is populated in the temperature range of our experiments.

This gives rise to an anisotropic g-value and to anisotropic interactions of an ion with its surroundings, including more than one kind of nearest neighbour exchange interaction. In gadolinium aluminate all of these were isotropic.

The other major difference is that the ordering in $DyAlO_3$ is mainly due to dipole-dipole interactions. This results in a different mode of ordering, G_xA_y, with a dominance of A_y compared with the mainly G_y mode of the

$GdAlO_3$ A_xG_y ordering.

Following a description in the next section of work carried out by other workers we will then detail the results of our specific heat, susceptibility and magnetic moment experiments. Analysis of the experiments will be shown to be consistent with a four sublattice arrangement of highly anisotropic magnetic ions in which the sublattices are canted at $\pm 33^{\circ}$ to the b-axis to give no net ferromagnetic moment.

5-2. Other Magnetic Measurements.

It is fortunate that there have been studies by two other techniques - neutron diffraction and optical spectroscopy - to complement our measurements and provide valuable information on the internal configurations. By determining the antiferromagnetic ordering arrangement and the g-values these measurements have considerably eased our task.

The neutron diffraction study was carried out by Bidaux and Meriel[43] and they found the ordering mode to be G_xA_y with the sublattices canted at $33^{\circ} \pm 2^{\circ}$ to the b-axis. They observed a magnetic moment of 8.6 Bohr magnetons/Dy^{3+} atom at $1.3^{\circ}K$ extrapolating to 8.8 Bohr magnetons at $T = 0^{\circ}K$.

They also showed that there are two possible kinds of G_xA_y ordering when one considers the distortions at the dysprosium site. These are fully dealt with in Appendix 1 for both the G_xA_y and A_xG_y modes and it is shown that the extra ordering mode does not occur in $GdAlO_3$.

Bidaux and Meriel determined the Néel temperature of $DyAlO_3$ to be $3.48 \pm 0.03^{o}K$ and calculated that the ordering is 70% due to dipolar coupling and 30% due to exchange. With dipolar coupling alone the most favoured mode would be pure A_y.

From the optical Zeeman spectroscopy of undoped $DyAlO_3$, Hufner et al.[54] have determined the directions and magnitudes of the principal axes of the g-tensor. As pointed out in Section 1-3, the c-axis must be a principal axis and the remaining two axes lie in the a-b plane, with the major axis (which we shall call the α-axis) being canted at $\pm 33.5^{o} \pm 1^{o}$ to the b-axis. Their results give:

$$g_c = 2.0 \pm 1.0$$
$$g_\alpha = 18.4 \pm 1.8$$
$$g_\beta = 3.2 \pm 1.0$$

where the β-axis is the remaining principal axis.

Hufner observed a triplet structure in the absorption lines at 20.4°K with a total splitting of 8.35°K. He attributed this splitting to Ising type exchange between nearest neighbours along the c-axis and calculated the magnitude of the interaction to be 1.2°K after allowing for the dipole contribution.

Ellis[53] has also studied the optical Zeeman spectra of $DyAlO_3$ and his preliminary results give values for g_c and g_α in good agreement with those of Hufner. However his value for g_β is twice as large as that obtained by Hufner. The origin of this discrepancy is not clear and we shall use the values of Hufner in analyzing our experimental results in view of the incomplete nature of Ellis' results.

Ellis also observed a linear shift in line position with applied field for fields greater than 50kOe, and extrapolated to zero field to obtain the energy of the flipped state in $DyAlO_3$. Comparison of this energy with the corresponding line position in the paramagnetic state at 20.4°K along the three principal axes then gives information about the strength of the internal interactions.

An a.c. susceptibility measurement was carried

out on polycrystalline $DyAlO_3$ by Schuchert et al.[55]. They obtained a Néel temperature of $3.5 \pm 0.2^{\circ}K$ and a Curie-Weiss law for $T > 6^{\circ}$ of:

$$\chi = \frac{C}{T + (18 \pm 3)}$$

It is perhaps relevant here to mention that the physical significance of the reported angle of 33° differs between the optical and neutron diffraction experiments. This is because optical spectroscopy measures the direction of the maximum splitting or g-value with no consideration of the direction of the sublattices whereas neutron diffraction directly measures the direction of net sublattice magnetization. The magnetic moment of 8.8 Bohr magnetons from neutron diffraction is not considered significantly different to the optical result of 9.2 Bohr magnetons.

5-3. Specific Heat Measurements.

The specific heat of a 5gm sample of $DyAlO_3$ was measured from $1.3 - 8^{\circ}K$. The most significant feature is a λ-anomaly peaked just above $3.5^{\circ}K$. The magnetic part of the specific heat is shown in Fig.5-1.

The high temperature part was analyzed in a similar fashion to $GdAlO_3$ into a T^3 lattice term and a

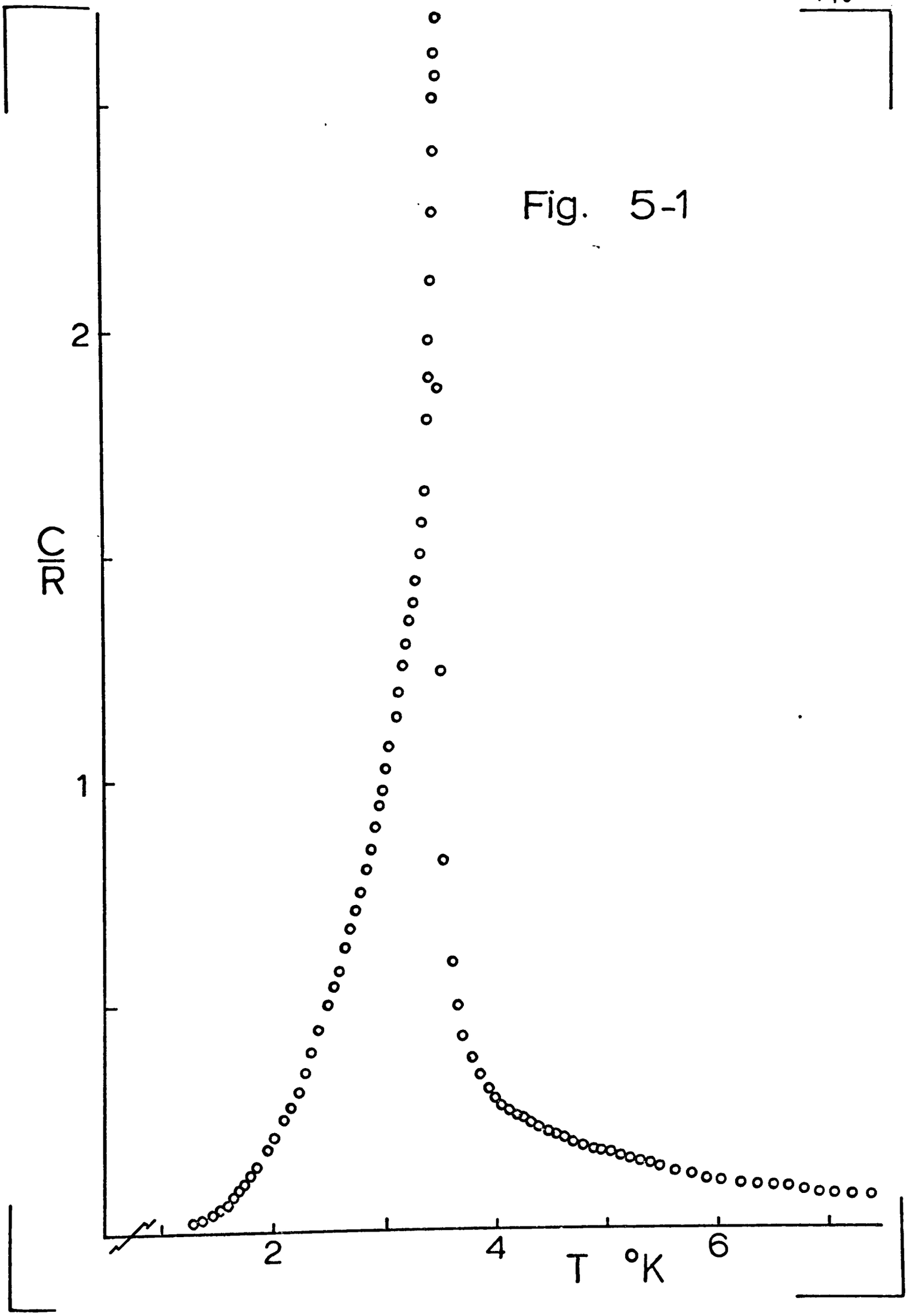


Fig. 5-1

$1/T^2$ tail of the λ-anomaly giving the result:

$$\frac{C}{R} = \frac{4.03}{T^2} + 3.25 \times 10^{-5} T^3$$

The lattice contribution has been subtracted from the experimental points to obtain Fig.5-1.

To obtain the true ordering temperature, a Mangelsdorf plot was carried out as described in Section 2-3. Once again only the points for $T < T_N$ fit a logarithmic singularity and may be validly used in a Mangelsdorf plot. The value obtained is $T_N = 3.53 \pm 0.01^{\circ}K$.

Using this value of T_N we can again find the nature of the singularity at the transition by plotting the specific heat against $|1 - T/T_N|$ on logarithmic and semi-logarithmic scales. Below the Néel temperature the best fit was obtained with

$$\frac{C}{R} = -0.50 \ln(1 - T/T_N)$$

and for $T > T_N$ the law obtained was:

$$\frac{C}{R} = 0.17|1 - T/T_N|^{-0.40} - 0.24$$

Thus as in the case of $GdAlO_3$ the singularity is logarithmic for $T < T_N$ and power law for $T > T_N$.

The theory of Eisele and Keffer[27] for anti-ferromagnets with a finite anisotropy gives the specific

heat for $T < T_N$ in terms of the Hankel functions K as:

$$\frac{C}{R} = \frac{1}{4\pi^2}\left(\frac{z}{2}\right)^{1.5} \frac{T_{AE}^{4}}{T_E^{3}} \frac{1}{T} \sum_n \left[K_2\left(\frac{nT_{AE}}{T}\right) + K_4\left(\frac{nT_{AE}}{T}\right)\right]$$

if we ignore the term including the temperature dependence of the energy gap T_{AE}. The term T_E is an effective exchange temperature but its true designation in a crystal where most of the ordering is due to magnetic dipole interactions is not obvious. Accordingly we shall treat it as an adjustable parameter.

The shape of the curve is determined entirely by T_{AE} with T_E acting only as a scaling factor. To obtain an estimate of T_{AE} we consider the asymptotic expansion of a Hankel function[56] as the argument $x \to \infty$ $(T \to 0)$:

$$K_\lambda(x) \sim \sqrt{\frac{\pi}{2x}} \exp(-x)\left[1 + \frac{4\lambda^2-1^2}{1!8x} + \frac{(4\lambda^2-1^2)(4\lambda^2-3^2)}{2!\,(8x)^2} + \ldots\right]$$

Thus at low temperatures we should have:

$$\frac{C}{R} \sim \frac{1}{\sqrt{T}} \exp\left(\frac{-T_{AE}}{T}\right)$$

From a plot of $\ln(C/T/R) \sim 1/T$ we obtained the value $T_{AE} = 7.65^{\circ}K$. This value was then inserted in the formula of Eisele and Keffer and the specific heat evaluated by computer using the tables of Hankel functions of Dempsey and Benson[57].

With a value for $T_E = 4.96^o$ the curve shown in Fig.5-2 was obtained. As can be seen the fit to the experimental points is astoundingly good, extending up to $0.94T_N$. We will consider later what significance may be attached to T_{AE} and T_E.

The energy and entropy values under the specific heat curve are given in Table 5-I together with the values for several theoretical models. The total entropy was measured to be 0.639R which is 8% lower than the expected value of R ln2. This shows that the ground state of Dy^{3+} at these temperatures is quite well described by an effective spin of $\frac{1}{2}$ but it is difficult to find an explanation for the shortage of entropy. The slight deficiency of dysprosium shown in the chemical analysis can only account for 1% and the experimental error is estimated at less than 2% which leaves over half the shortage unexplained.

The other energy and entropy values show that the best correlation is with the figures for the Ising simple cubic system. This is to be expected in view of the large anisotropy which we will find in the susceptibility and moment measurements. However the fact that all the $DyAlO_3$ values are consistently larger than the theoretical ones warns us that there is some interaction

TABLE 5-I

			$\frac{S_\infty - S_0}{k}$	$\frac{S_\infty - S_N}{k}$	$\frac{E_\infty - E_N}{kT_N}$	$\frac{E_\infty - E_0}{kT_N}$
$DyAlO_3$			0.639	0.160	0.285	0.745
Ising	s.c.	$S=\frac{1}{2}$	0.693	0.133	0.218	0.665
Ising	f.c.c.	$S=\frac{1}{2}$	0.693	0.102	0.150	0.613
Ising	sq.	$S=\frac{1}{2}$	0.693	0.387	0.623	0.881
Heisenberg	s.c.	$S=\frac{1}{2}$	0.693	0.265	0.595	0.894

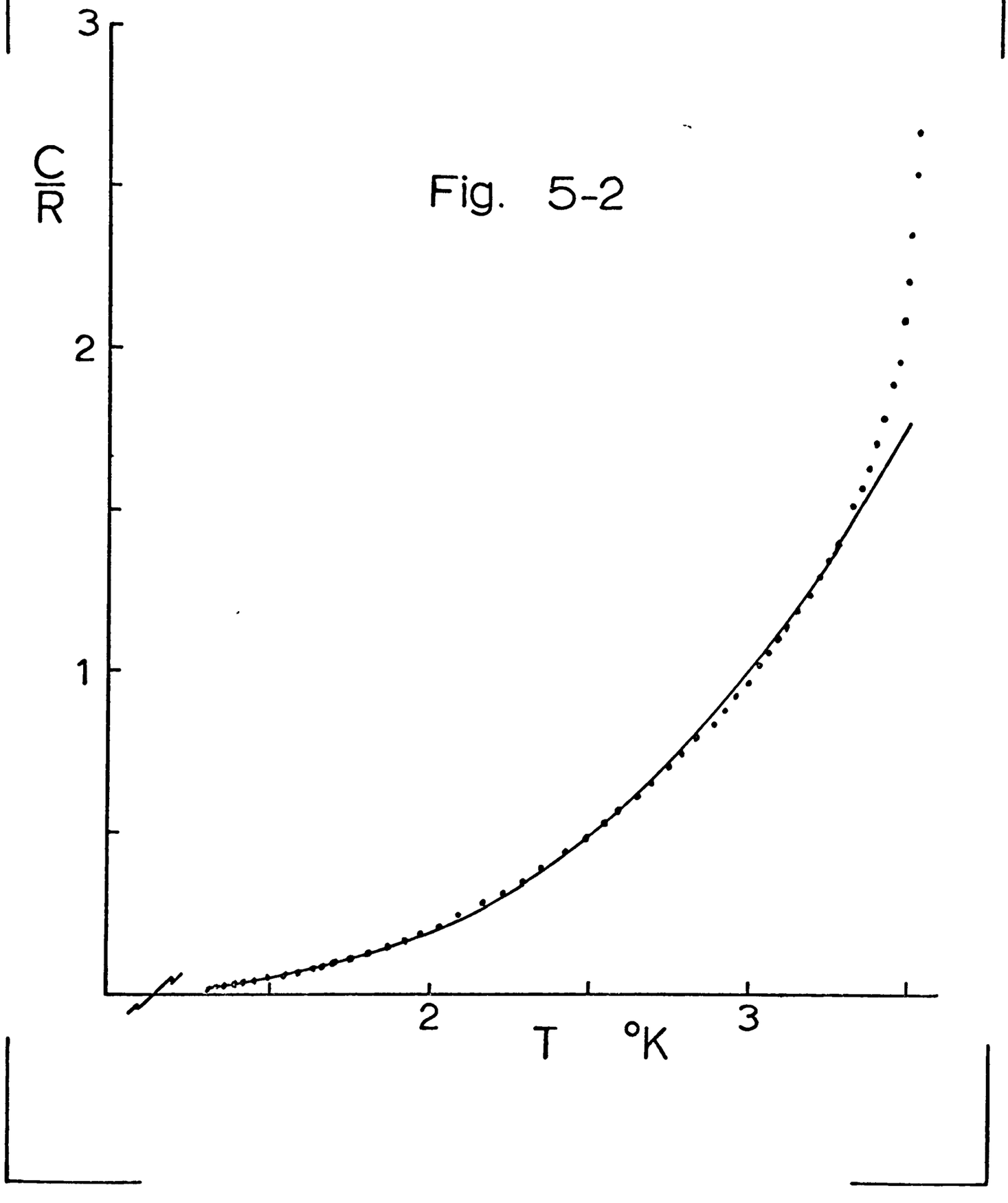


Fig. 5-2

tending to make the results closer to either the two dimensional Ising or the three dimensional Heisenberg models. If we consider the numerical values of the difference between the $DyAlO_3$ and Ising s.c. figures it is found that they correlate slightly better to the Heisenberg s.c. than to the Ising square net results.

However more will be said about the possible interactions in the next chapter when we have finished considering the experimental evidence.

5-4. Susceptibility Measurements.

Before detailing the experimental measurements let us first consider what kind of results we should expect. The system corresponds quite well to that of the Ising model so we shall use it for comparison.

In a two sublattice Ising antiferromagnet, measurement along a direction at an angle ϕ to the direction of the single g-value should give a Curie-Weiss law above the Néel temperature of the form:

$$\chi = \frac{C}{T + \theta} + \alpha$$

with the Curie constant, C having the value:

$$C = Ng^2\beta^2S(S+1)\cos^2\phi\,/3k.$$

Perpendicular to the g-value direction the temperature

dependent part will be zero.

However in $DyAlO_3$ we have four sublattices instead of two, with a hidden canting of $\pm 33^\circ$ to the b-axis in the a-b plane. If we measure the susceptibility along the a- or b-axes then all four sublattices are equivalent and we should obtain Curie constants $Ng^2\beta^2S(S+1)\sin^2 33^\circ/3k$ and $Ng^2\beta^2S(S+1)\cos^2 33^\circ/3k$ respectively. Along the c-axis the susceptibility should still be small and temperature independent.

Below the Néel temperature the susceptibility along both the a- and b-axes should fall with decreasing temperature while maintaining a ratio of $\tan^2 33^\circ$. Along the c-axis there should again be no change in the susceptibility.

The susceptibility and moment measurements were carried out on the 78mgm single crystal described in Section 1-4. The results given have been corrected for demagnetizing factor to the value appropriate for a sphere.

As expected from the preceding discussion the hydrogen range susceptibility results show very large anisotropy. Unfortunately the measured temperature range was not sufficiently large to obtain a value for the Van Vleck temperature independent part of the susceptibility

and the results have therefore simply been analyzed into a Curie-Weiss law.

For the a- and b-axes we obtained the results:

$$\chi_a = \frac{11.2}{T + 6.7}$$

$$\chi_b = \frac{22.8}{T + 4.6}$$

The Curie constants agree reasonably well with the values expected from the g-values, the theoretical numbers being $C_a = 10.1$, $C_b = 22.6$. The discrepancy can be easily explained by our failure to determine a value for the temperature independent term which must be significant at these temperatures. We will consider the Weiss θ values later when discussing the magnitude of the internal interactions.

Along the c-axis the susceptibility has a very small value, $\chi_c \sim 0.17$, the majority of which is due to the temperature independent term. Because of this it was not possible to estimate a Weiss θ value, but from comparison with the helium range measurements the Curie constant was estimated to be 0.23 ± 0.10 corresponding to a g-value of 1.6 ± 0.4 in good agreement with the optical measurements.

The helium range measurements are shown in

Fig.5-3. The susceptibilities along both the a- and b-axes decrease below the Néel temperature and the value obtained for T_N agrees well with that from the specific heat measurements.

At the very lowest temperatures χ_b crosses over χ_a before they reach their temperature independent values of $\chi_b = 0.030$ and $\chi_a = 0.050$emu/Oe. Although the correction for the specimen holder is 0.01emu/Oe at this temperature, it is the same for both measurements and so does not affect the crossover.

To find the explanation for this effect we must consider the concept of the perpendicular susceptibility in this highly anisotropic material. In the case of $GdAlO_3$ we saw that the perpendicular susceptibility remained almost constant with decreasing temperature at the value it attained at T_N. The same should also be true here except there is greater difficulty in determining the part of the susceptibility perpendicular to the ordering direction since we have two effective ordering directions due to the canting.

If we just consider one pair of antiparallel sublattices and apply a small magnetic field perpendicular to their axis in the a-b plane, then the susceptibility we obtain is due entirely to g_β. The component of this

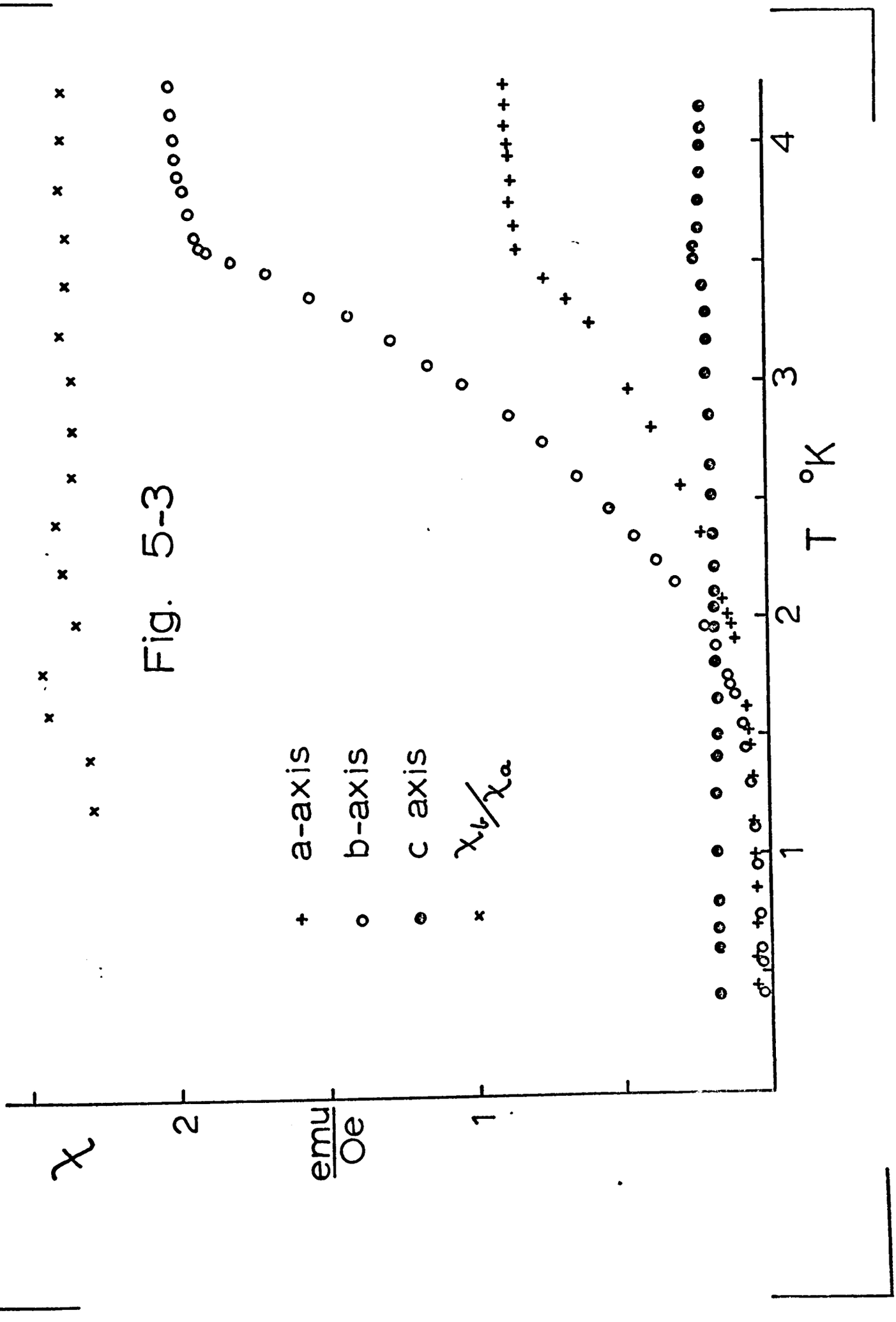


Fig. 5-3

which we measure along the a-axis is $\chi_\perp \cos^2 33^\circ$ and along the b-axis is $\chi_\perp \sin^2 33^\circ$.

We may obtain an estimate of the value of $\chi_\perp$ by taking the molecular field theory formulae for T_N and $\chi(T_N)$ given by Smart[46] and eliminating the dependence on the interaction between them we then obtain the simple formula:

$$\chi(T_N) = \frac{C}{2T_N}$$

Inserting the g-value g_β into the formula for the Curie constant C and putting $\chi_\perp = \chi(T_N)$, we obtain the values:

$$\chi_a = 0.096 \text{ emu/Oe}$$
$$\chi_b = 0.041 \text{ emu/Oe.}$$

These values agree well with the measured values considering the approximate nature of the calculation and tha small size of the quantities involved.

If we subtract the temperature independent values from the results, then as mentioned at the start of this section $\arctan (\chi_b/\chi_a)^{\frac{1}{2}}$ should be equal to the canting angle. The ratio χ_b/χ_a is given as a function of temperature by the crosses in Fig.5-3. The ratio is seen to remain constant within the experimental error showing that the canting angle does not change with

temperature. The average value of 2.37 ± 0.02 corresponds to a canting angle of $33.0^{o} \pm 0.2^{o}$ which is in good agreement with the neutron diffraction results of Bidaux and Meriel.

5-5. Moment Measurements.

Because of the large anisotropy in $DyAlO_3$, application of a strong magnetic field does not induce a "flop" as in $GdAlO_3$, but a "flip" in which one or more sublattices simply reverse their direction of magnetization.

If we consider a pure Ising system where each individual moment is constrained to lie in a line but may point in either direction along it, then below the ordering temperature there will be an internal field at each site preferring one direction or the other. If an external field is then applied along this constraining direction when it increases past the value of the internal field then all the moments which were originally antiparallel to the field will now find it energetically more favourable to "flip" over and become parallel to it.

This means that the full saturation moment would be obtained immediately on passing through the critical field, in contrast to a flop when only a small fraction is obtained by the discontinuous process.

In $DyAlO_3$ we do not quite have this simple Ising situation which would correspond to $g_\beta = g_c = 0$. The quite finite value of g_β means that when a field is applied at an arbitrary angle in the a-b plane then the moments will turn towards it, finding an equilibrium angle between the resultant field direction and the α-axis.

However even with this complication, a simple flip would be obtained if we applied the external field along the α-axis. But here because of the canting, we can at best apply the field along the α-axis of two of the four sublattices, at which stage it will be at an angle of 66° to the α-axis of the other two sublattices.

The simplest experimental result we can obtain therefore is when the applied field is parallel to the a- or b-axes, in which case allfour sublattices are equivalent. Fig.5-4 shows the results obtained at $0.5^\circ K$ when the field is applied along the b-axis and it can be seen that the moment rises steeply and smoothly when the applied field exceeds 6.3kOe.

In contrast the second curve in Fig.5-4 shows the magnetic moment obtained when it was attempted to apply an external field parallel to the a-axis. A stepped double flip has been obtained showing that the correct

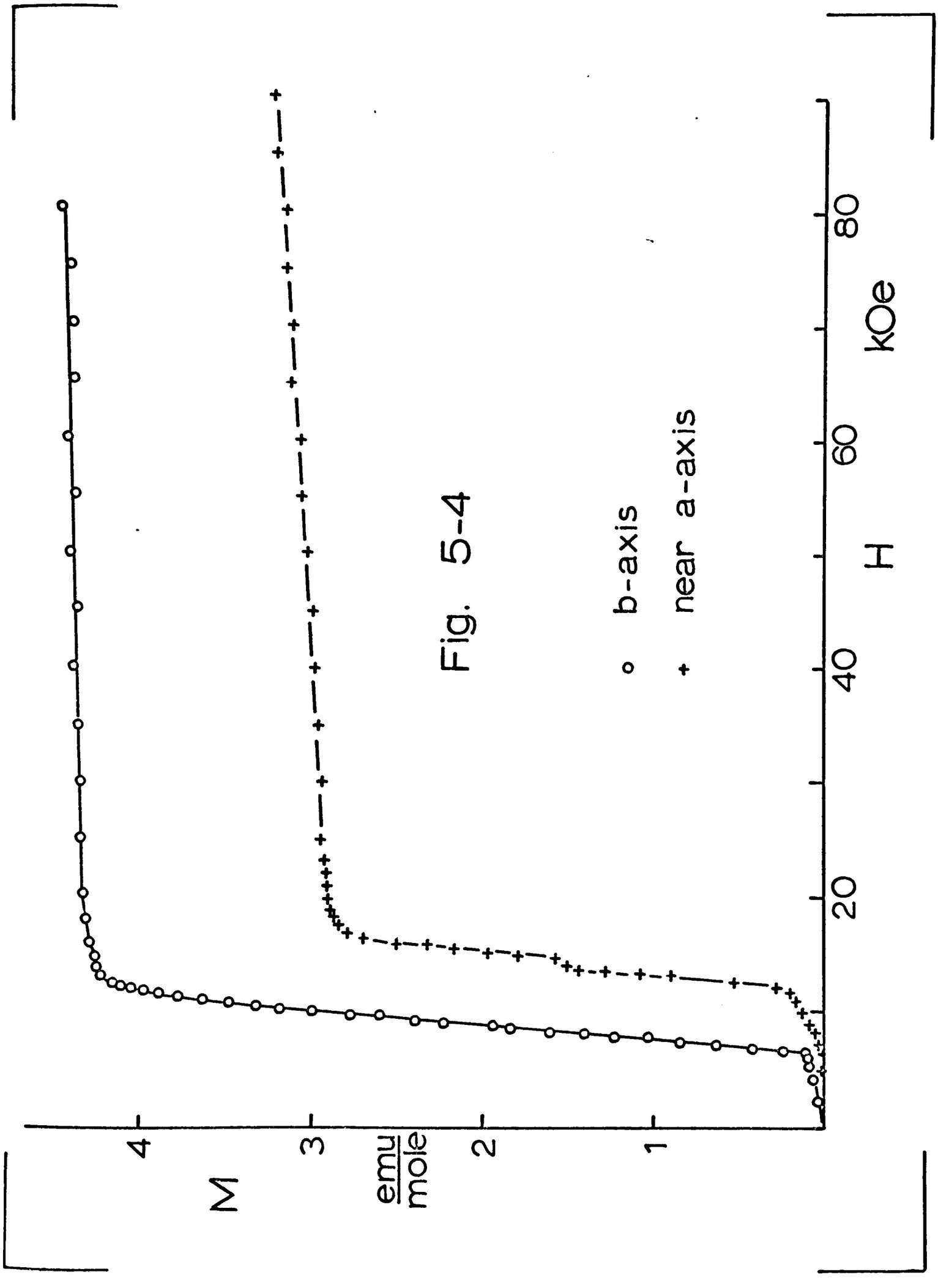


Fig. 5-4

alignment was not achieved and so the four sublattices are no longer equivalent. The process is shown schematically in Fig.5-5 as first one and then a second sublattice reverse their directions of magnetization.

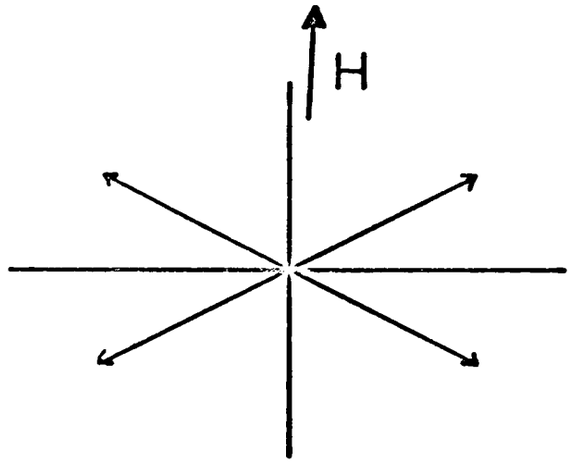
It is interesting to estimate how far from the a-axis the applied field was in order to obtain this pronounced double flip. If we take the applied fields for the two flips as 11.7kOe and 12.8kOe respectively, then the angle δ from the a-axis is simply:

$$\frac{\cos(57-\delta)}{\cos(57+\delta)} = \frac{12.8}{11.7}$$

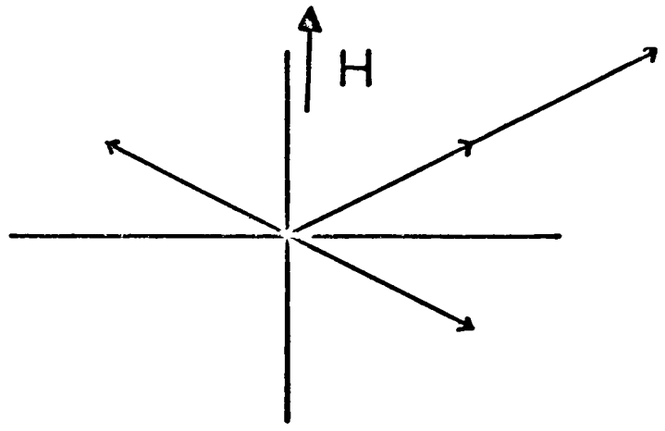
This gives the solution $\delta = 1.6^{\circ}$, a surprisingly small angle, showing how critically the observation of an unstepped double flip depends on the accurate orientation of the crystal.

No demagnetization correction has been made to these results and the demagnetizing factor is therefore the experimental value appropriate for a sphere.

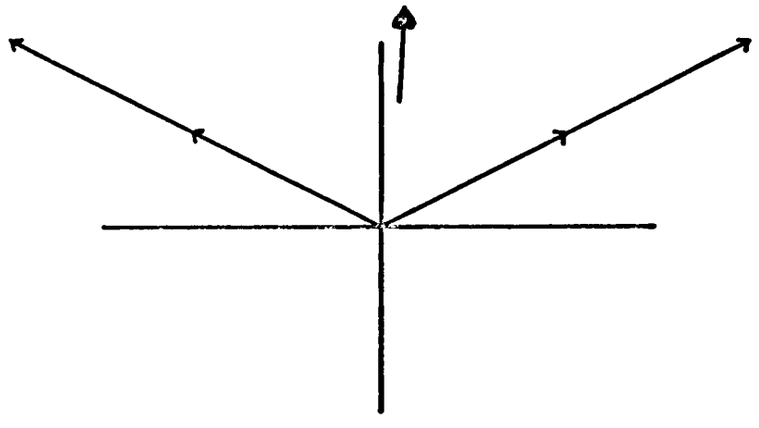
In both the results in Fig.5-4 there is a small rise in moment above the flip with increasing applied field, showing that saturation has not yet been achieved. This is because the Dy^{3+} ion is not a perfect Ising system and the finite value of g_{β} is allowing the net magnetization of each sublattice to turn nearer to the



$H < H_C$



Flip 1



Flip 2

Fig. 5-5

applied field. More will be said quantitatively about this in the next chapter.

The absolute value of the moment is also greatly different for these two directions due to the angle of the maximum g-value being nearer to the b-axis.

For arbitrary angles of the applied field in the a-b plane not close to the orthorhombic axes, the second flip appears to be no longer a sharp process, the moment rising steadily with field above the first flip.

Fig.5-6 shows examples of this effect at five different angles in the a-b plane. In some cases e.g. the measurement at 33° to the b-axis, the second "flip" or "pseudo-flip" as we could call it commences directly at the top of the first flip. However for angles nearly perpendicular to the second sublattice (45° and 69°) there is a very slowly rising part of the moment curve before the steeper part where the pseudo-flip takes place. Consideration of these effects in terms of the internal fields and demagnetization corrections will be given in the next chapter. In all the measurements the moment was still increasing at 90kOe applied field.

The induced moment along the c-axis at 0.5°K in large applied field is shown in Fig.5-7. The slope of

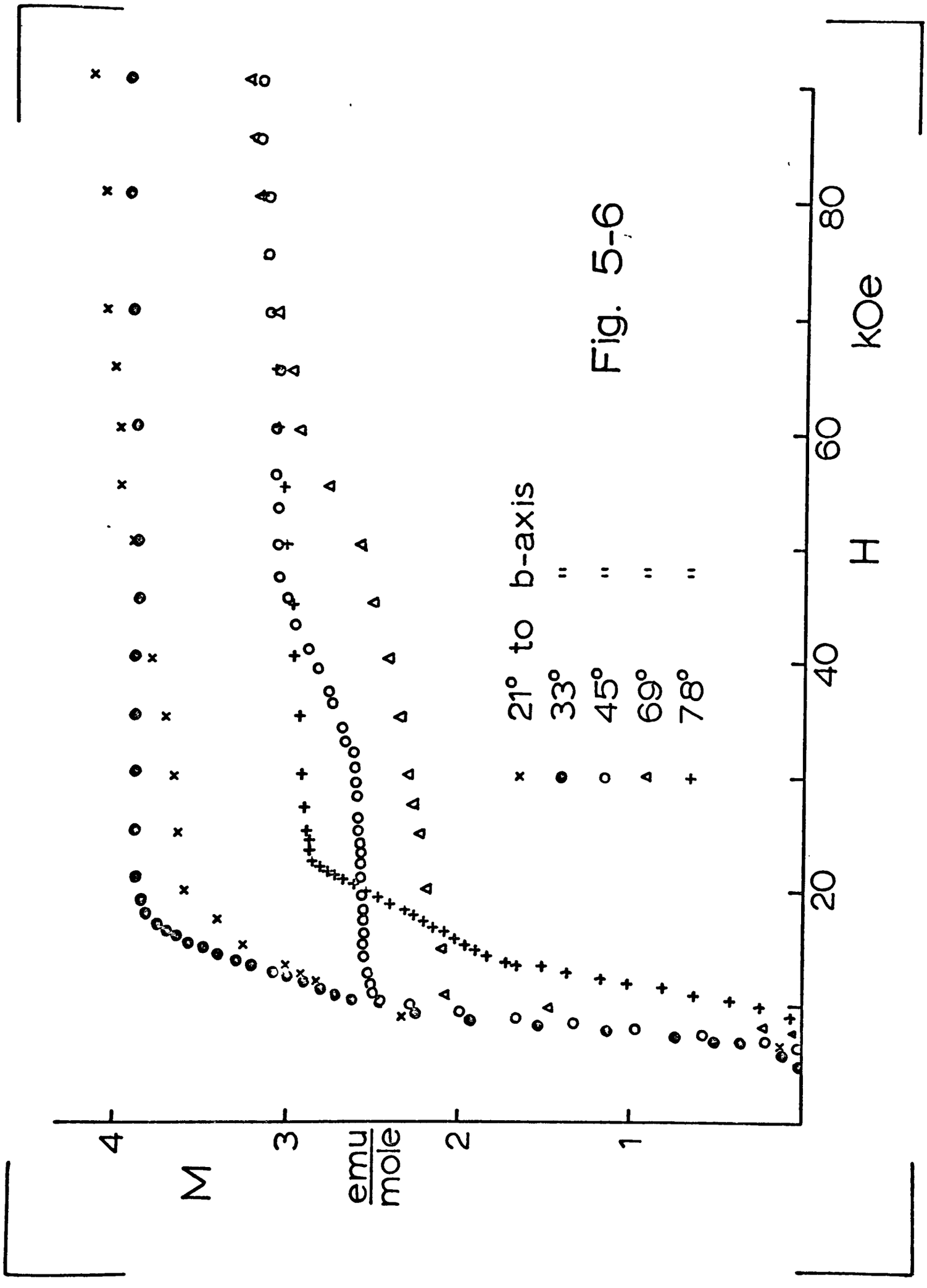


Fig. 5-6

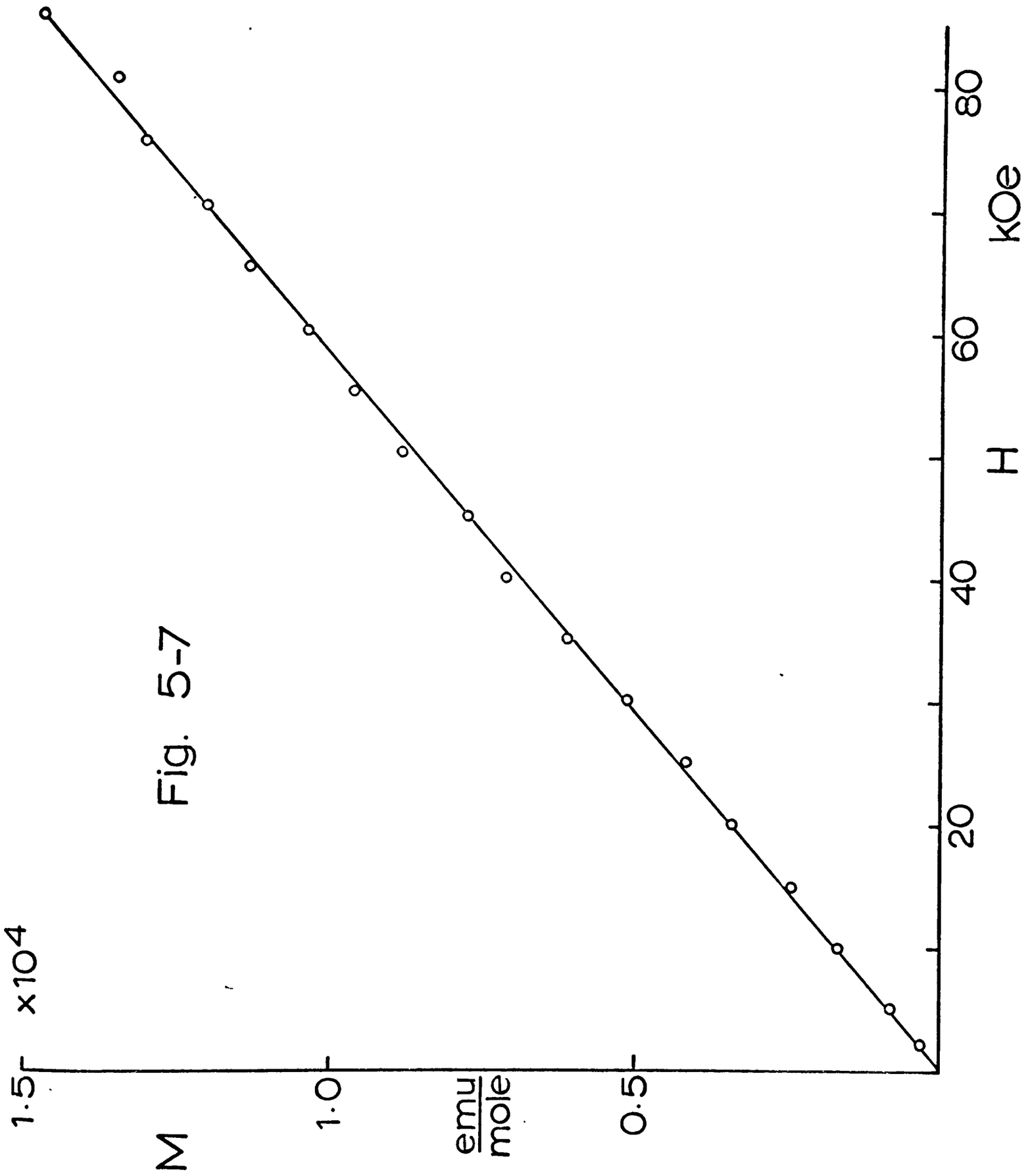


Fig. 5-7

0.176emu/Oe is independent of field and agrees well with the value of the low field susceptibility 0.180emu/Oe. A similar curve of slightly larger slope is obtained at 4.2°K.

It is interesting that only a small part of this moment is due to the ground state g-value of 1.7, the majority being due to admixing of higher states through the Van Vleck temperature independent term. In fact the saturation moment for a g-value of 1.7 and spin of $\frac{1}{2}$ is only 4700emu/mole, 30% of the observed moment at 85kOe. However no change of slope due to saturation of this g-value was observed.

5-6. Summary.

A survey of other experimental results on $DyAlO_3$ shows that both the canting angle and the direction of the maximum g-value are at 33° to the b-axis in the a-b plane.

Specific heat results showed that the best estimate for the Néel temperature is 3.53°K and that at these temperatures the Dy^{3+} ions are in a ground doublet state.

The susceptibility results were consistent

with those expected for a canted antiferromagnet with a canting angle of 33^{o} and the estimates of the g-values agreed reasonably well with those from optical measurements.

The moment measurements showed the phenomenon of "spin flip" expected in an anisotropic antiferromagnet. A double spin-flip is observed near the orthorhombic axes, but at an arbitrary angle in the a-b plane the second spin flip appears to become a gradual instead of a discontinuous process.

CHAPTER SIX

DYSPROSIUM ALUMINATE - ANALYSIS OF RESULTS.

6-1. Introduction.

This chapter will be concerned entirely with the various internal interactions in dysprosium aluminate and their effect on our experimental results.

Using the g-values obtained from optical measurements we will calculate the dipole contribution to our various experiments and then consider which forms of exchange we need to explain discrepancies.

An analysis of the internal configuration in the moment experiments as a function of field will be given and it will be shown that these are consistent with the g-values of Hufner et al[54]. Finally an estimate of the size of the exchange parameters will be given.

6-2. Consideration of Interactions.

It has already been calculated by Bidaux and Meriel[43] that about 70% of the energy of ordering in $DyAlO_3$ is due to the dipole-dipole interaction. However as their analysis was made on the basis of an axial

magnetic moment with a single g-value of 17.6 at 33^{o} to the b-axis, it is necessary for us to repeat the calculation using the g-values obtained by Hufner et al[54]. In particular, his determination of the size of the other g-value in the a-b plane has important consequences for us in the analysis of the moment experiments.

If we include the various combinations of single and double flips, there are nine configurations with the sublattices along the 33^{o} directions for which we must work out the dipole fields. These are shown schematically in terms of the moment directions in Fig.6-1 and we shall consider in each case the resultant field on sublattice 1.

In fact many of these configurations may be broken up into two if we consider the distinction between the two G_xA_y modes of Bidaux and Meriel mentioned in Appendix 1. However we shall neglect this distinction since the difference in the dipole interaction is small and use only the configuration which they favoured.

A tabulation of the results for each of the configurations of Fig.6-1 is given in Table 6-I. We have listed the total dipole field magnitude and direction taking the positive b-axis as the origin of the direction

TABLE 6-I

Dipole Fields in $DyAlO_3$.

Configuration	Field (kOe)	Angle	Component (kOe)
1	6.75	1.0°	+5.72
2	3.74	299.8°	-0.21
3	3.56	70.3°	+2.84
4	5.16	12.3°	+4.81
5	5.48	349.9°	-4.01
6	2.27	273.8°	-1.11
7	3.69	180.3°	-3.10
8	2.27	93.8°	-1.11
9	3.69	0.3°	-3.10

\+ indicates a favourable field.

\- indicates an unfavourable field.

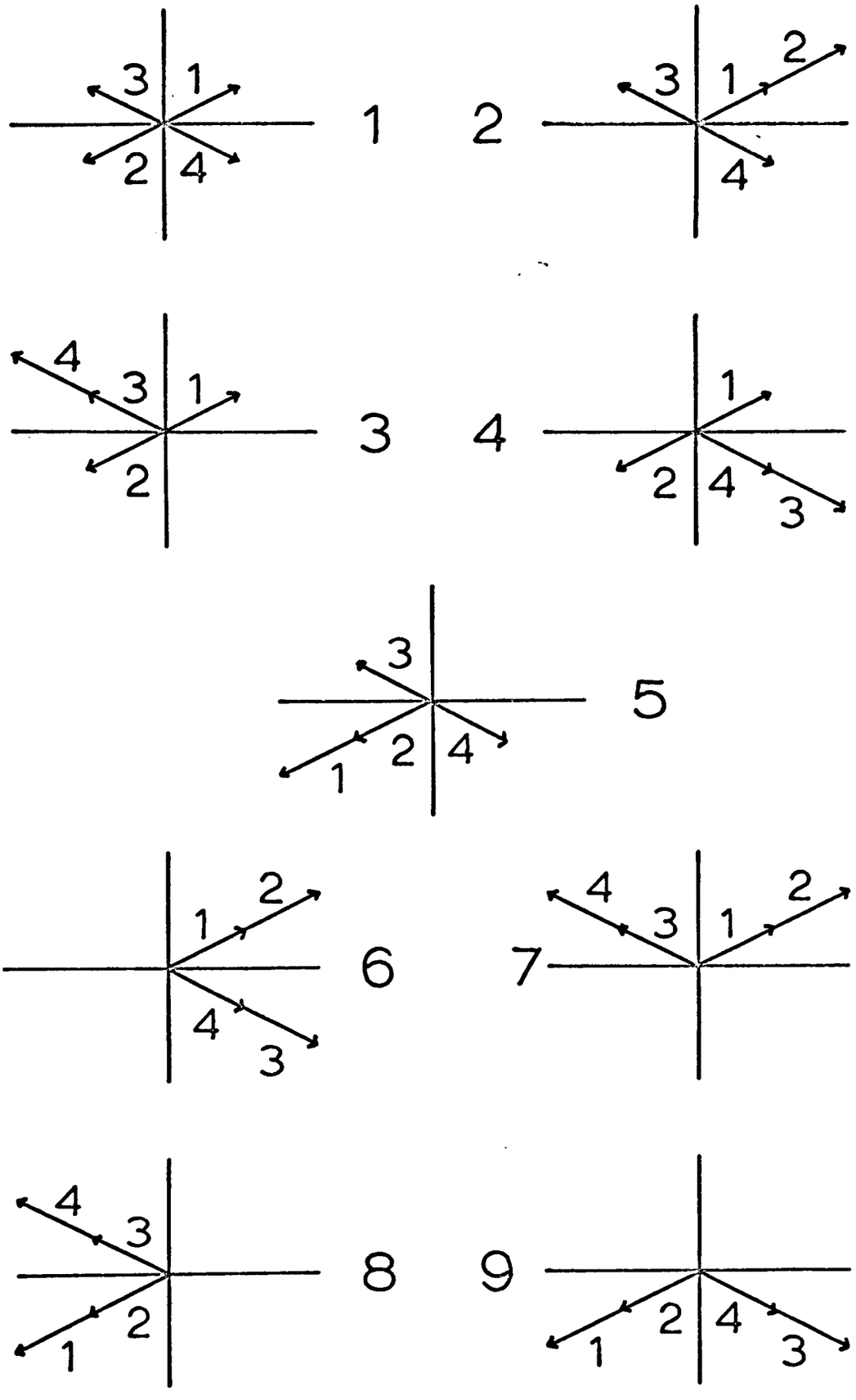


Fig. 6-1

scale. Also listed is the dipole field component along the positive direction of sublattice 1, e.g. in configuration 5 there is a component of the dipole field trying to flip sublattice 1 back to its original position.

It can be seen from Table 6-I that configuration 1 which is the observed G_xA_y mode has the largest favourable dipole field as expected. If we convert this field into an effective ordering temperature using the simple molecular field relation $g_\alpha \beta H = kT_N$ we obtain $T_N(\text{dip}) = 3.53^\circ K$.

This is unfortunately exactly equal to the observed Néel temperature, but overestimation of the dipole contribution has been observed before, e.g. in dysprosium aluminium garnet[63] when again the entire ordering temperature could be accounted for by dipole interactions. However in this case there was an exchange contribution of about 30% as was shown by optical measurements and a Monte Carlo calculation of the specific heat.

It will also be seen from Table 6-I that the effective dipole field points almost along the b-axis, a not surprising result since we noticed in $GdAlO_3$ that the dipole field for a G mode is very small.

The question now arises as to why the sublattices happen to point along the direction 33° from the b-axis as observed by neutron diffraction. The fact that this is the direction of maximum g-value is not sufficient, since the finite value of g_β would mean that the sublattices would lie between this direction and the resultant dipole field direction of 1° from the b-axis. The angular deviation from the α-axis is given by:

$$\tan \delta = \frac{g_\beta}{g_\alpha} \tan 32^\circ.$$

This gives the solution $\delta = 6^\circ$, i.e. we would expect a canting angle of $\pm 27^\circ$ from the b-axis.

If we now introduce the possibility of an exchange interaction as well it is clear that we must consider two types, one between nearest neighbours above and below along the c-axis and one between the four nearest neighbours in the a-b plane. We shall denote these by J_2 and J_1 respectively.

Now the interaction J_2 is between magnetically equivalent ions which are constrained on symmetry grounds to lie antiparallel (or parallel) to one another.

In his optical absorption experiments Hufner[54] has observed a triplet splitting at 4.2°K and 20.4°K

which he attributed to an Ising exchange interaction between these ions. He obtained the value

$$J_2 = -1.2^{o}K$$

for the interaction.

However as long as the direction of the Ising interaction is along the principal g-value direction, as is most likely, this interaction can not bring the resultant field direction around from the b-axis to 33^{o} to the b-axis (unless $J_2 \rightarrow \infty$).

On this basis it would seem that we need a small antiferromagnetic exchange interaction J_1 to explain why the moments point along the direction of maximum g-value.

We are therefore allowing exchange interactions between ions 1 - 4 (J_1) and ions 1 - 2 (J_2) but will assume that there is no exchange interaction between the next nearest neighbour ions 1 - 3. A diagram of these interactions is shown schematically in Fig.6-2.

6-3. Analysis of Moment Experiments.

We have two main points to explain from the moment experiments detailed in Section 5-5. The first is the variation in the spin flip critical field with

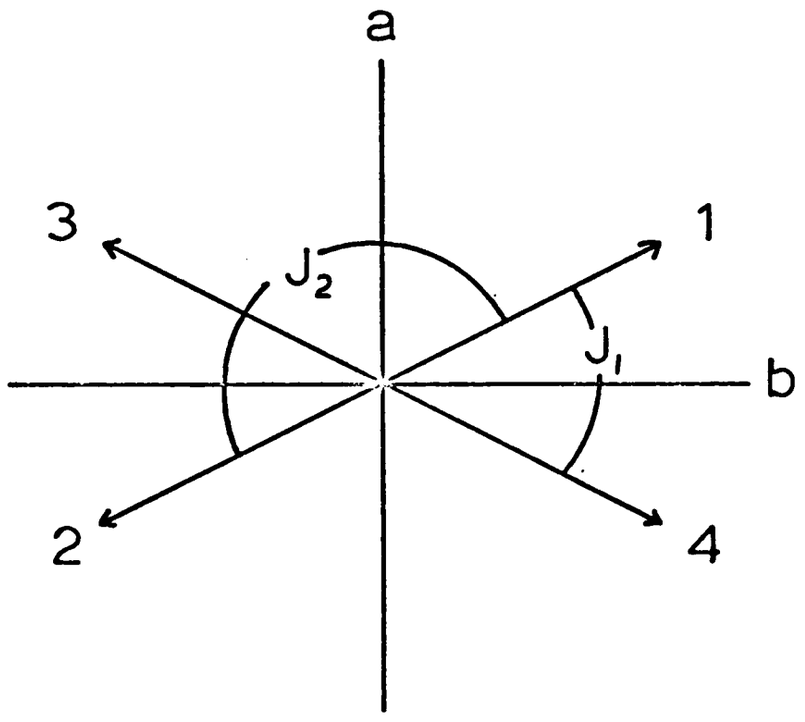


Fig. 6-2

angle for both the first and second flips and the second is the direction of the resultant sublattice magnetizations as a function of field including why a sharp second flip is only obtained near the orthorhombic a- and b-axes.

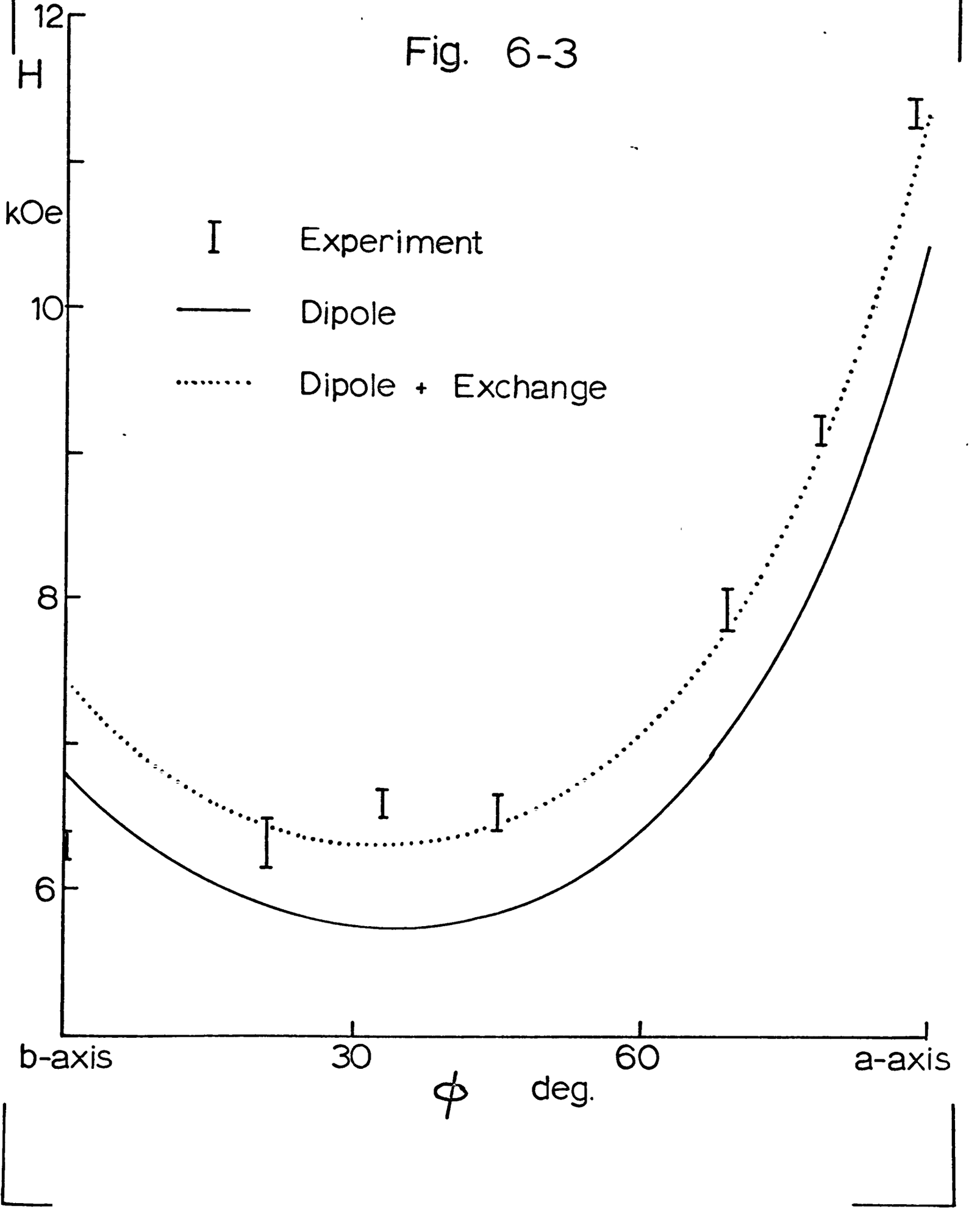
In view of the inconclusive evidence as to the size and nature of the non-dipolar interactions it was thought advantagous to calculate the critical fields expected for the first flip on the basis of dipole forces alone.

This was done by simply writing down expressions for the energies in the flipped and unflipped states and equating them to solve for the applied field. The theoretical results are shown as the solid curve in Fig.6-3 together with the experimentally determined values.

For the measurements not taken close to the a- or b-axis the theoretical curve underestimates the flipping field by an almost steady 1.0kOe which we may attribute to the exchange interaction. However the basic details of the experimental results are quite well explained on the basis of dipole forces alone except for the measurement along the b-axis which is lower than the predicted value.

Before considering the possible reasons for

Fig. 6-3


12
H
kOe
10
8
6
Experiment
Dipole
Dipole + Exchange
b-axis
30
60
a-axis
φ deg.

this discrepancy in terms of exchange let us see what other correlations may be made.

In view of the finite value of g_β it is of interest to see how well the flips correspond to a simple reversal of magnetization direction ("simple flip") or whether there is also an associated turning towards the direction of the applied field.

A list of values is given in Table 6-II for the observed moment after one and two flips compared with the values expected for a simple flip and also for the saturation moment attainable at the angle of measurement.

The saturation values quoted are the maximum moments obtainable along the given directions. This is because the conventional saturation description of having the sublattices parallel to the applied field is not in general possible, even for infinite applied field. In fact for the applied field at an angle ϕ to the α-axis, the maximum angle θ that the sublattices can turn away from the α-axis is given by:

$$\tan \theta = \frac{g_\beta}{g_\alpha} \tan \phi.$$

As expected the correlation in Table 6-II is much better for the case of the simple flip. The worst

TABLE 6-II

	1 FLIP			2 FLIPS		
Angle to b-axis	M(obs)	M(33°)	M(sat)	M(obs)	M(33°)	M(sat)
0°	-	-	-	43300	43000	45500
21°	22400	25100	25300	-	40200	44000
33°	25300	25700	25700	38500	36300	42700
45°	25400	25100	25300	31000	30400	40700
69°	20500	20600	22300	29700	26000	37800
78°	18100	17600	20700	28800	27600	37400
88°	15000	14000	18400	29000	27900	36600

correlation is by the 21° measurement which is considerably less than either of the theoretical estimates. This may be explained by the fact that this measurement (and the 69° measurement) was taken before the specimen was ground to a sphere. The specimen was then elongated along the pseudo-cubic axis and the different demagnetizing fields could account for the reduction in moment.

The second half of the table shows that the second flip is also close to a simple reversal of the magnetization. Above the second flip we still observe a moment increasing with field and Table 6-III compares the experimental moment values at 90kOe applied field with the saturation values and the simple double flip values. As can be seen, considerably greater applied fields are necessary before saturation can be achieved.

The variation of the second flip with the angle of the applied field can be treated in a similar method to that used to treat flip 1, i.e. by solving the energy equation for the two states for the applied field as a function of angle.

The dipole fields on each sublattice after one flip are shown in Fig.6-4 with the applied field being at an arbitrary angle ϕ in the first quadrant. We can see that for $\phi < 57^{\circ}$ the second flip will be a reversal of

TABLE 6-III

Angle to b-axis	M(90kOe)	M(33°)	M(sat)
0°	44400	43000	45500
21°	41700	40200	44000
33°	39200	36300	42700
45°	33800	30400	40700
69°	32800	26000	37800
78°	32000	27600	37400
88°	32000	27900	36600

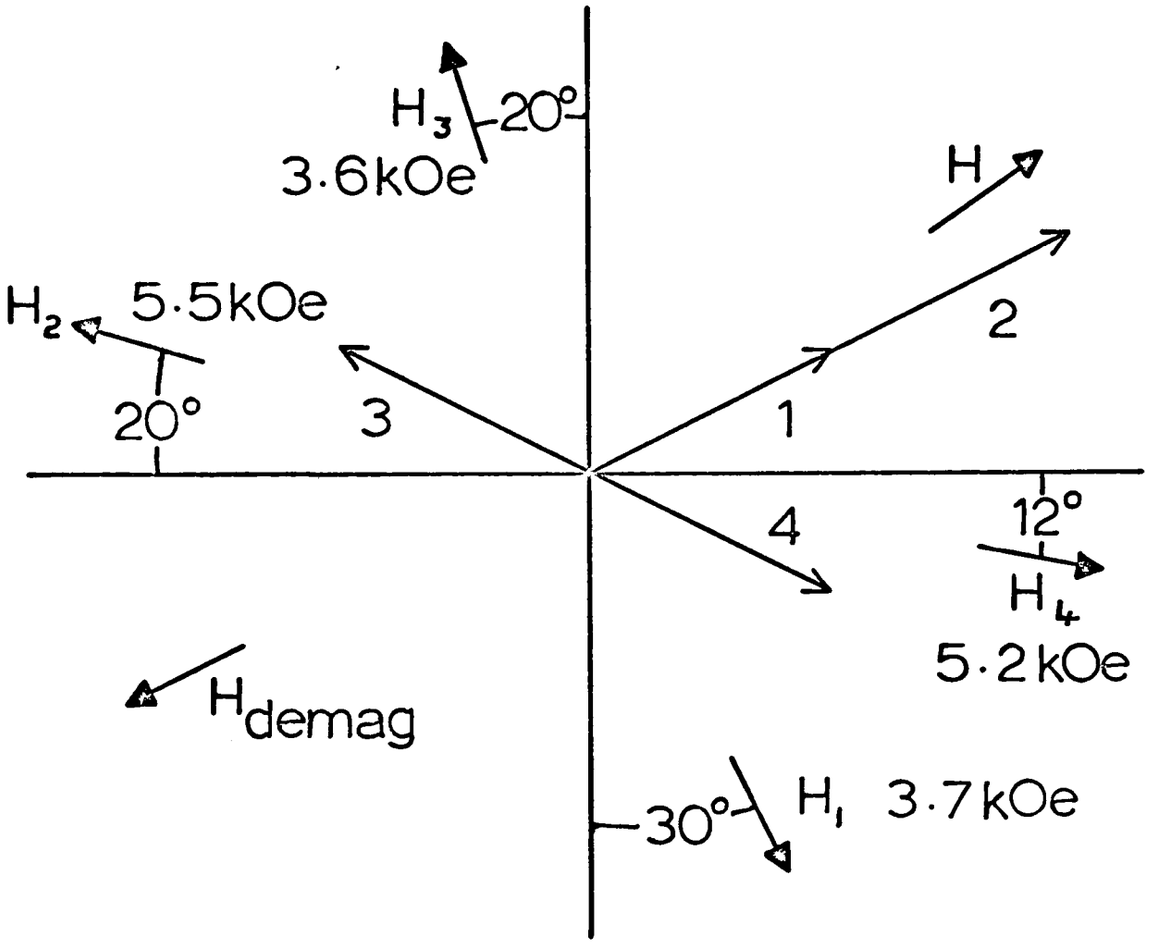


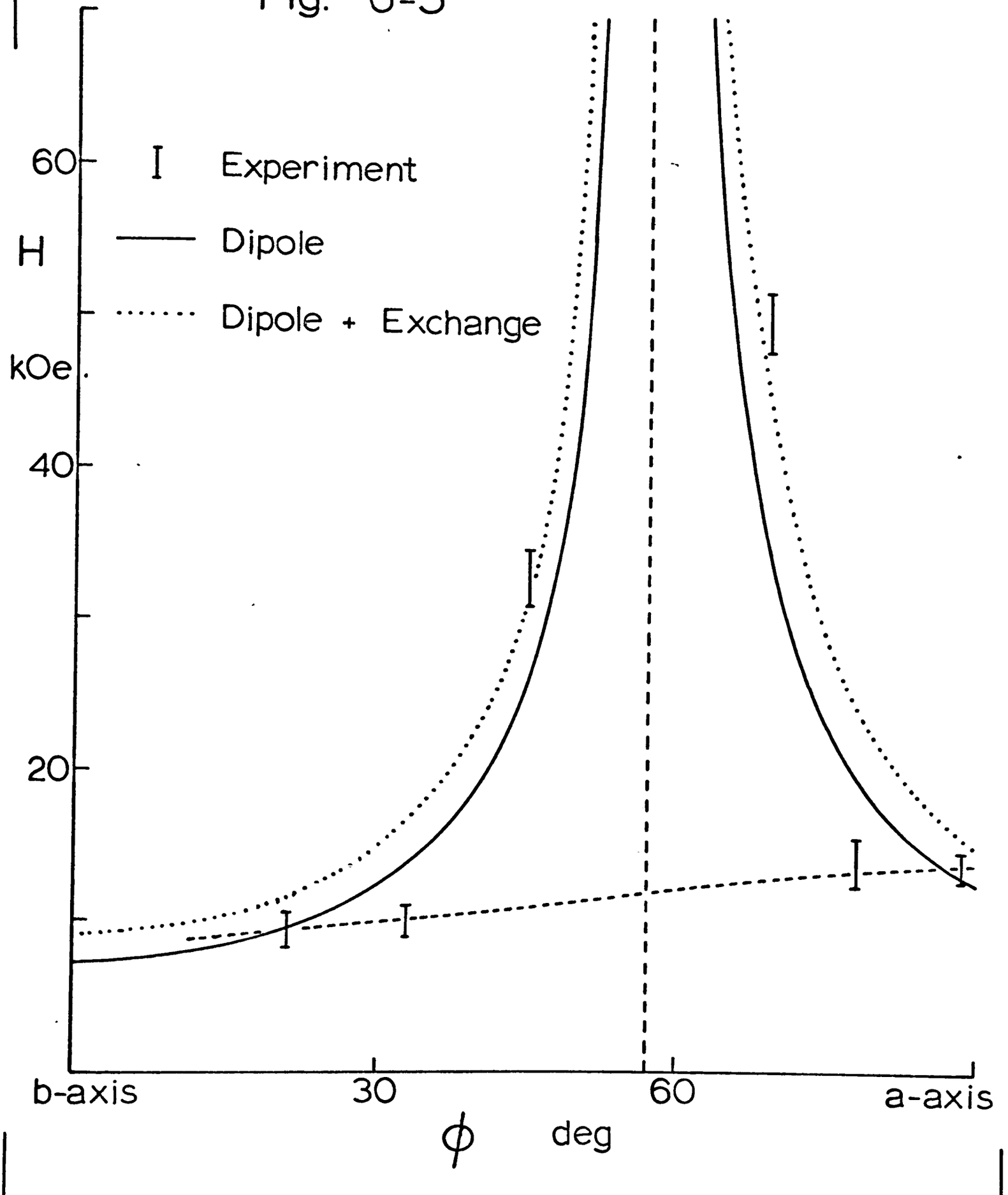
Fig. 6-4

sublattice 3 whereas for $\phi > 57^{\circ}$ sublattice 4 will be reversed. Since clearly no second flip can be obtained for $\phi = 57^{\circ}$, this angle is an asymptote, with the applied field value varying as $1/\sin(57-\phi)$ in this approximation.

There is however another detail which we have so far neglected - the demagnetizing field of sublattices 1 and 2 after the first flip. This amounts to a constant opposing field of about 1.4kOe. The theoretical variation of the second flipping field is shown in Fig.6-5 together with the experimental points. The agreement is seen to be reasonable, particularly in view of the enormous error produced by a few degrees misalignment for angles near 57°.

The reason for the low experimental values at 33° and 78° can be attributed to the fact this is very close to the applied field at the top of the first flip and it is extremely difficult to pick out unambiguously the field at which the second flip begins. For comparison the applied field at completion of the first flip is shown as the dotted curve in Fig.6-5. It is thus easy to see now why we obtained a pronounced two step process as in the 45° curve in Fig.5-8 but a continuous process with two different slopes as in the 33° curve.

Fig. 6-5


60
H
kOe
40
20
I Experiment
Dipole
Dipole + Exchange
b-axis
30
60
a-axis
φ deg

If we consider the internal field seen by sublattices 3 and 4 we can explain the different slope of the second flip which makes it appear a gradual process. In Fig.5-8 we have plotted the magnetic moment against applied field, rather than internal field as for $GdAlO_3$, because the internal field seen by the two sets of sublattices is different. In particular the field seen by sublattices 3 and 4 is $H\cos(33+\phi)$ and similarly the moment which we measure is $M\cos(33+\phi)$.

To consider a case quantitatively let us take the 45° measurement. The slope of the second flip appears to correspond to the impossible demagnetizing factor $N/4\pi = 7.84$. However when we consider the components of M and H we must reduce this by $\cos^2 78^\circ$ giving the demagnetizing factor $N/4\pi = 0.31$ in good agreement with the value 0.33 expected for a sphere.

Thus all the major features of the moment curves have been explained reasonably well by using dipole forces alone, helping to show that this is indeed the dominant interaction.

6-4. The Exchange Interactions.

In trying to estimate the importance of the two nearest neighbour exchange interactions described in

Section 6-2, we have so far neglected one very great complication - we do not know how these interactions will vary with angle. In the case of the J_2 interaction between magnetically equivalent atons along the c-axis it seems reasonable to assume that the interaction is closely represented by an Ising form.

However the interaction J_1 between neighbours in the a-b plane is between moments normally canted at 66° to one another and it seems probable that this interaction has a complicated angular dependence.

With this in mind we only have sufficient information to try and estimate the interactions in the particular case where the moments lie parallel or antiparallel to the crystal field α-axis at 33° to the orthorhombic b-axis.

The specific heat measurements are the most lucrative in providing information for our cause, there being four values which depend on the interactions. These are the total energy under the magnetic part of the specific heat, the energy gap T_{AE}, the $1/T^2$ part of the specific heat tail and the low temperature expansion.

If we subtract the dipole contribution to the total energy, $\frac{1}{2}Ng\beta SH_{dip}\cos 33^\circ$, from the total energy

2.62R we obtain the equation:

$$2\frac{J_1}{k} - \frac{J_2}{k} = 1.70^{\circ}$$

We have maintained the convention that $J < 0$ corresponds to an antiferromagnetic interaction and therefore the opposing sign of the two interactions arises because J_2 is aiding the G_xA_y ordering but J_1 is hindering it as can be seen from Fig.6-2.

The low temperature expansion of the specific heat should be of the form(66:

$$\frac{C}{R} = \frac{A}{T^2}\exp\left(-\frac{\delta}{T}\right)$$

where δ is equal to twice the sum of the interactions. Graphically we obtain the result $\delta = 10.55^{\circ}K$ from which we must subtract the dipole contribution determined in Section 6-2. This gives us an equation similar to the previous one:

$$2\frac{J_1}{k} - \frac{J_2}{k} = 0.88^{\circ}K$$

In an antiferromagnet with small anisotropy T_{AE} corresponds to the flopping field. However in an antiferromagnet with large anisotropy there is no spin flop and it therefore corresponds to twice the minimum flipping field. The factor of two arises because in turning over

one spin its total energy change is from $-g\beta H_c$ to $+g\beta H_c$. If we take the spin flip field as 6.3kOe this gives an expected value of 7.8°K for T_{AE} which agrees well with the observed value of 7.65°K.

However to obtain another equation containing the exchange explicitly we must turn to the $1/T^2$ tail of the specific heat. Using the method of Daniels[65] we can evaluate the required lattice sum by computer, evaluating the dipole contribution for all ions and putting in the exchange parameters J_1 and J_2 between nearest neighbours. This gives an equation roughly quadratic in the exchange parameters and it is easiest to solve this graphically with the two linear equations obtained previously.

This is carried out in Fig.6-6 where we see that if we treat the two linear equations as representing error limits we do not obtain a unique solution but a band of solutions.

It is interesting to note that for solutions with small $|J|$ we obtain a ferromagnetic J_1 and an antiferromagnetic J_2. The reason for this can be seen when we remember that the contribution to the $1/T^2$ term from each of the nearest neighbours is of the form:

$$(\text{dipole term} + \text{exchange term})^2$$

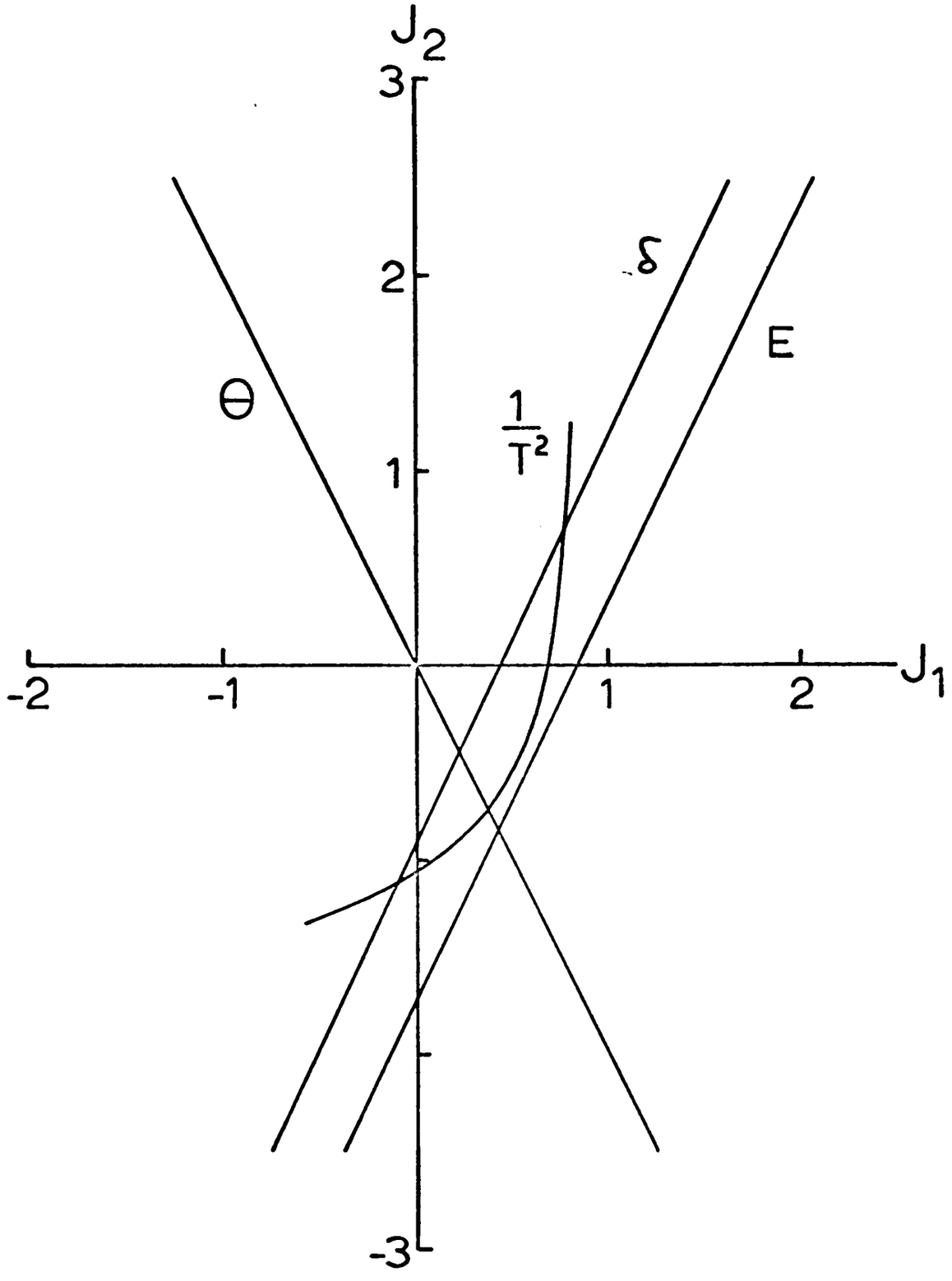


Fig. 6-6

Now the dipole term due to sublattice 2 is negative and that due to sublattice 4 is positive so that to increase the size of each term we need contributions of the same sign (with the restriction that the exchange term must be smaller than the dipole term). This gives the result $J_1 < 0$ and $J_2 > 0$.

To try and obtain a unique solution we can turn to the Weiss θ values which can often be used to estimate the strength of interactions. However in this case our failure to determine the temperature independent term in the susceptibility means that the observed values for the Weiss θ will be too large.

However we can obtain some estimate for the exchange if we first subtract the dipole contribution. Here we obtain a very surprising result - that the dipole contribution to the Weiss θ is less than $0.1^{\circ}K$. This is because the dipole contribution depends on the size of the F mode in the dipole sums and this is very small since the structure is close to cubic.

Thus although the ordering is mainly due to dipole interactions, these do not give a Weiss θ of the expected size showing how the simple theory result of $\theta/T_N \gtrsim 1$ can sometimes give very erroneous results in

estimating an ordering transition from high temperature susceptibility results.

However the fact that the Weiss θ is negative does tell us that the total exchange contribution must be antiferromagnetic. This gives as the extra equation:

$$2J_1 + J_2 < 0$$

and the solution must lie to the left of the line marked "θ" in Fig.6-6. This considerably reduces the allowed range of values and shows that J_2 is much stronger than J_1.

Thus we arrive at the estimates:

$$-0.10^{\circ}K < \frac{J_1}{k} < 0.35^{\circ}K$$

$$-1.15^{\circ}K < \frac{J_2}{k} < -0.75^{\circ}K$$

These results are consistent with the values of Hufner[54]:

$$J_1/k = 0 \pm 0.5^{\circ}K$$

$$J_2/k = -1.2 \pm 0.5^{\circ}K$$

An interaction $J_2/k = -1^{\circ}K$ corresponds to an extra effective field of 0.6kOe and if we include this in the calculation of the fields required to obtain the first and second flips we obtain the dotted curves in Figs.6-3 and 6-5 and it can be seen that agreement with experiment is now very good with the single exception of the first

flip along the b-axis.

6-5. Summary.

After evaluating the dipole contribution for the various kinds of flips we showed that the main features of the moment curves could be explained reasonably quantitatively using dipole interactions alone.

It was shown that in general the flips correspond well to simple reversal of the direction of magnetization and good agreement was obtained for the variation of critical field with angle in the a-b plane. The different slopes of the moment curve for the first and second flip were explained by consideration of the different internal fields on the sublattices.

The nearest neighbour exchange constants were estimated as:

$$-0.10^{\circ}K < \frac{J_1}{k} < 0.35^{\circ}K$$

between the four neighbours in the a-b plane, and

$$-1.15^{\circ}K < \frac{J_2}{k} < -0.75^{\circ}K$$

for the two neighbours along the c-axis.

CHAPTER SEVEN

OTHER MAGNETIC MEASUREMENTS.

7-1. Introduction.

In addition to the detailed study on $GdAlO_3$ and $DyAlO_3$ described in the preceding chapters, susceptibility measurements were carried out on members of four other families of rare earth compounds. These had the general formulae $RNbO_4$, R_3NbO_7, R_2TiO_5 and $R_2Ti_2O_7$ while the remaining members of the $RAlO_3$ family studied included two with the rhombohedral distortion of the perovskite structure as well as several others with the orthorhombic structure.

The susceptibility measurements were carried out on polycrystalline or powder specimens using the a.c. mutual inductance technique. All the compounds were measured in the liquid He^4 range (4.2° - $1.0^\circ K$) and in two cases down to $0.4^\circ K$ in the d.c. He^3 cryostat to try and find a suspected transition. In addition, a measurement at the melting point of liquid hydrogen, $20.4^\circ K$, was always taken, coupled with a complete run from 20.4° - $14^\circ K$ if the $20^\circ K$ point did not tie up with the extrapolation of the helium range due to the nearness

of a transition.

7-2. Interpretation of Susceptibility Measurements.

Measurement of the magnetic susceptibility, χ, is probably the easiest and fastest method of obtaining data about a magnetically interesting compound. First, any transition shows up immediately as a break in the curve - either to a decrease in the value of χ with decreasing temperature in the case of an antiferromagnet or as a complex and very rapid increase in χ during a transition to ferromagnetism.

If no magnetic transition is observed an estimate of the strength of the magnetic interaction can be obtained by trying to fit the data to the general Van Vleck expression for the magnetic susceptibility:

$$\chi = \frac{C}{T - \theta} + \alpha \qquad \ldots (7\text{-}1)$$

Here C is the molar Curie constant and equals $Ng^2\beta^2S(S+1)/3k$

θ is the Weiss constant and equal to γC,

and α is the Van Vleck temperature independent susceptibility.

In molecular field theory the constant γ is called the interaction parameter and expresses the relation between the effective internal field ... $H_E = \gamma \mathcal{M}$

where $\mathcal{M}$ is the magnetization. Thus the Weiss constant gives us a direct measure of the size and sign (+ for ferromagnetic, - for antiferromagnetic) of the magnetic interaction. It is usually $\geq T_c$, the magnetic ordering temperature and the ratio θ/T_c can be used to help determine the ordered arrangement of moments below T_c.

The separation of the low-lying energy levels varies widely in the rare earths. For many, the crystal field splitting of the L,S,J ground state is so large that only the lowest lying level (a doublet in the case of the odd-electron Kramers' ion) is appreciably populated at the temperature we are considering. In this case susceptibility measurements as a function of temperature give considerable information as to which of the original J multiplet levels lies lowest and how far away the next levels are. The g-tensor in this case is often very anisotropic and this is apparent even though our measurements on powder specimens only gives a root-mean-square value.

The temperature independent term, α, depends on the energy difference between the ground and excited energy levels through the matrix elements of the magnetic field operator $\beta \underline{H}.(\underline{L} + 2\underline{S})$.

$$\alpha = 2N \sum_j \frac{\left|\langle i|\underline{L}+2\underline{S}|j\rangle\right|^2}{E_j - E_i}$$

where i and j are the ground and excited states respectively.

In the case of the Gd^{3+} ion, which has an $^8S_{7/2}$ ground state, the splittings of the J multiplet will be small as already described in the case of $GdAlO_3$, so that at the temperature of these experiments we can expect the magnetic properties of the ion to be those of an 8-fold degenerate state. For such an S-state ion, the g-value must equal 2 thus giving a theoretical Curie constant of 7.875. Departure from this value is an indication of the non-stoichiometry of the compound and is a useful complement to chemical analysis.

There may be departures from the formula (7-1) for a number of reasons. As the temperature increases, low-lying energy levels may become appreciably populated, while at low temperatures when T is of the order of θ, there may be departures from the behaviour predicted by the simple molecular field theory of the interactions. For the non-Kramers' ions (Pr^{3+}, Eu^{3+}, Tb^{3+}, Ho^{3+}) where the lowest state is a singlet, all other states may become depopulated before any co-operative interaction can take

place and the susceptibility then tends to a temperature independent value.

In spite of these limitations, Eq.7-1 provides a useful basis for interpreting magnetic susceptibility measurements and consequently all the compounds have been so fitted, although it will be pointed out that some are merely empirical fits to the data.

All the measurements have been corrected for the demagnetizing effect of the shape of the specimen and the results given are referred to a spherical sample. In the case of compounds which have undergone an antiferromagnetic transition, the quoted Néel temperature is the point of maximum positive slope on the χ - T curve since most theories of magnetic ordering prefer this definition to the alternative of the peak value of susceptibility.

A tabulation of the results obtained on this basis is given in Table 7-I.

7-3. Rare Earth Orthoaluminates $RAlO_3$.

Of the seven members of this family measured, five have the Pbnm structure already described for $GdAlO_3$ and $DyAlO_3$, while the remaining two, $PrAlO_3$ and $NdAlO_3$,

TABLE 7-I

Susceptibility Data.

R	T_N	Curie-Weiss Law	Remarks
$RAlO_3$			Stoichiometric
Pr	-	temp. independent	Large Crystals
Nd	-	0.65/(T+3.2)+0.015	Small crystals
Gd	3.9°	7.9 /(T+4.8)	"
Tb	4.0°	10.7/(T+6.5)	"
Dy	3.5°	10.3/(T+4.7)+0.08	"
Ho	-	11.1/(T+5.3)	"
Er	0.5°	6.8 /(T+3.4)	Powder
R_2TiO_5			Non-stoichiometric
Gd	-	8.8 /(T+10)	Fine needles
Dy	1.55°	-	Platelets
$R_2Ti_2O_7$			Non-stoichiometric
Gd	-	7.7 /(T+11.7)	Small crystals
Tb	-	4.5 /(T+1.2)+0.14	"
Dy	1.3°	12.4/(T+0.65)	"
Ho	1.3°	12.6/T	Over 9° - 20.4°K

TABLE 7-I (cont.)

R	T_N	Curie-Weiss Law	Remarks
$RNbO_4$			Stoichiometric
Nd	-	0.52/(T+1.2)+0.006	Small crystals
Gd	1.67°	8.0 /(T+2.5)	"
Tb	1.82°	11.0/(T+8.3)	Flaky crystals
Dy (a)	1.52°	11.9/(T+4.1)	Large crystals
(b)	1.60°	7.4 /(T+2.7)	"
Ho	-	5.9 /(T+1.7)+0.23	Flaky crystals
Er	-	5.4 /(T+1.4)+0.15	Small crystals
Yb	-	1.1 /(T+0.07)+0.028	"
R_3NbO_7			Non-stoichiometric
Gd (a)	1°	6.1 /(T+5.9)	Small crystals
(b)	1°	7.2 /(T+7.5)	"
Dy	1°	10.9/(T+3.7)	Small crystals
Ho	1°	10.3/(T+2.2)	"

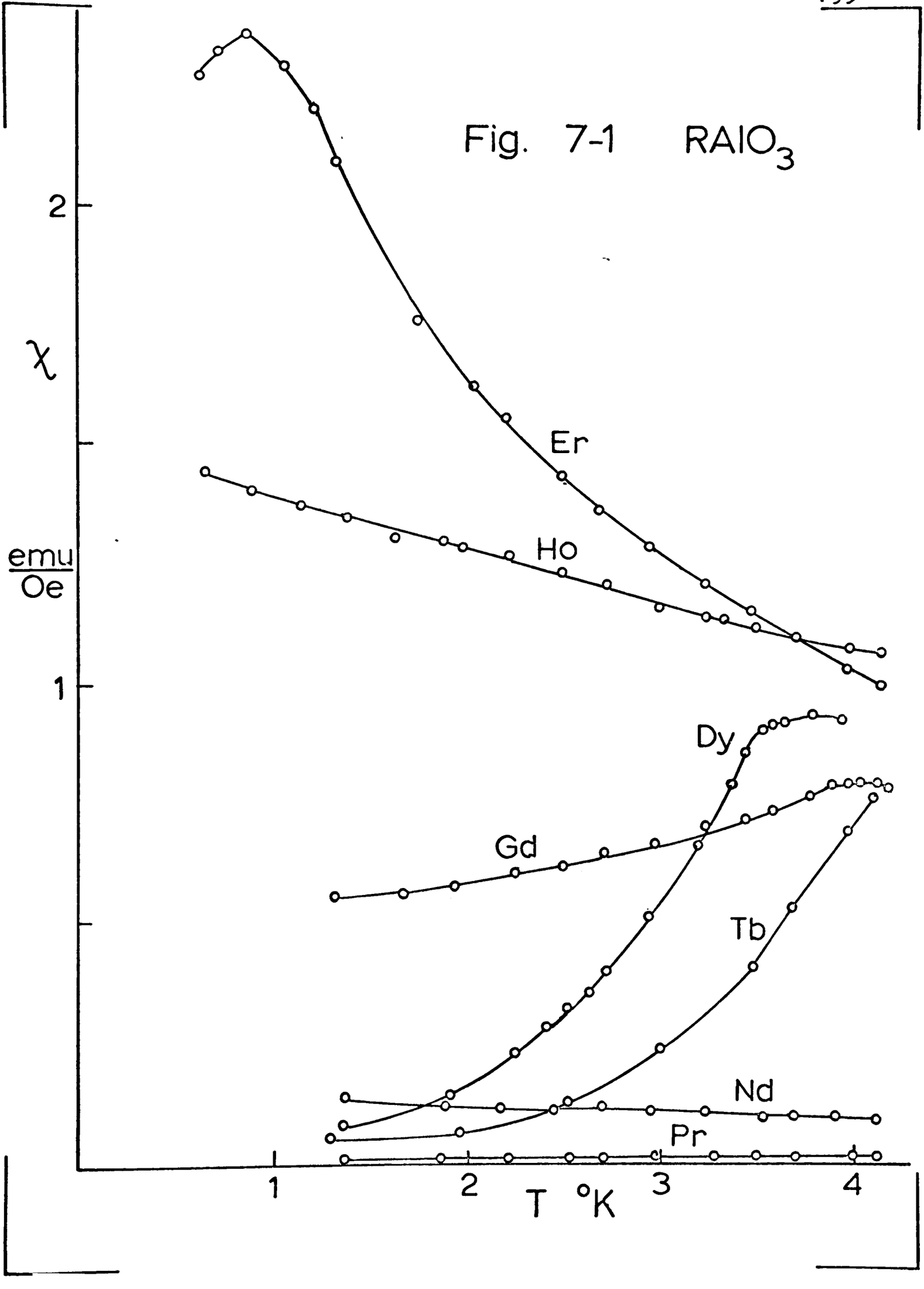
have the rhombohedral structure D_{3d}^5 - $R\bar{3}m$ also described in Section 1-3.

The rare earth sub-lattice in $R\bar{3}m$ is slightly distorted from simple cubic as in Pbnm, but with smaller distortions because $R\bar{3}m$ is nearer crystallographically to the true cubic perovskite structure.

The small crystals used were all grown from a PbO or PbO/PbF_2 flux as described in Ref.12 and were usually very twinned. The only exception was $ErAlO_3$ which was a very fine pink powder.

The susceptibility of the gadolinium and dysprosium compounds as shown in Fig.7-1 agreed well with the average of the single crystal results described earlier and the terbium compound with that described in Ref.59. The Néel temperatures also agreed well with the more accurate results from specific heat measurements(60. The ground state of Tb^{3+} has been determined from optical measurements(61 to be the doublet $J_z = \pm 6$ and this gives a Curie constant within 5% of our value of 10.7.

$ErAlO_3$ has a transition temperature much lower than would be expected from its value of the Weiss θ and nothing is known of its ordering arrangement. The extremely low value of χ for $PrAlO_3$ indicates that its


Fig. 7-1 $RAlO_3$
χ
emu/Oe
2
1
Er
Ho
Dy
Gd
Tb
Nd
Pr
1
2
3
4
T °K

lowest excited state must be at least 100 cm^{-1} above the ground state.

7-4. Rare Earth Orthoniobates $RNbO_4$.

The system R_2O_3/Nb_2O_5 contains three series of compounds $RNbO_4$, R_3NbO_7 and RNb_3O_9. The first of these crystallizes into a monoclinic distortion of the tetragonal scheelite structure with the space group C2 - C_2^3. The rare earth sublattice is body-centred with four extra ions on opposing faces in the positions $(0,\frac{1}{2},1/4)$ and $(\frac{1}{2},0,3/4)$.

The specimens were grown[58] either by cooling from 1340° to 900°C at 3°C/hr in the presence of Bi_2O_3/B_2O_3 flux or by evaporation at 1230°C from PbF_2 flux. Small crystals were generally formed except for the terbium and holmium compounds which were very flaky.

Unfortunately all the compounds undergo a crystallographic distortion at about 800°C so that no single crystals were obtained at room temperature. An attempt was made with the well-formed bipyramidal $GdNbO_4$ to heat it above the transition and allow to cool under uniaxial pressure but this was not successful in removing all the twinning.

As can be seen from the results in Fig.7-2 the Gd, Tb and Dy compounds all underwent transitions to an antiferromagnetic state in the measured region. The susceptibility of the holmium compound has also started to turn over but it was not possible to tell whether it too was about to go antiferromagnetic or whether it was becoming temperature independent.

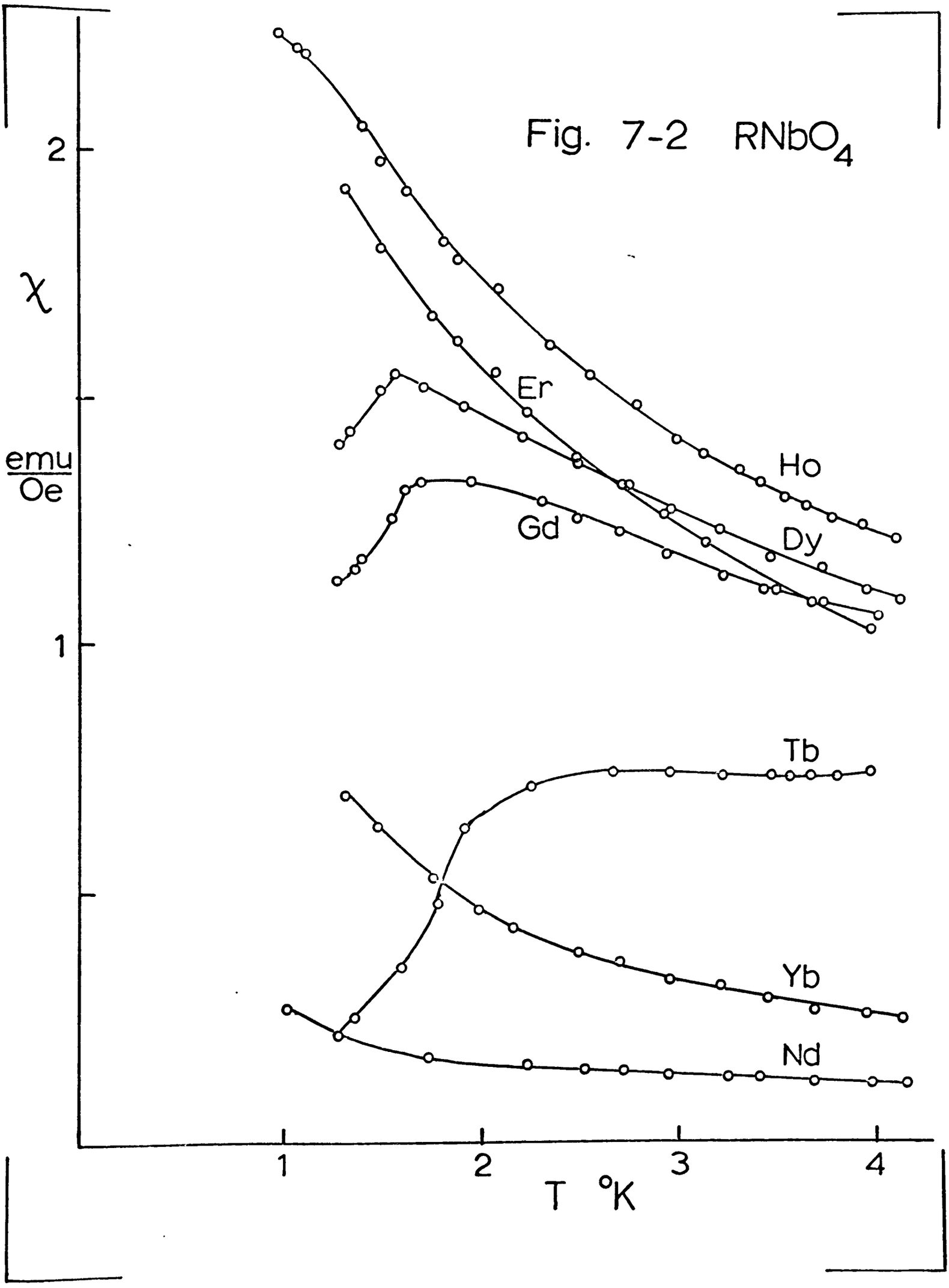
The value of the Curie constant in $GdNbO_4$ helps confirm the belief that the $RNbO_4$ are a stoichiometric series. Wang and Gravel[62] have measured the powder susceptibility of $GdNbO_4$ and $NdNbO_4$ at temperatures above 20.4°K. Our results are essentially in agreement for $GdNbO_4$ for which they obtain

$$\chi = 8.0/T$$

but differ markedly in the case of neodymium for which they observed an antiferromagnetic transition at 25°K and a Curie-Weiss law above that temperature of:

$$\chi = \frac{1.94}{T + 30}$$

This seems very unlikely for neodymium, which may have a large magnetic interaction in intermetallic compounds, e.g. $NdAl_2$(T_N = 65°K), NdAl(25°K), NdBi(24°K), $Nd_{0.7}Y_{0.3}$(34°K) and Nd(12°K), but is usually very weak in ionic compounds, e.g. $NdCl_3$(T_N = 0.47°K) and


Fig. 7-2 $RNbO_4$
χ
emu/Oe
2
1
Er
Ho
Gd
Dy
Tb
Yb
Nd
1
2
3
4
T °K

NdGaG (0.52°K).

The Curie-Weiss formulae for $TbNbO_4$ and $DyNbO_4$ cannot be taken too seriously since temperature independent terms would be expected from both, and the high value of θ for the terbium compound also makes results in the measured temperature range of doubtful validity.

7-5. Rare Earth Niobates R_3NbO_7.

This series of compounds exists in a range of stoichiometry from the nominal formula ratio of $75\%R_2O_3/25\%Nb_2O_5$ to $65\%R_2O_3/35\%Nb_2O_5$. The crystal structure is a distortion of the fluorite structure and is believed to be of the pyrochlore type. This means there will be two inequivalent rare earth sites, the formula being more understandably expressed as $R_2(R,Nb)O_7$. The rare earth sublattice is cubic with half the cells (grouped in adjacent pairs) being body-centred.

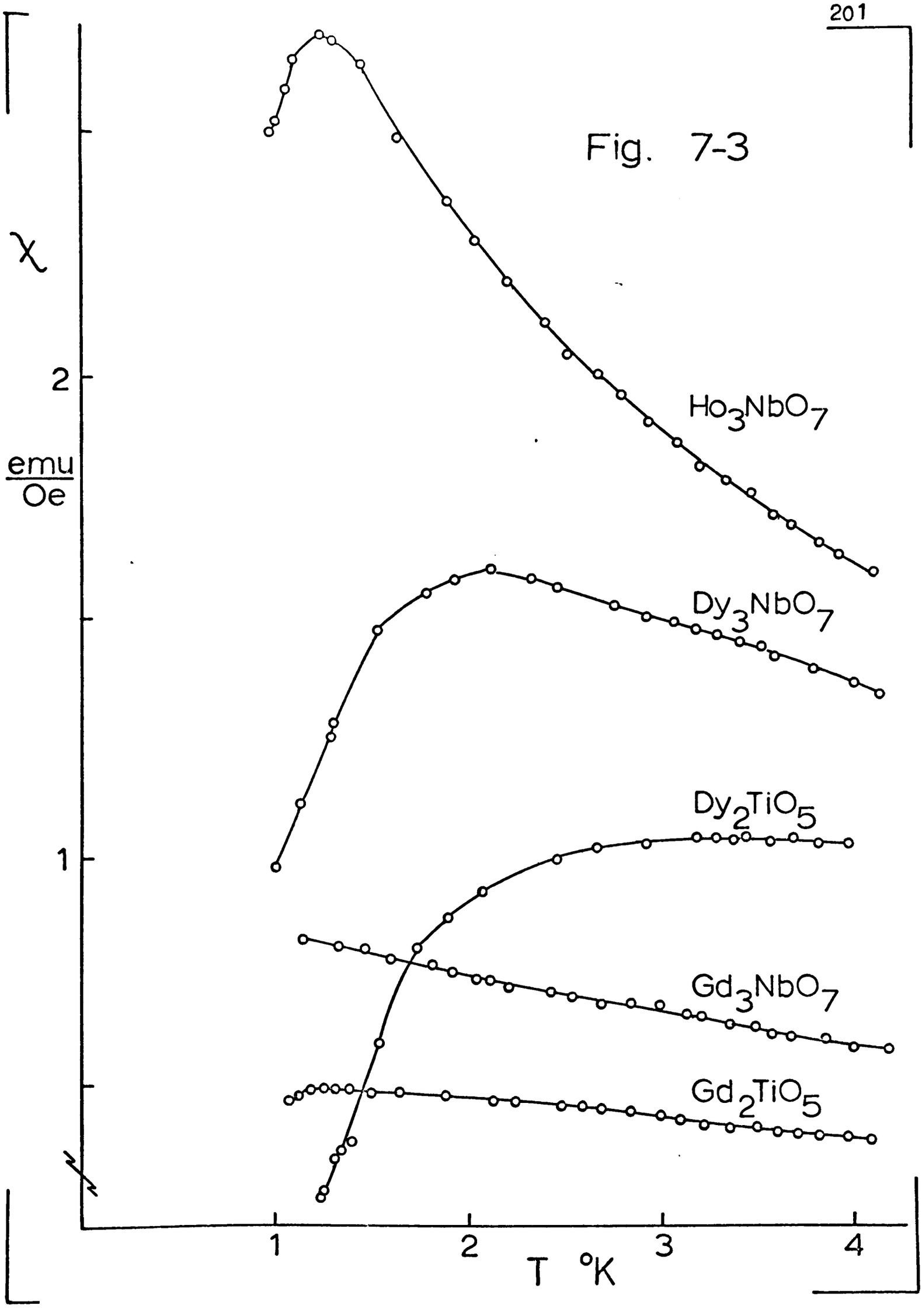
The crystals were grown[58] from a PbO/PbF_2 flux by cooling from 1285° to 950°C at 2°/hr and were all highly twinned. The formation of compounds with the flux necessitated non-stoichiometric melts and made it likely that the crystals are deficient in rare earth. It also appeared that the deviation from stoichiometry

tended to distort the structure from cubic by stretching along a body diagonal.

Both the holmium and dysprosium compounds underwent transitions to an antiferromagnetic state as can be seen from Fig.7-3. The susceptibility of the gadolinium compound has also flattened off at the limit of our measurement range and is about to become antiferromagnetic. An X-ray fluorescence analysis of the Gd_3NbO_7 showed that it contained a molar ratio of 67% Gd_2O_3/33% Nb_2O_5 and also 5wt% of Pb either substituted for gadolinium in the lattice or as occluded flux. This means a total deficiency of about 15% from the formula amount of gadolinium giving an expected Curie constant of 6.7 in agreement with the mean of our two results on different batches.

It is interesting that the large value of the Curie constant for the dysprosium and holmium compounds suggests that the ground doublet is characterized by very nearly the highest value of J_z which is available to each ion (J_z = 15/2 for Dy^{3+}, J_z = 8 for Ho^{3+}). The large value cannot be due to incorrect stoichiometry as the nominal amount of 75 mole % R_2O_3 is at the high end of the allowed range of stoichiometry.

Fig. 7-3



7-6. Rare Earth Titanates R_2TiO_5.

The system R_2O_3/TiO_2 contains two compounds, R_2TiO_5 and $R_2Ti_2O_7$, both of which have an allowed range of composition. The R_2TiO_5 series are an orthorhombic modification of the fluorite structure with the space group Pnam and have an allowed range of stoichiometry from 46 - 61% R_2O_3 (formula amount is 50%). The rare earth ions lie on the 4c sites and so form a distorted cubic sublattice the same as already described in the ortho-aluminates.

The crystals were grown[58] by slow cooling from a PbO flux and fine needles were obtained of the Gd_2TiO_5 and well formed platelets of the Dy_2TiO_5. The susceptibility measurements showed both crystals to have transitions to an antiferromagnetic state at 1.25 and 1.55°K respectively. An analysis of the gadolinium compound showed it to contain 55m% R_2O_3 giving an expected Curie constant of 8.7 in agreement with the average of our results. It is interesting that in the cases where measurements made on different batches of the same compound have given different Curie-Weiss laws as quoted, there has been very little change in the Néel temperature. This seems to indicate that flux impurities are usually occluded rather than distributed evenly in rare earth

sites through the lattice.

7-7. Rare Earth Titanates $R_2Ti_2O_7$.

The range of composition allowed for this set of compounds is 29 - 42 m% R_2O_3 bracketing the nominal figure of 33 m%. The crystal structure is the same as that of pyrochlore which is a rhombohedral distortion of the face-centred cubic structure Fd3m. The rare earths lie on a face-centred sublattice which is very nearly f.c.c. but the surrounding eight oxygens are such that two are considerably closer giving a roughly axially symmetric crystal field.

A PbF_2 flux was used[58] to prepare the samples and the solution evaporated to dryness at 1230°C. Small crystals were obtained in all cases except for one of the two $Gd_2Ti_2O_7$ batches which was powdery possibly due to inclusion of flux. No analysis of the gadolinium compound was available to compare with the measured Curie constants. However the susceptibility (Fig.7-4) was almost straight; and although giving an enormous Weiss θ (for a rare earth) of 11.7° it was the only gadolinium compound not to undergo a transition. Its behaviour is quite similar to that of potassium chloro-iridate[64] above its ordering temperature of 2.8°K.

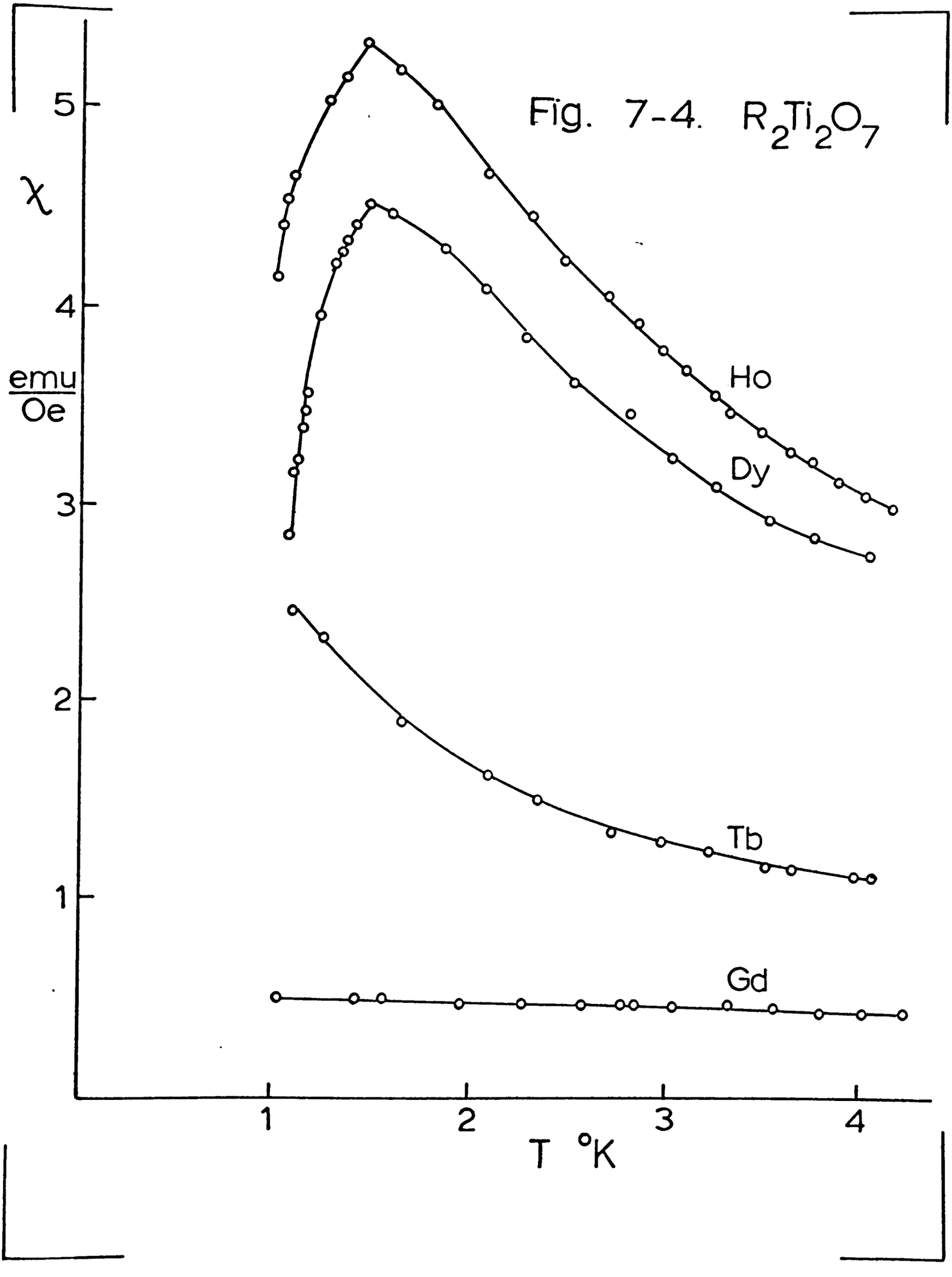


Fig. 7-4. $R_2Ti_2O_7$

The dysprosium and holmium compounds are unusual in the opposite way. Both undergo antiferromagnetic transitions and yet have very small Weiss θ's. Although this is not allowed on a simple molecular field picture it can happen in cases where we cannot simply divide the ions into two sublattices such that all ions on one sublattice have only nearest neighbours of the other sublattice. In a f.c.c. lattice the two sublattice model is certainly not possible. Second nearest neighbour interactions, dipole induced ordering and crystal field effects can also affect the θ/T_N ratio.

The large value of the Curie constant for both these compounds indicates that again there is a large crystal field splitting with the ground state being the doublet $J_z = \pm J$. Again however we must be warned by the absence of the expected temperature independent term and the lack of knowledge of the precise composition of the compounds measured.

7-8. Conclusions and Summary.

A surprising proportion of the compounds measured were found to be magnetically interesting, usually because of transitions to an antiferromagnetic state in the liquid helium range. Many seemed to be

extremely anisotropic, with the prospect of interesting crystal-field effects as well as the appreciable exchange or dipole-dipole interactions causing the ordering.

However more detailed work has only been carried out on three of the compounds - $GdAlO_3$ and $DyAlO_3$ as described in the preceding chapters, and $TbAlO_3$. This failure has been due in all cases to one cause - the difficulty of obtaining suitable single crystals.

In the case of $ErAlO_3$ various methods failed to give crystals of any appreciable size. The $RNbO_4$ series all undergo a crystallographic distortion between the flux-growing temperature and room temperature so that all the specimens were highly twinned. The other three series R_3NbO_7, R_2TiO_5 and $R_2Ti_2O_7$ are all non-stoichiometric making it very hard to obtain sensible answers when the composition may not only change within one batch but even along the length of one crystal.

However, much information about the series was obtained from the simple measurements performed and although in some cases it could be seen that not all the effects known to exist could be quantitatively included, considerable knowledge on the size and anisotropy of interactions, the nature of the ground state and the splitting to the next excited state could be deduced.

APPENDIX 1

Ordering Modes in the Pbnm Structure.

It has been pointed out by Bidaux and Meriel[43] that there are two different kinds of G_xA_y magnetic ordering modes when one considers the distortions of the dysprosium atom from being on a (0,0,1/4) site. In this Appendix we shall explain the difference between the two modes and explain why the situation does not arise for the A_xG_y ordering mode of $GdAlO_3$.

In Fig.A-1 we depict the projections on the a-c and b-c planes of the dysprosium atoms where the first line represents atoms of types 1 and 2 in a line up the c-axis and the second line the atoms of types 3 and 4. It can be seen that the projection onto the a-c plane is different from that on the b-c plane.

If we now put a magnetic moment on each of the atoms we find that there are two possible configurations for each of the G_x and A_y modes as shown in the lower part of Fig.A-1. The four possible ways of combining these modes are shown in Fig.A-2 where we have now depicted the projection on the a-b plane to show more clearly the relation between the directions of the moment

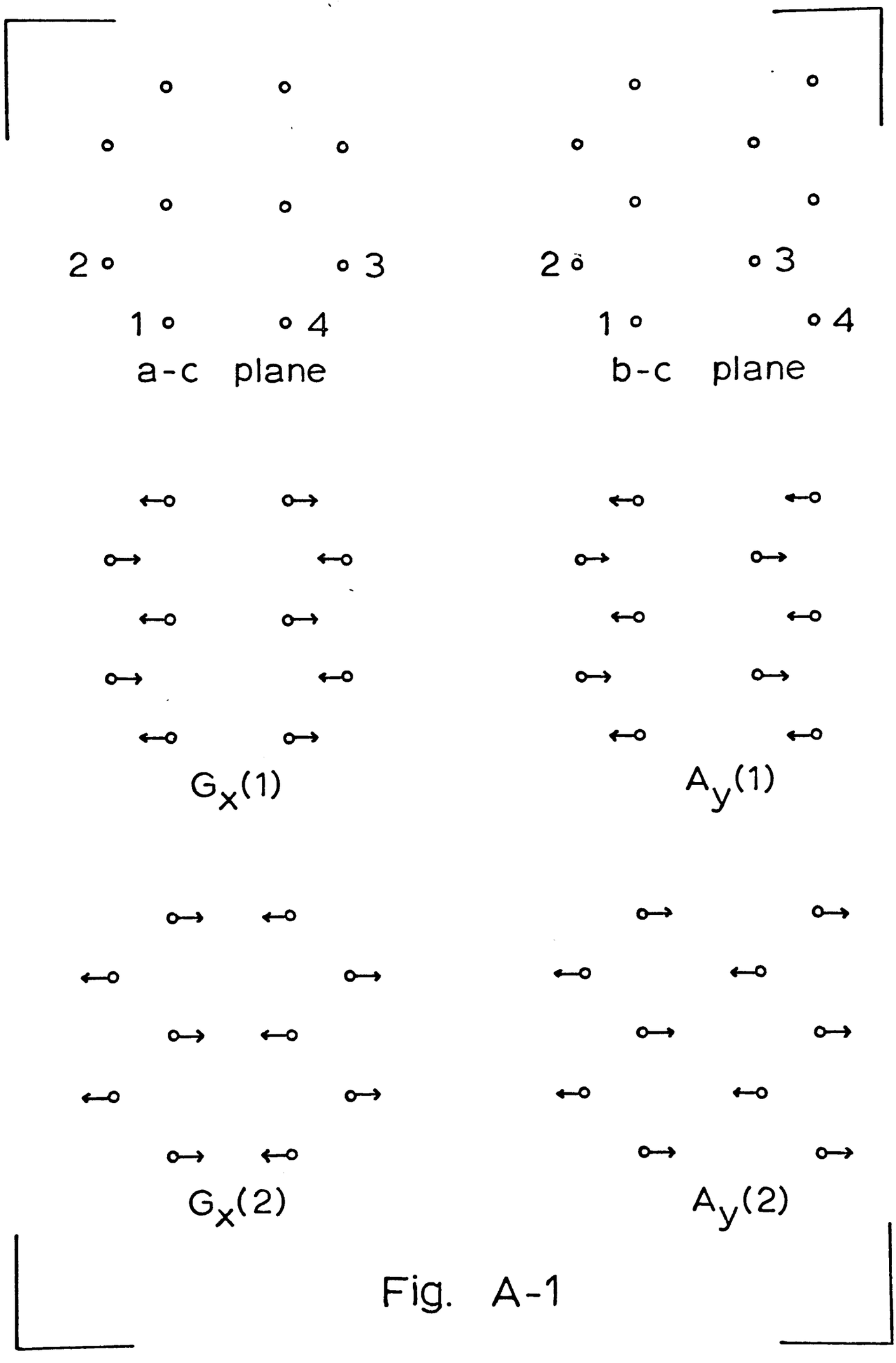


Fig. A-1

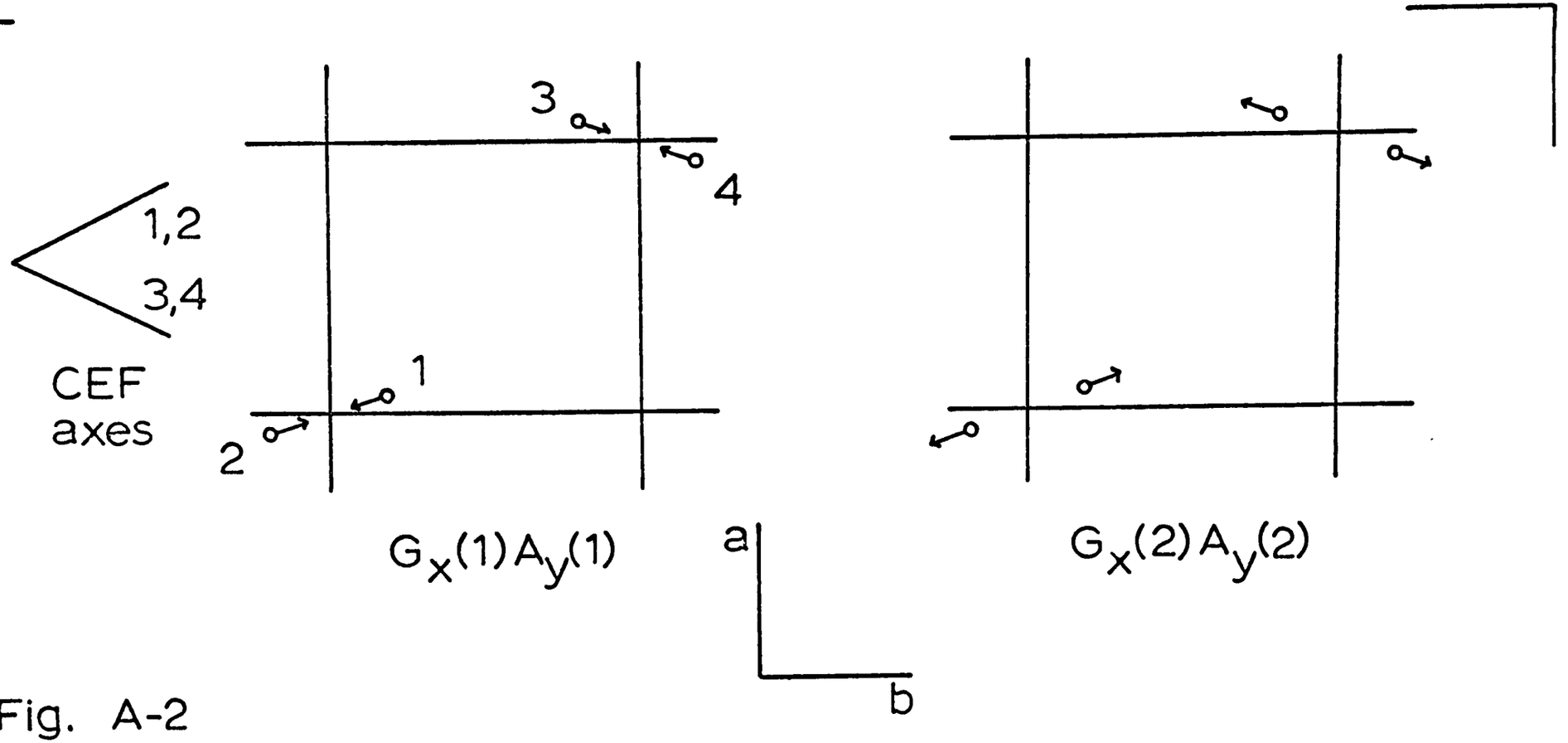


Fig. A-2

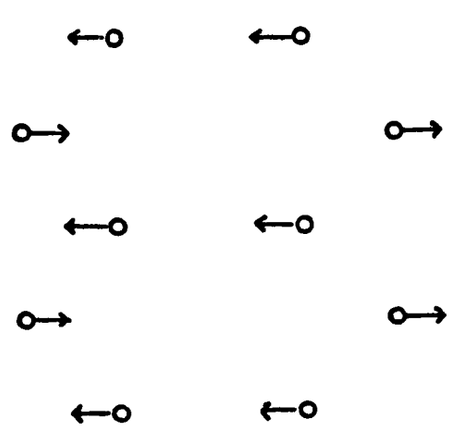
on each atom.

However we have not considered the effect of the direction of the major g-value which is determined by the crystal field. The direction of this axis for the two different magnetic sites is also shown in Fig.A-2 and we see that it is inconsistent with the lower two diagrams leaving only the possibilities $G_x(1)A_y(1)$ and $G_x(2)A_y(2)$.

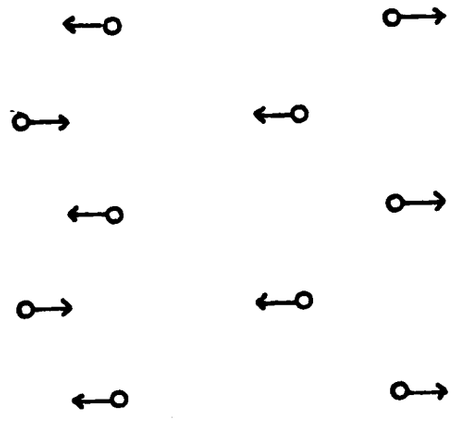
It is the former of these possibilities which Bidaux and Meriel prefer from both analysis of their neutron diffraction results and consideration of the mode most favoured by the dominant dipole-dipole interactions.

In considering the case of $GdAlO_3$ we depict in Fig.A-3 the analogous diagrams to those in Fig.A-1 for the case of A_xG_y. However here it is not so obvious that we have obtained different results because we can obtain $G_y(2)$ from $G_y(1)$ by simply swopping the lines of atoms $(1,2) \leftrightarrow (4,3)$ and similarly for the A mode although here we must also rotate the crystal by 180^o.

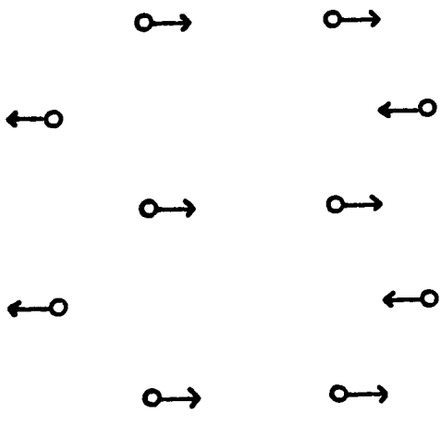
Again the cross product modes $A_x(1)G_y(2)$ and $A_x(2)G_y(1)$ are forbidden by the principal axis of the crystal field. However the projection on the a-c plane of the other two modes which is depicted in Fig.A-4



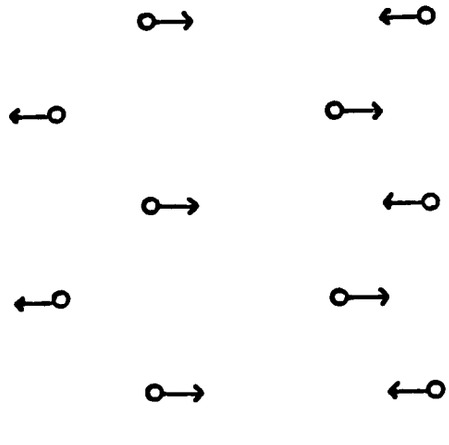
$A_x(1)$



$G_y(1)$

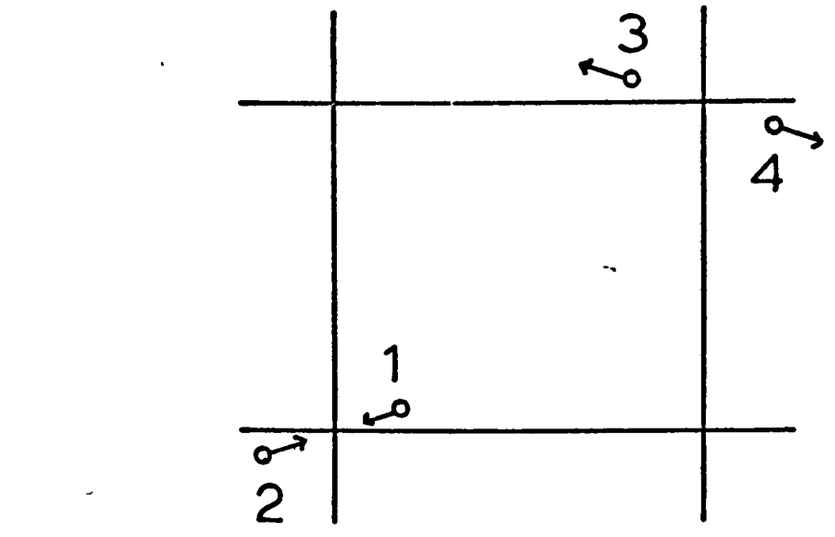


$A_x(2)$



$G_y(2)$

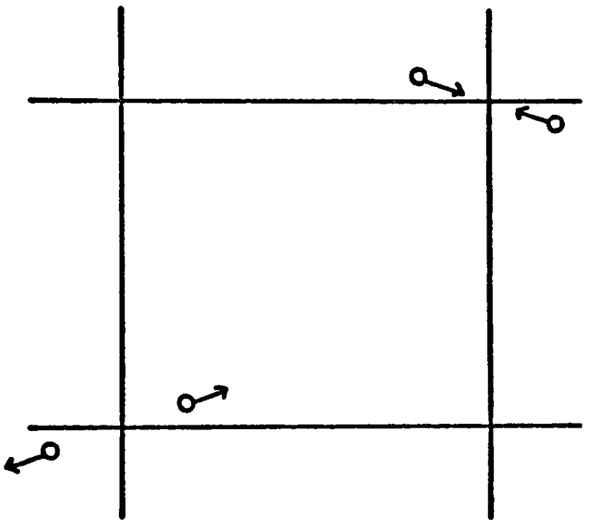
Fig. A-3



$A_x(1)\,G_y(1)$

a

b



$A_x(2)\,G_y(2)$

Fig. A-4

clearly shows that the other two modes are identical provided we interchange the atoms (1,2) $\leftrightarrow$ (4,3). In a real crystal of course we have no way of choosing between the pairs (1,2) and (4,3).

Fig.A-4 does bring out a very interesting point - that the relation between the moments on atoms 1 and 2 is different from that between atoms 3 and 4 although because of the isotropic nature of the interactions of the gadolinium ion this would be very hard to detect in any physical experiment.

GLOSSARY OF SYMBOLS.

The following symbols occur frequently throughout the thesis without accompanying explanation.

A_i	Type of ordering (Bertaut notation).
B	Brillouin function.
C	Molar Curie constant.
"	Specific heat.
C_i	Type of ordering (Bertaut notation).
D	Crystal field parameter $D\left[S_z^2 - 1/3\ S(S+1)\right]$
E	Crystal field parameter $E(S_x^2 - S_y^2)$
"	Energy.
F_i	Type of ordering (Bertaut notation).
G_i	Type of ordering (Bertaut notation).
H	Applied magnetic field.
H_A	Anisotropy field.
H_c	Spin flop field.
H_E	Exchange field.
K	Hankel functions.
M	Magnetic moment.
N	Avogadro's number.
R	Universal gas constant.
S	Total effective spin.
"	Entropy.

T	Temperature.
T_{AE}	Low temperature spin wave gap.
T_N	Neel temperature.
V	Anisotropy energy.
Z	Partition function.
a	Crystallographic axis.
b	Crystallographic axis.
c	Crystallographic axis.
g	Spectroscopic splitting factor.
k	Boltzmann factor.
m	Reduced sublattice magnetization.
t	Time.
x	Crystallographic distortion.
y	Crystallographic distortion.
z	Crystallographic distortion.
n	Number of nearest neighbours.
$\mathcal{H}$	Hamiltonian.
$\mathcal{m}$	Sublattice magnetization.
Σ	Summation.
α	Van Vleck temperature independent susceptibility.
n	Principal axis of the crystal field.
β	Bohr magneton.
n	Principal axis of the crystal field.
γ	Molecular field constant, $2zJ/Ng^2\beta^2$.

δ Small change.

η Canting angle of sublattice magnetizations.

θ Weiss term in susceptibility.

ϑ Spherical polar angle.

λ Angle of crystal field α-axis to b-axis.

π 3.14159....

τ Reduced temperature T/T_N.

ϕ Spherical polar angle.

χ Susceptibility.

REFERENCES.

1. C.Domb & A.R.Miedema, Progress in Low Temperature Physics Vol IV, ed. Gorter (North Holland, 1967) p296.

2. P.Weiss, J.de Phys., 6, 667 (1907).

3. W.Heisenberg, Z.Physik, 38, 411 (1926).

4. P.A.M.Dirac, Proc.Roy.Soc., A112, 661 (1926).

5. W.Heisenberg, Z.Physik, 49, 619 (1928).

6. J.Frenkel, Z.Physik, 49, 31 (1928).

7. E.Ising, Z.Physik, 31, 253 (1925).

8. L.Onsager, Phys.Rev., 65, 117 (1944).

9. T.L.Thorp, Thesis, Clarendon Laboratory, Oxford (1966).

10. F.R.McKim & W.P.Wolf, J.Sci.Instr., 34, 64, (1957).

11. S.Geller & B.V.Bala, Acta Cryst., 9, 1019 (1956).

12. G.Garton & B.M.Wanklyn, J.Cryst.Growth, 1, 164 (1967).

13. E.F.Bertaut, Magnetism Vol III, ed. Rado & Suhl, (Academic Press, 1963) p150.

14. J.F.B.Hawkes, Thesis, Clarendon Laboratory, Oxford (1968).

15. R.Bidaux & P.Meriel, J.Phys.(Fr.), 29, 220 (1968).

16. K.W.Blazey & H.Rohrer, Helv.Phys.Acta, 40, 370 (1967). Phys.Rev., 173, 574 (1968).

17. R.L.White, G.F.Herrmann, J.W.Carson & M.Mandel, Phys.Rev., 136A, 231 (1964).

18. H.R.Boesch, E.Brun & B.Dherighetti, Helv.Phys.Acta, 41, 417 (1968).

19. B.J.C.van der Hoeven Jr., Dale T.Teaney & V.L.Moruzzi, Phys.Rev.Lett., 20, 719 (1968).

D.T.Teaney, V.L.Moruzzi & B.L.Argyle, J.Appl.Phys., 37, 1122 (1966).

P.Handler, D.E.Mapother & M.Rayl, Phys.Rev.Lett., 19, 356 (1967).

M.Rayl, O.E.Vilches & J.C.Wheatley, Phys.Rev., 165, 692 (1968).

20. C.Domb, Proc.Phys.Soc., 86, 933 (1965).

M.E.Fisher & A.E.Ferdinand, Phys.Rev.Lett., 19, 169 (1967).

B.M.McCoy & T.T.Wu, Phys.Rev.Lett., 21, 549 (1968). Phys.Rev.,176, 631 (1968).

21. J.Skalyo Jr., A.F.Cohen, S.A.Friedberg & R.B.Griffiths, Phys.Rev., 164, 705 (1967).

22. B.E.Keen, D.P.Landau & W.P.Wolf, J.Appl.Phys., 38, 967 (1967).

23. P.C.Mangelsdorf, J.Appl.Phys., 30, 442 (1959).

24. L.P.Kadanoff, W.Gotze, D.Hamblen, R.Hecht, E.A.S.Lewis, V.V.Palciauskas, M.Rayl, J.Swift, D.Aspnes & J.Kane, Rev.Mod.Phys., 39, 395 (1967).

25. D.S.Gaunt, Proc.Phys.Soc., 92, 150 (1967).

26. M.E.Fisher, Proceedings of the Conference on Critical Phenomena, Washington 1965, National Bureau of Standards, (1966).

27. J.A.Eisele & F.Keffer, Phys.Rev., 96, 929 (1954).

28. J.H.Van Vleck, J.Chem.Phys., 9, 85 (1941).

29. R.J.Joenk, Phys.Rev., 128. 1634 (1962).

30. H.B.Callen & S.Shtrikman, Sol.State Comm., 3, 5 (1965).

31. R.Hornreich & S.Shtrikman, Phys.Rev., 159, 408 (1967).

32. M.E.Fisher, Phil.Mag., 7, 173 (1963).

33. H.M.Gijsman, N.J.Poulis & J.van der Handel, Physica, 25, 954 (1959).

34. L.Néel, Ann.Phys., 5, 232 (1936).

35. W.van der Lugt & N.J.Poulis, Physica, 26, 917 (1960).

H.Forstat, J.N.McElearney & P.T.Bailey, Phys.Lett., 27A, 70 (1968).

See also Ref.33.

36. J.S.Smart, "Effective Field Theories of Magnetism", (W.B.Saunders Co., 1966).

37. C.Zener, Phys.Rev., 96, 1335 (1954).

38. P.Pincus, Phys.Rev., 113, 769 (1959).

39. F.Keffer, Handbuch der Physik, Vol XVIII/2 (Springer, 1966).

40. H.L.Davis, Phys.Rev., 120, 789 (1960).

41. E.D.Jones & K.B.Kefferts, Phys.Rev., 135A, 1277 (1964).

H.Montgomery, D.T.Teaney & W.M.Walsh Jr., Phys.Rev., 128, 80 (1962).

D.T.Edmonds & D.R.Taylor, Proc.Phys.Soc., 91, 356 (1967).

42. R.J.D.Gee, private communication.

43. R.Bidaux & P.Meriel, J.Phys.(Fr.), 29, 220 (1968).

44. L.D.Roberts, R.B.Murray & J.W.T.Dabbs, Phys.Rev., 100, 1100 (1955).

45. M.E.Lines, Phys.Rev., 156, 536 (1967).

46. J.S.Smart, Phys.Chem.Solids, 11, 97 (1959).

47. G.S.Rushbrooke & P.J.Wood, Mol.Phys., 6, 409 (1963).

48. K.H.Lee & S.H.Lui, Phys.Rev., 159, 390 (1963).

49. M.E.Lines, Phys.Rev., 135, A1336 (1964).

50. F.B.Anderson & H.B.Callen, Phys.Rev., 136, A1068 (1964).

51. J.H.Van Vleck, J.Chem.Phys., 5, 320 (1934).

52. I.S.Jacobs & S.D.Silverstein, P.R.Lett., 13, 272 (1964).

53. C.J.Ellis, private communication.

54. S.Hufner, H.Schuchert & N.Skribanowitz, Z.Naturf., 22A, 573 (1967).

H.Schuchert, S.Hufner & R.Faulhaber, J.Appl.Phys., 39, 1364 (1968).

H.Schuchert, S.Hufner & R.Faulhaber, Z.Physik, to be published.

55. I.Grambow, P.Kronauer, J.Schneider & H.Schuchert, Z.Naturf., 22A, 828 (1967).

56. G.N.Watson, "Theory of Bessel Functions", (Cambridge University Press, 1952).

57. E.Dempsey & G.C.Benson, Can.J.Phys., 38, 399 (1960).

58. G.Garton & B.M.Wanklyn, J.Mater.Sci., 3, 395 (1968).

59. A.H.Cooke et al., to be published.

60. J.D.Cashion, A.H.Cooke, T.L.Thorp & M.R.Wells, J.Phys.C, 1, 539 (1968).

61. L.Holmes, R.Sherwood & L.G.van Uitert, J.Appl.Phys., 39, 1373 (1968).

62. F.F.Wang & R.L.Gravel, Phys.Stat.Sol., 12, 609 (1965).

63. K.A.Gehring, Thesis, Clarendon Laboratory, Oxford (1966).

64. A.H.Cooke, R.Lazenby, F.R.McKim, J.Owen & W.P.Wolf, Proc.Roy.Soc., 250A, 97 (1959).

65. J.A.Daniels, Proc.Phys.Soc., 66A, 673 (1953).

66. W.P.Wolf, private communication.